
SEISMIC RISK ASSESSMENT FOR GEOHERMAL PROJECTS

WITH THE CREATION OF A PHYSICAL SCREENING MODEL

By

S. E. Nieuwstad

to obtain the degree of Master of Science

Master of Science
in Applied Earth Sciences
at the Delft University of Technology.

Student number: 4180208
Thesis committee: Dr. Ir. F.C. (Femke) Vossepoel, TU Delft, supervisor
Dr. P.J. (Phil) Vardon, TU Delft
Dr. D.V. (Denis) Voskov, TU Delft
Ir. B.E. (Barbara) Cox, Hydreco GeoMEC B.V.

NOMENCLATURE.....	5
ABSTRACT.....	8
1. INTRODUCTION.....	9
2. BACKGROUND AND LITERATURE.....	10
2.1 THE GEOTHERMAL SYSTEM	11
2.1.1 Geothermal plays	11
2.1.2 Hydrothermal vs Petrothermal	12
2.2 PHYSICAL BACKGROUND OF SEISMICITY	13
2.2.1 Induced seismicity.....	14
2.2.2 Induced seismicity causes.....	16
3. SUBJECT OF INVESTIGATION	19
4. SRA METHODOLOGIES	20
4.1 SODM METHODOLOGY.....	20
4.2 Q-CON/IF METHODOLOGY	23
4.3 TNO/GEOMECH MODEL	28
4.4 COMMON EVALUATION OF THE SRA METHODOLOGIES	30
5. NEW SEISMIC RISK ANALYSIS METHODOLOGY.....	31
5.1 SRA STEP 1	31
5.3 SRA STEP 2	36
5.4 SRA STEP 3.....	37
6. THEORY BEHIND PHYSICAL SCREENING MODEL	39
6.1 STRESS.....	39
6.2 MOHR CIRCLE.....	41
6.3 PORE PRESSURE.....	43
6.4 PORO-ELASTIC COUPLING	45
6.5 DIFFUSION OF PORE PRESSURE AND PORO-ELASTIC STRESS.....	48
6.6 THERMOELASTIC STRESSING.....	54
6.7 MOMENT	57
6.8 GROUND VIBRATIONS	59
7. PHYSICAL SCREENING MODEL.....	63
7.1 PSM STEP 1A: SPATIO-TEMPORAL EVOLUTION OF STRESS AND PRESSURE	64
7.1.1 Results	65
7.2 PSM STEP 1B: SPATIO-TEMPORAL EVOLUTION OF TEMPERATURE	69
7.2.1 Results	70
7.3 PSM STEP 2: STRESS STATE	73
7.3.1 Effective stress	73
7.3.2 Reservoir stress calculations	74
7.3.3 Results	75
7.4 PSM STEP 3: FROM STRESS TO SEISMIC MOMENT	79
7.4.1 Results	79
7.5 PSM STEP 4: GROUND MOTION PREDICTION	81
7.5.1 Results	82
8. PHYSICAL SCREENING MODEL RESULT ANALYSIS.....	84
8.1 SENSITIVITY ANALYSIS	84
8.1.1 Permeability.....	84
8.1.2 Injection rate.....	88
8.1.3 Injection temperature.....	91
8.1.4 Elastic moduli	93
8.2 SRA CASE STUDY: DAP PROJECT	97

8.3 SRA CASE STUDY: EXTREME CASE.....	99
9. DISCUSSION.....	102
10. CONCLUSION	104
APPENDIX	106
APPENDIX A: SRA STEP 2B.....	106
APPENDIX B: RUDNICKI EQUATIONS EXTENSION	108
APPENDIX C: THERMOELASTIC DIFFUSION EQUATIONS EXTENSION	109
APPENDIX D: DIFFUSION OF ΔP , $\Delta \Sigma_{\text{PORO}}$ (7.1.1)	110
APPENDIX E: MOHR CIRCLES FOR THRUST FAULTS AND STIKE SLIP REGIMES.....	111
APPENDIX F: SENSIBILITY ANALYSIS OF K (8.1.1)	114
APPENDIX G: SENSIBILITY ANALYSIS OF INJECTION RATE (8.1.2)	115
APPENDIX H: SENSIBILITY ANALYSIS OF ELASTIC MODULI (8.1.4)	116
APPENDIX I: DAPWELL PROJECT CASE STUDY (8.2).....	119
APPENDIX J: MODEL COMPARISON	122
1. TNO/GEOMECH model	122
2. DoubletCalc (TNO).....	124
12. REFERENCES	126

NOMENCLATURE

A = (total) area of the fault (over which the slip takes place) [m²]

B = Skempton's coefficient [-]

c = diffusivity [m/s]

C = cohesion of the rock or plane [Pa]

Δ CFF = faults friction coefficient [-]

C_r = heat capacity of rock [J/kg·°C]

C_w = heat capacity of water [J/kg·°C]

d = depth of hypocentre [m]

D = offset of the fault [m]

\bar{D} = total slip of the fault [m]

F = body force [kg·m/s²]

\vec{F}_n = force normal to the surface [kg·m/s²]

\vec{F}_0 = surface force [kg·m/s²]

\vec{F}_s = force parallel to the surface [kg·m/s²]

G = shear modulus [Pa]

h = head [m]

I = identity matrix as here considered to be a three directional situation [-]

K = bulk modulus [Pa]

k = permeability [m² or Darcy]

K_d = drained bulk modulus [Pa]

k_f = hydraulic conductivity [m/s]

K_g = bulk modulus of the grains [Pa]

L = length of the fault [m]

l = rupture length of the fault [m]

M = the magnitude of the seismic event [-]

M_L = local magnitude [-]

M₀ = seismic moment [Nm]

M_{0M} = seismic moment density [-]

$M_{0,T}(t)$ = maximal seismic moment [Nm]

M_w = moment magnitude of an seismic event [-]

OS = opslingerfactor [-]

P = fluid pressure [Pa]

PGV = peak ground velocity [cm/s]

$\vec{V}P$ = directional pressure difference [Pa]

q_z = fluid flow per unit area and time [m^2/s]

R_{epi} = distance to epicentre [m]

S = uniaxial specific storage [m^3]

t = (injection) time [s]

u_w = flow velocity of water [m/s]

u = average slip of the fault [m]

ν = Poisson's ratio [-]

V_h = peak ground velocity [cm/s]

w = height of the fault [m]

x = longitudinal direction [m]

z = elevation head [m]

α = Biot-Willis coefficient [-]

β = linear thermal expansion coefficient [-]

ε = total strain [-]

ζ = dimensionless variable that expresses the fluid volume transported out or into a storage [-]

η = viscosity [Pa·s]

θ = angle with the fault plane [-]

ϕ = angle of internal friction [-]

λ = (drained) lame parameters [Pa]

λ_u = undrained lame parameter [Pa]

λ_{eff} = effective thermal conductivity of the porous medium [W/m·°C]

λ_c = thermal conductivity of the aquifer [W/m·°C]

μ = (internal) friction coefficient [-]

μ_r = rigidity [-]

ρ_f = fluid density [kg/m³]

ρ_w = density of water [kg/m³]

ρ_r = density of rock [kg/m³]

σ = total stress [Pa]

σ_1 = largest principle stress [Pa]

σ_2 = medium principle stress [Pa]

σ_3 = smallest principle stress [Pa]

σ_n = normal stress [Pa]

σ_{neff} = effective normal stress [Pa]

σ_v = vertical stress [Pa]

$\sigma'_{v,eff}$ = poro-elastic effective vertical stress [Pa]

σ_H = maximum horizontal stress [Pa]

σ_h = minimum horizontal stress [Pa]

$\sigma'_{h,eff}$ = poro-elastic effective smallest horizontal stress [Pa]

τ = shear stress [Pa]

τ_p = critical shear stress [Pa]

φ = porosity [-]

Φ = fluid mass density [kg/m³]

ψ = poro-elastic stress coefficient [-]

ABSTRACT

Geothermal energy can be a great solution for the downscaling fossil fuel society, but it can potentially lead to seismic hazards. A doublet system, with a cold water injection well and a hot water production well, alters the stress situation in the subsurface, which can result in (micro)fracturing and fault reactivation. Even in water filled reservoirs, aquifers, with relatively good permeabilities, the acting in-situ stress on already existing fault can be changed such that there can be a seismic hazard. The three dominant phenomena that influence the fault reactivation and are triggered by geothermal water injection and production are the direct pore pressure change, poro-elastic stress change and thermo-elastic stress change.

To predict and subsequently diminish or limit the seismic hazards in geothermal operations, Seismic Risk Analysis (SRA) are to be completed before such operations can take place in an often seismic risky location, like densely populated areas. In the current (Dutch) geothermal environment mainly three SRA's are used; "Methodiek voor risicoanalyse omtrent geïnduceerde beving door gaswinning" by the Staatstoezicht op de Mijnen (StoM), "Defining the Framework for Seismic Hazard Assessment in Geothermal Projects V0.1" by Q-con/IF-technology [6] and an Excel-model created by TNO/Geomech. By investigating and reviewing these three SRA's in this thesis their shortcomings and limitations are exposed, for example their lack of physical foundation and explanatory results. From the foundation of the currently existing SRA's a new alternative SRA, which corresponds in some steps with the older SRA's, is created in this thesis. In order to successfully finish the new SRA one of the three steps should be completed, starting with SRA Step 1. In this first step of the new SRA a new Physical Screening Model (PSM) is created. When completing the SRA an indication of what type of seismic monitoring there should be done during production.

This PSM is a fairly quick and simple in its use but provides sufficient informative data to investigate the seismic hazard for most geothermal operations in the Netherlands. In four different steps in the PSM, the potential reactivation of faults over the whole reservoir during production will be evaluated. With the spatio-temporal evolution of ΔP , $\Delta\sigma_{poro}$, ΔT (PSM Step 1) this model can predict fault reactivation at any place and time inside the reservoir, while it can also look at which parameter dominated this reactivation. In this thesis the physical background and results of the PSM will be explained step by step. Eventually there are three final results from the PSM; a Mohr plot that predicts if certain faults (at certain locations) are stable or not and the maximum Moment magnitude (M_w) in combinations with the Peak Ground Velocity (PGV), which predict the severity of a possible event.

Sensitivity analyses and case studies done with the PSM in this thesis show the influence of dominating parameters, like permeability and injection rate, and what results can be expected when using this model.

1. INTRODUCTION

Geothermal energy is a renewable energy source that is generated and stored in the subsurface of the Earth. When operating into the (deep) subsurface, seismicity can potentially be a risk to deal with, especially when injecting fluids into and/or extracting fluids from a reservoir. As such is done in geothermal projects, it is important to know what the potential risks of seismicity are before geothermal operations are started; a so-called a priori risk assessment. Currently there are a couple approaches that provide a seismic risk analysis (SRA) that can be used as an indication for such risks. The three most widely used in the Netherlands are: “Methodiek voor risicoanalyse omtrent geïnduceerde beving door gaswinning” by the Staatstoezicht op de Mijnen (SodM) [59], “Defining the Framework for Seismic Hazard Assessment in Geothermal Projects V0.1” by Q-con/IF-technology [6] and an Excel-risk model created by TNO/Geomech [64]. In chapter 4 the existing SRA methodologies will be reviewed and subsequently a new SRA methodology will be proposed in chapter 5, which will give a more quantitative prediction of the seismic risk.

The creation of an alternative SRA will also include the development of a new quick-scan method. The SodM and Q-con/IF-technology SRA’s use their own Quick-Scan in similar ways. The new Quick-Scan provides a swift and practical seismic prediction of a certain geothermal field. This prediction is based on physical calculations. Chapters 6-8 will be fully dedicated to the explanation, creation and investigation of this new quick scan method: the Physical Screening Model (PSM).

The focus of this research will be on potential seismicity in hydrothermal systems, which contain a natural aquifer in a sedimentary reservoir, where no hydraulic treatment is needed. This is a so-called hot sedimentary aquifer (HSA). In chapter 2 a more complete story on the different geothermal systems and parameters are provided. In order to execute a good seismic risk analysis of such a hydrothermal system, it is necessary to find the (main) components and parameters that influence this induced seismicity. Usually these parameters are divided into reservoir parameters, like permeability, and operational parameters, like injection rate. The relation between these parameters and induced seismicity will be investigated in this thesis project. Subjects like; the reactivation faults and their shape and orientation; the importance of permeability; the injection rate; pore pressure; and more, will be addressed in this investigation.

2. BACKGROUND AND LITERATURE

Geothermal energy can play an important role in the search for more sustainable energy resources. Geothermal energy can (partly) replace fossil fuels for direct heat use or electricity generation. In the Netherlands geothermal energy is currently quickly developing. At the moment over 20 geothermal systems are operating; these are mainly developed for the horticulture industry (greenhouses)[47] [63]. So there is still a large opportunity for more geothermal projects, especially knowing that the total recoverable heat from sedimentary aquifers in the Netherlands is estimated to be 55 times larger than the Dutch annual heat consumption [21] [54].

According to the ‘Masterplan aardwarmte in Nederland’ (2018) [47] the geothermal industry is estimated to have an enormous growth potential in the coming years. This growth is primarily achieved by replacing the current fossil fuel generated heating systems in urban areas. The necessity of transitioning from gas to other more sustainable energies, like geothermal energy, comes from an environmental incentive; to reach the climate goals set in the ‘Paris Climate agreements’ in 2015 [45]. Another incentive for using sustainable energy is the decrease of gas produced from the Groningen gas field; here the production is lowered in order to reduce the earthquakes in the area induced by this large-scale gas production.

The goal of the Masterplan is to reduce CO2 emissions by 49% in 2030 and by 95% in 2050 relative to the year 1990 [47]. In order to accomplish this, it is necessary that 95% of all heat-produced energy will come from “clean energy” or “clean heat”. To achieve those numbers, several sustainable energy resources need to be implemented and replace fossil fuels; geothermal energy will play a big part in this replacement. Currently, the geothermal heat produces 0.5% of the total heat production in the Netherlands, the intentions are that this will grow to 5% in 2030 and 23% in 2050. Initially the greenhouse industry will be the main customer, but later on also urban areas and light industry will be a consumer of geothermal energy, see figure 2-1. Estimated is that geothermal heat can produce up to 40% of the total heat demand [47].

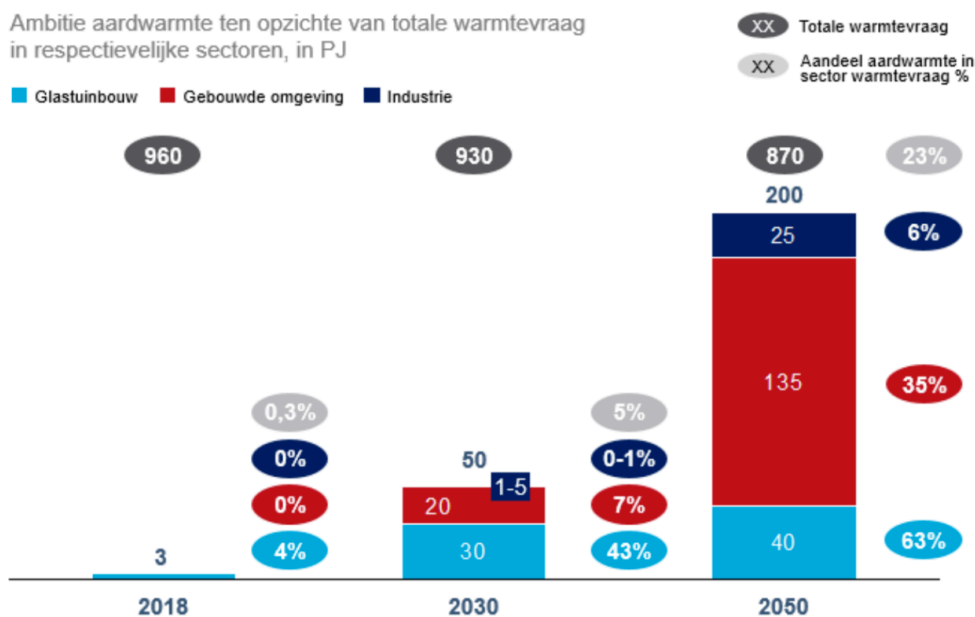


Figure 2-1. Ambition of the geothermal heat production relative to the total heat demand in their respective sectors, in PJ. The geothermal heat production can be 5% of the total heat demand in 2030 and 23% in 2050. Source: CE Delft, if technology, LTO glaskracht, McKinsey energy insights.

In order to meet the heat demand of the Masterplan in 2050 and to achieve the new energy and climate goals set by the European Council [26] and the Dutch government [48], many new geothermal systems will need to be built. As geothermal systems will be a heat source for residential buildings, the operating systems itself should be located close to (dense) urban areas, where millions of people live. This brings along a potential risk, as certain activities in the subsurface, which can change pressure, temperature, or the material balance, could potentially cause induced seismicity [47]. Therefore seismic risk and hazard assessments need to be made.

In order to evaluate and improve the existing SRA's for a priori risk assessment of induced seismicity in hot sedimentary aquifers, current literature and background information on both different geothermal systems and on the physics behind (induced) seismicity are presented in this chapter.

2.1 THE GEOTHERMAL SYSTEM

In this section the different geothermal plays and classifications will be described.

2.1.1 GEOTHERMAL PLAYS

A working geothermal play consists of geological settings and is essential when looking for a location in the subsurface to do (geothermal) operations in [44]. In contrast of the straightforward definitions hydrocarbon plays have, which are defined by 3 elements (source rock, reservoir and the trap), geothermal plays are not bounded by clear geological features. The geological settings for geothermal plays should at least include a heat source, heat migration pathway, (movable) heat storage capacity and the potential for economic recovery of that heat [44]. Its geological features like rock type and depth characterize a particular geothermal play.

CLASSIFICATION

The most common way to classify a geothermal resource is by looking at the enthalpy of the geothermal fluids [52]. The classification and boundaries between high and low enthalpy systems is not very distinctive [44].

Low enthalpy geothermal plays consist of low to moderate temperatures and are dominated by conduction, they occur in passive tectonics settings. The conduction in the rock is controlled by the temperature difference and thermal conductivity, while it relies on fluid flow [44]. Conductive plays are divided into hydrothermal, intra-cratonic basin types and orogenic belt types, and petro-thermal types [44].

High enthalpy geothermal plays refer to high temperatures and dominated by convection, they occur in active geological tectonics and volcanism [10]. Depending on the pressure and depth, which are correlated, convective hydrothermal resources can be categorized into vapour dominated (steam) and liquid dominated (water) systems. Convective plays consist of volcanic, plutonic and extensional domain types [44].

In figure 2-2 and 2-3 these two types of geothermal systems are visualized; conduction versus convection. Different geothermal play types can be developed by different well configurations, like single well, doublets or triplets, depending on the need of the situation [10].


1	Volcanic field type	Plutonic type	Extensional domain type
2	<i>Java-Kamojang</i>	<i>Larderello</i>	<i>Bradys (Basin and Range)</i>
3	Magmatic arcs Mid oceanic ridges Hot spots	Young orogens Post-orogenic phase	Metamorphic core complexes Back-arc extension Pull-apart basins Intracontinental rifts
	Magma chamber, intrusion	Young intrusion+extension	Thinned crust → elevated heatflow
4	Active magmatism (volcanism)	Recent plutonism	Active extensional domain
5			
6	-	Fault controlled Magmatic	+

Figure 2-2. Geothermal classification scheme for convection-dominated systems based on the geologic controls of igneous activity as magmatism (volcanic type with typus locality Java, Indonesia), recent plutonism (intrusion type with typus locality Larderello Italy in the periphery of the Alpine orogeny), and absent igneous activity but significant active extension (extensional domain type with typus locality Basin and Range, western USA.). 1 – Play type, 2 – Typus locality, 3 – Plate tectonic setting, 4 – Geologic habitats of potential geothermal reservoirs, 5 – Heat transfer type, 6 – Geologic controls. Source: Moeck (2014) [44].


1	Intracratonic Basin Type	Orogenic Belt Type	Basement Type
2	<i>Paris Basin</i>	<i>Unterhaching (Germany)</i>	<i>Habanero (Australia)</i>
3	Intracratonic/Rift basins Passive margin basins	Fold-and-thrust belts Foreland basins	Intrusion in flat terrain Heat producing element rock
	Sedimentary aquifers Permeability/porosity with depth	Sedimentary aquifers Permeability/porosity with depth Fault and fracture zones	Hot intrusive rock (granite) Low porosity/low permeability Fault and fracture zones
4	hydrothermal	hydrothermal	petrothermal
5			
6	-	Fault/fracture controlled Litho-/biofacies controlled	+

Figure 2-3. Conduction dominated geothermal play types, ranging from intra-cratonic basins to foreland basins of orogenic belts with its characteristic foredeep to basement (igneous or metamorphic) provinces. Geologic controls in conduction-dominated plays are either litho- or biofacies of sedimentary rock and faults and fractures. Typically these play types are lacking active faulting and seismicity. Labels are as in figure 2-2. Source: Moeck (2014) [44].

2.1.2 HYDROTHERMAL VS PETROTHERMAL

Zooming in on the conduction dominated systems; there is another distinction made between hydrothermal and petrothermal plays. The difference between these two is mainly based on the rock type and thus on the typical exploitation method [44].

Petrothermal systems typically consist of low porosity-low permeability crystalline rocks, like granite, and often require reservoir stimulation to make a geothermal system producible. By stimulation techniques, like fracking, permeability can be created to allow circulation between the injector and the producer, a doublet [38]. This enhancement of permeability is created by high-pressure fluid injection that mainly involves shearing of natural fractures as opposed to tensile fracturing [10]. This concept is called Hot Dry Rock (HDR) and is identified as Enhanced Geothermal Systems (EGS).

In hydrothermal systems temperatures are typically lower, between 30 – 150 °C, while the permeability and porosity is fairly high. Such an aquifer is typically at shallow depth, between 1 – 4 km. In these hydrothermal systems doublets typically one injector and one producer is used, see figure 2-4 for a schematic diagram [2]. Between these wells water is circulated at relatively low pressures. While temperatures can be high enough to be used for electricity generation in many cases it is best suitable for direct heat use, like the heating of (residential) buildings. In the sedimentary subsurface these hydrothermal systems are dominant, like they are in all the geothermal systems in the Netherlands [47].

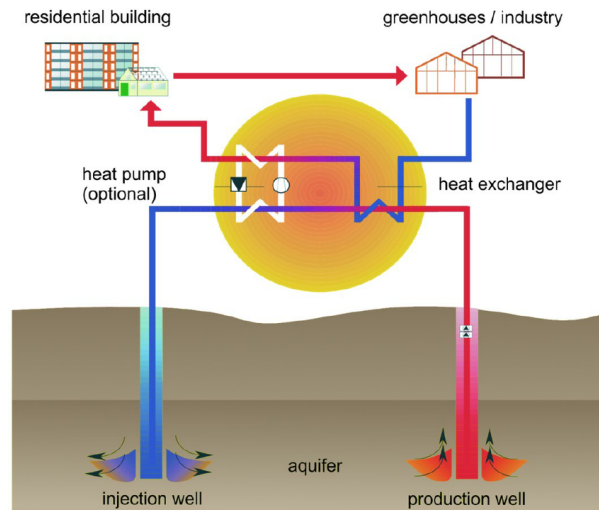


Figure 2-4. Typical diagram of a hydrothermal system, with a doublet and an optional heat pump. Source: Agemar (2014) [2].

2.2 PHYSICAL BACKGROUND OF SEISMICITY

In this section a short physical background of seismicity will be given, where later in chapter 6 a more elaborate physical description will be given to provide more technical information needed to interpret the newly developed Physical Screening Model.

The physical mechanisms underlying induced seismicity are controlled by stress changes in the subsurface caused by anthropogenic activities [6]. If the stress inside a reservoir changes and acts on a pre-existing fracture or similar zone of weakness (like weak intact rock), seismicity may occur on the fracture if the shear stress exceeds the fracture strength or frictional strength [16]. The failure process of a fracture can lead to seismic activity. The rock failure criterion defines the relationship between the material cohesion and the effective stresses acting at the point of failure [22]. The most used relationship is described by the Mohr-Coulomb failure criterion:

$$\tau = C + \mu\sigma_n \quad [2.1]$$

where τ = shear stress [Pa]

C = cohesion of the rock or plane [Pa]

μ = (internal) friction coefficient [-]

σ_n = normal stress [Pa].

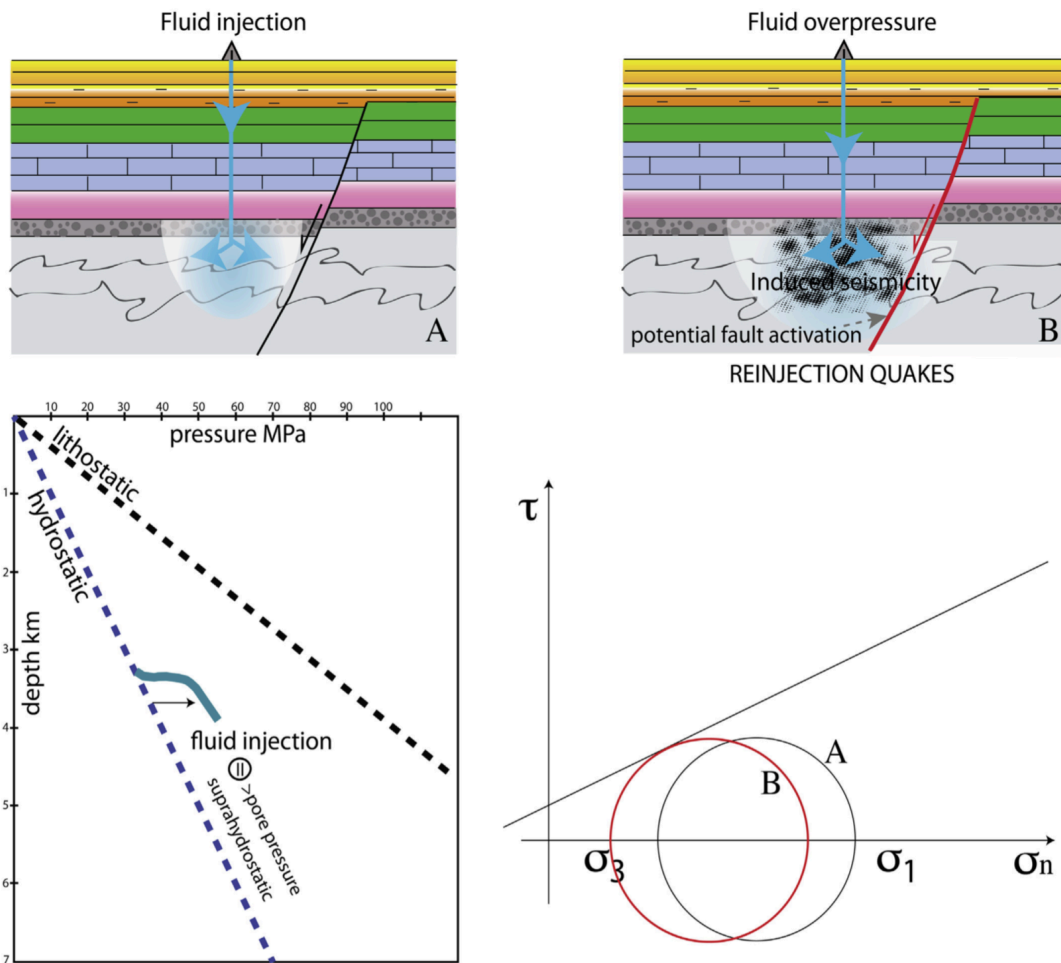


Figure 2-5. Schematic overview of fluids injection and its subsurface consequence. 1) Schematic cross-section of fluid injection in to a reservoir in the subsurface. 2) Schematic cross-section of the fluid overpressure in the reservoir as result of the injection. The stress disturbance reaches the fault close to the injection point. 3) Depth plot of the lithostatic and hydrostatic pressures in the subsurface. Due to the injection the pore pressure becomes super-hydrostatic. 4) A Mohr diagram, that shows that the fluid overpressure results a movement to the left of the initial Mohr circle, which can lead to fault instability and reactivation. Source: Doglioni (2017) [16].

2.2.1 INDUCED SEISMICITY

In general it is assumed that injection into a reservoir can induce seismicity in two ways. One is by causing pre-existing faults to slip and fail resulting in large-scale earthquakes, while on the other hand we have microseismicity, which is more related to the redistribution of the stress disturbance due to high-pressured injection resulting a series of small events in a prograding cloud moving through the reservoir [16] [25].

REACTIVATION OF FAULTS

The reactivation of pre-existing faults can cause large-scale seismicity. The existence, vicinity, and orientation (and therefore critically stressed state) of faults are crucial in identifying the hazard and the significance of the induced seismicity. From a physical point of view, our understanding of the mechanics of fault reactivation and earthquake nucleation due to fluid pressure variations is based on the concept of effective stress combined with a Coulomb failure criterion, as described in the previous section 2.2 [46]. The onset of fault reactivation is typically characterized by a critical shear stress, τ_p , given by the product of a friction coefficient, μ , and the normal stress, σ_n , applied on the fault. In the presence of fluids, this normal stress is offset by an amount equal to the fluid pressure, P , so that the fault reactivation criterion is [36] [58]:

$$\tau \geq \tau_p = \mu(\sigma_n - P) \quad [2.2]$$

$$\tau = \mu \sigma_{neff} \quad [2.3]$$

where σ_{neff} = effective normal stress [Pa]

τ_p = critical shear stress [Pa]

P = fluid pressure [Pa].

The effective normal stress σ_{neff} and shear stress τ along the fault may be defined as:

$$\sigma_{neff} = \frac{\sigma_x + \sigma_y}{2} + \frac{\sigma_x - \sigma_y}{2} \cos 2\left(\frac{\pi}{2} - \theta\right) - \tau_{xy} \sin 2\left(\frac{\pi}{2} - \theta\right) - P \quad [2.4]$$

$$\tau = \frac{\sigma_x - \sigma_y}{2} \sin 2\left(\frac{\pi}{2} - \theta\right) - \tau_{xy} \cos 2\left(\frac{\pi}{2} - \theta\right) \quad [2.5]$$

where σ_x = normal stress in x-direction [Pa]

σ_y = normal stress in y-direction [Pa]

θ = angle with the fault plane [Pa]

τ_{xy} = shear stress in xy-direction [Pa].

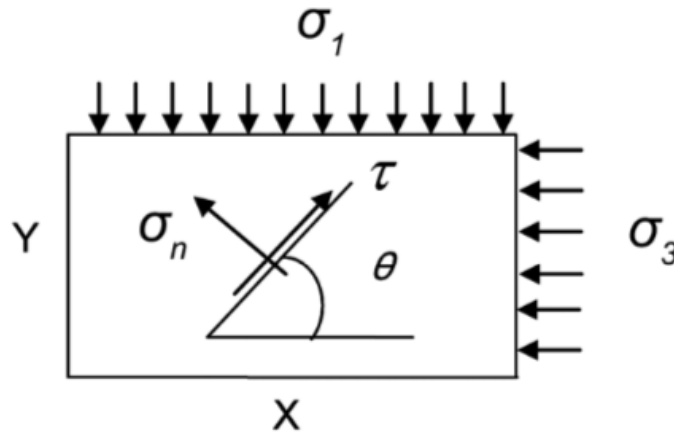


Figure 2-6. Schematic overview of the primary stresses in an angular relation to the normal and shear stress that act on a plane, i.e. fault or fracture. Source: Gan (2014) [23].

Based on the effective stress law the reactivation criterion is expected to hold, within a reasonable degree of approximation, only when the entire fault is affected by fluid pressure. Thus considering that the pressure should be homogeneous over the whole fault [46]. This means that the onset of large-scale fault motion depends on the distribution of fluid pressure, applied stresses, and elastic stress redistribution due to partial slip [14] [30].

When it comes to the reactivation of faults the type of rock can play a considerable role as well. Injection into sedimentary rocks leads to more distant and larger seismicity for a given volume of injection, perhaps because the pressure and stress transmission is more efficient [28]. For this transmission there is a difference between abrupt decay, which is limited to sites where injection is within the crystalline basement, and steady decay, which predominantly occurs above the basement in sedimentary reservoirs. This will mean that maximum magnitude is larger for sites with steady decay because of the greater probability of activating bigger faults within the extended spatial

footprint of the injection wells [28]. The risks of this effect can be enlarged by the incapability of the identification of faults within a reservoir. Big(ger) faults can be identified on seismic sections but minor faults go often unnoticed, thus these create an unknown risk when placing an injection well in the vicinity [32].

HYDRAULIC FRACTURING

With hydraulic fracturing, done in EGS, fractures are created and/or reopened; with this process microseismicity will occur. Here a diffusive process of pore-pressure relaxation in sub-critically stressed rocks triggers fluid-induced microseismicity. This will result in a distribution of microseismicity similar to observed microseismic clouds that move through the reservoir during hydraulic fracturing [50].

Microseismicity is nowadays the most efficient technique to state on the dynamic behaviour of fractures and faults when considering low magnitude geomechanical phenomena [15]. It corresponds to the energy release under body waves associated with stress release on a surface (geological discontinuity such as a natural fracture or fault plane) or associated with the fracturing and the propagation of the fracture into a continuous medium. The range of the moment magnitudes of microseismicity is usually between -3 and 2, with these extremely low energy levels it can barely be noticed by humans on surface level. Besides the always-low magnitude the definitions of microseismicity is fairly analogue to natural seismicity [15]. With the microseismicity clouds it is easy to qualitatively map structures in the subsurface like fractures and faults [15].

2.2.2 INDUCED SEISMICITY CAUSES

As described above induced seismicity is mainly caused by production or injection of water, gas or other fluids into the subsurface, but in order to predict more about the possible occurrence of induced seismicity the different physical mechanics behind these geological events need to be known. According to literature by McGarr (2002) [43], Jaeger (2007) [36] and TNO (2014) [64] there are seven different physical mechanisms that can cause fault reactivations and thus lead to induced seismicity:

- 1. Pore pressure increase**
- 2. Poro-elastic stress changes**
- 3. Thermal stress change**
4. Compaction
5. Mass changes
6. Stress transfer from nearby earthquakes
7. Chemical reaction

These mechanisms work differently for different operations within the subsurface. For instance, compaction is a dominant mechanism in gas depletion operations like the Groningen gas field. Mass changes will be minimal for hydrothermal operations as the amount of injected and produced fluids will be equal. Therefore, compaction is likewise not likely to take place during geothermal production because there is no single production and the total volume will remain equal inside the (operating) reservoir [64]. In the (West-)Netherlands (except for Groningen and Limburg) there are no earlier (induced) earthquakes observed so there will be no stress transfer from nearby earthquakes [17]. In general for geothermal/hydrothermal operations some causes are irrelevant; chemical reaction will have a minor effect in these reservoirs, as only formation-water is re-injected.

This leaves the three (bold) mechanisms that should be investigated extensively in this thesis due to its influence in geothermal operations; pore pressure increase, poro-elastic stress changes, and thermal stress change. These will be discussed in the following paragraphs.

PORE PRESSURE INCREASE

In most geothermal systems formation fluids are reinjected into the reservoir. The increasing fluid pressure at the injector in a reservoir causes pressure in the connected pore space of rocks to increase (the pore space includes pores, cracks, vicinities of grain contacts, and all other possible voids in rocks). This leads to a general increase of pore pressure at the critical locations (like faults) as well. Such an increase of pore pressure consequently causes a decrease of the effective normal stress, usually acting compressional on arbitrary internal rock surfaces like faults. This leads to sliding along pre-existing, favourably oriented subcritical cracks or faults [56]. Consequently this sliding can result in seismic activity, especially close to the injection well, where pore pressure is changed the most.

The pressure disturbance caused by the pressured injection of water diffuses into the reservoir and creates two types stress-changing mechanisms. There is a direct pore pressure changes that is most relevant close to the point of injection and induced shear stress changes, poro-elastic changes (one-way coupling between pore pressure and stress), which may dominate far from the injector but can also influence the stress change close to the well [55].

PORO-ELASTIC STRESS CHANGE

In many relevant studies and seismicity analysis of induced seismicity poro-elastic effects are under accounted for, as the directed pressure change is mostly seen as the most dominant physical mechanisms. This subsequently the poro-elastic modification to the full stress tensor arising from pore pressure gradient acting as a body force is widely neglected [37].

Pore pressure diffusion into hydraulically connected, permeable faults dominates their mechanical stability [12]. For hydraulically isolated or low-permeability faults, however, poro-elastic stresses transmitted to deeper basement levels can trigger slip, even without elevated pore pressure [12].

WHAT IS PORO-ELASTICITY?

Porosity-elasticity can be described as follows: "Porosity-elasticity is the term used to describe the interaction between fluid flow and solids deformation within a porous medium. When an external load is applied to a porous medium, the volume fraction of the pores is affected. The fluid-filled pores experience a change in pressure under this mechanical stress, which, in turn, leads to fluid motion. As a reaction to this change in pore volume, the solid material shifts and deforms elastically." (Comsol cyclopedia) [13]

In other words, this describes porosity-elasticity as the physical process of rock deformation as well as fluid flow through deformable pores. Porosity-elasticity involves coupling of equations for deformation of the solid matrix (Biot) with those governing pore fluid flow (Darcy) [12].

HOW DOES PORO-ELASTICITY RELATE TO SEISMICITY?

As cited before, most models neglect porosity-elastic stress changes associated with injection, assuming that direct pore pressure changes are the dominant effect in destabilizing faults. However, indirect transfer of stress may disturb faults even without direct diffusion of pore pressure into the faults [37]. Elasticity is an effective means of transmitting forces to great distances, and therefore the fully coupled porosity-elastic stress field can extend well beyond the fluid pressure increase in the

hydraulically connected region [28]. According to Brody [28] and Jin [37], the most important reason to include poro-elasticity into induced seismicity models is because of its extensive disruptive reach into the subsurface.

Another reason to incorporate the poro-elastic coupling is its significant decreasing factor it still has on seismicity closer to the well. According to Segal (2015) [55], the effect of poro-elastic coupling on the seismicity rate is understood, as follows: Increased pore pressure near the injector causes the rock to expand volumetrically, the poro-elastic behaviour. This expansion leads to radially outward displacements, which decrease with distance from the injector. Thus, the radial strain, and thus stress, are compressive. Along a certain direction, that is perpendicular to a fault, horizontal compression increases the faults normal compression for (critically) striking normal faults. The shear traction on the faults also decreases; both effects decrease the Coulomb stress, the stress that predicts seismicity. The uncoupled solution ignores this effect and thus over predicts the seismicity rate ahead of the large pore pressure changes [55].

According to Jin 2015 [37] the result of the poro-elastic coupling can be different depending on the location of the fault: Inside the excessive pressure front (the distribution of changes in fluid pressure, so extent of the fluid pressure disturbance), fractures act as fluid sources, generating a pressure gradient (an equivalent body force) acting towards the fractures, thus poro-elasticity tends to reduce seismicity; Outside the excessive pressure front, poro-elasticity can remotely promote or reduce seismicity, even though this area is not in physical contact with the fluid [37].

Thus it is imminent to include poro-elastic coupling into calculations for induced seismicity due to fluids injection.

THERMAL STRESS CHANGE

From the theory of thermodynamics thermoelastics is derived. This theory describes the effects of the change of temperature on a body, in this case on a rock. It looks at the stress change and displacement and is very similar to the poro-elasticity theory described above [36]. Both theories are governed by fairly similar equations for diffusion, more on this is chapter 6 and 7. In geothermal cases thermodynamics comes into play when rock is intensively cooled due to cold-water injection. This results in the thermal contraction of the rock (and of its void space like pores and fractures), which leads to a reduction of normal stress and an increase of shear stresses [27]. Depending on a number of parameters like thermal properties of the rock and fluids, difference in injection temperature and reservoir temperature, etc. the severity of the thermal effect can be calculated, further information on this in chapter 6.

3. SUBJECT OF INVESTIGATION

In order to summarize the subject of investigation of this thesis; it essentially consists of three different but interdependent studies:

1. **The description and evaluation of three SRA methodologies currently used for geothermal operations:** This thesis starts with the portrayal of the currently used SRA methods that are used in the Dutch geothermal (and petroleum) industry. The SRA's of SodM and Q-con/IF as well as the model created by TNO/Geomech are then further analysed, while its advantages and disadvantages are being exposed. Performing this dissection will be beneficial in the second part of this thesis, the creation of a new SRA.
2. **The design of an improved and more physically based SRA:** In the creation of this new SRA methodology the focus will solely be on the potential seismicity that can occur due to the reactivation of existing faults during geothermal operations in the Netherlands. This SRA will provide a step-by-step catalogue that should be used by operators before starting production or injection.
3. **Within this SRA, the creation of a simple Physical Screening Model that can perform a quick but reliable scan for seismic hazards:** The last and most extensive part of this thesis will describe the development of an analytical Physical Screening Model (PSM) that provides a more physical picture in the reactivation of faults than previously developed models in the Netherlands. Most current models neglect or underestimate poro-elastic stress changes associated with injection; assuming that direct pore pressure changes and temperature change are the dominant effect in destabilizing faults. However, indirect transfer of stress may perturb faults even without direct diffusion of pore pressure into the faults. Fluid injection can induce seismicity by changing stress fields in rocks adjacent to the storage formation due to poro-elastic coupling [55] [37].

In other words, this thesis will

create an analytical Physical Screening Model for seismic hazards to find the extensive reach and the strength decay of the direct pore pressure, poro-elastic effects and the thermodynamic effects in a homogeneous sedimentary aquifer, and how these changes influence the reactivation of a fault near (in direct flow connection) or far (sealing/low permeable faults i.e. in the basement rock underneath) from the injection point. This Physical Screening Model will be part of a new SRA methodology, which can be used to identify the seismic risks for geothermal projects in The Netherlands.

4. SRA METHODOLOGIES

In the Netherlands there are currently multiple Seismic Risk Analyses methodologies being used in advance of/ or during geothermal operations. This inherently means that there are different ways to quantify seismic hazards and risks related to a geothermal operation.

To ultimately develop an effective new methodology for seismic risk assessment in geothermal operations, it is important to first describe and evaluate three most commonly used methodologies at the moment the:

1. SodM approach [59]
2. Q-con/IF-technology approach [6]
3. TNO/Geomech model [64].

4.1 SODM METHODOLOGY

The ‘Staatstoezicht op de Mijnen’ (SodM) created a seismic risk analysis by order of the “Ministry of Economic Affairs and Climate” of the Netherlands, ultimately named: “Methodiek voor risicoanalyse omtrent geïnduceerde beving door gaswinning”. This request was made in order to diminish the seismic risk related to gas exploitation, but can therefore also be used for other reservoir producing industries, like geothermal operations.

The SodM methodology is a proper guide when it comes to the structure of the step-by-step plan, displayed in figure 4-1. This methodology is a handbook that only gives a guideline to map the seismic risk and it is not a review of this seismic risk. So it should rather be seen as a guidebook instead of an evaluation method for the investigation of seismic activities in gas (or oil) producing reservoir.

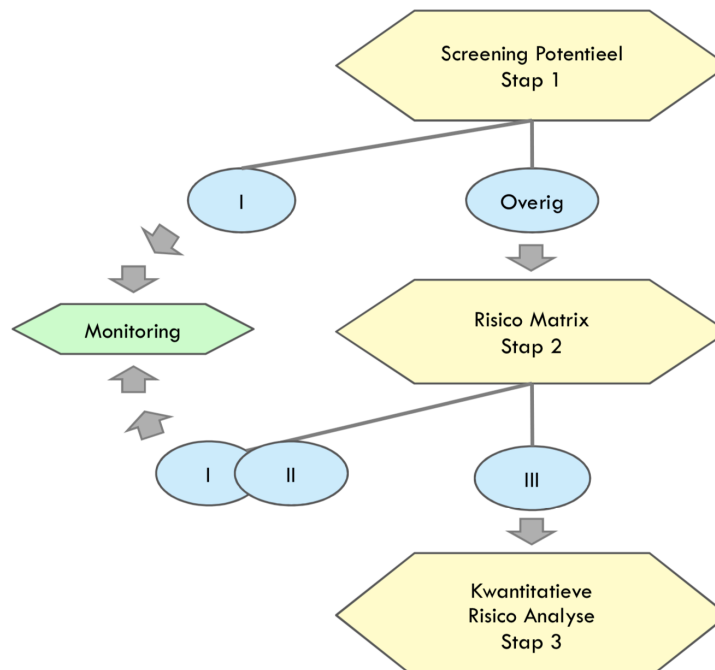


Figure 4-1. Display of steps that should be followed in the SRA of SodM. The roman numbering corresponds with the level of monitoring to be done. Source: SodM (2016) [59].

Figure 4-1 shows the step-by-step SodM methodology. Step 1 starts with screening for the potential of seismic activity; looking at the statistical correlation between parameters of field characteristics for the occurrence of induced seismicity. Based on two ratios and one single parameter the seismic hazard is determined and whether induced seismicity may occur in a production field:

- DP/P_{ini} : Ratio between pressure drop (DP or ΔP) and initial reservoir pressure (P_{ini}).
- E: relation between Young's moduli (E) of the overburden rock and reservoir rock.
- B: Fault density in the reservoir.

The results from the parameters above are then examined in Table 4-1 and the first hazard assessment can be made.

4-1. The risk table of the SodM SRA. When the DP/P_{inj} ratio is above 28% the likelihood of seismicity depends on E, B and P. If the DP/P_{inj} ratio is below 28% the likelihood of seismicity is negligible. Source: SodM (2016) [59]

Reeds bevende voorkomens	
$DP/P_{ini} \geq 28\%$	B > 0,86 en E \geq 1,34: $P_h = 0.42 \pm 0.08$
	B > 0,86 en $1,01 \leq E \leq 1,33$: $P_l = 0.19 \pm 0.05$
	B < 0,86 en/of E < 1,01: verwaarloosbare kans
$DP/P_{ini} < 28\%$	Verwaarloosbare kans

Subsequently there is research done into the magnitude of the induced seismicity based on the existing faults in the reservoir and the compaction of the reservoir. This is computed by two different methods. The first method considers the fault geometry and the correlation between the stress drop caused by a seismic event and the seismic moment using this equation [9] [60]:

$$M_o = GAu = \frac{3\pi}{8} \Delta\sigma(w^2L) \quad [4.1]$$

where M_o = seismic moment [Nm]

G = shear modulus [Pa]

A = total area of the fault over which the slip takes place [m²]

u = average slip of the fault [m]

$\Delta\sigma$ = stress drop [Pa]

w = height of the fault [m]

L = length of the fault [m].

In combination with the following equation [9]:

$$10\text{Log}(M_o) = 9.1 + 1.5M \quad [4.2]$$

where M = the magnitude of the seismic event [-].

The second method examines the energy balance resulting from volume change (ΔV) inside the reservoir. The volume change leads to compaction and thus to a seismic moment. Using the next equation [40] [8]:

$$M_{0,T}(t) \cong \frac{4G}{3} \alpha |\Delta V(t)| \quad [4.3]$$

where $M_{0,T}(t)$ = maximal seismic moment [Nm]

α = Biot-Willis coefficient [-]

and similar to the first method, also:

$$10\text{Log}(M_o) = 9.1 + 1.5M \quad [4.4].$$

If seismic magnitudes of 2.5 or less are expected, no further studies are required, besides the monitoring of the operations. If seismic magnitudes of 2.5 or higher are expected, step 2 will have to be executed as well. In this step 2, the risk of an induced seismicity is quantified by using a risk matrix. This matrix consists of a normalized quantification analysis of the influence factors of the subsurface and surface. This is done by an elaborate grading system. Figure 4-2 shows what the influence factors of the subsurface and surface are, while figure 4-3 shows a plot, the risk matrix, with the normalized quantifications of the two.

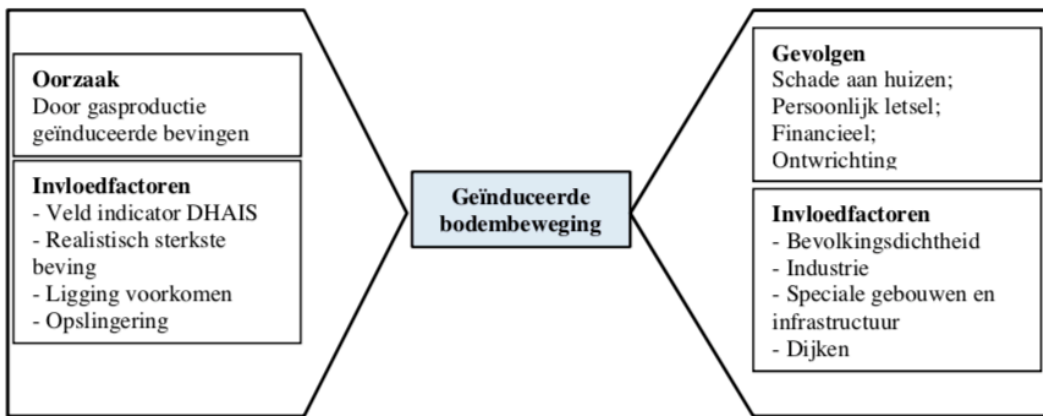


Figure 4-2. Schematic representation of the threats and consequences of induced seismicity and the various influencing factors that play a role in that. Source: SodM (2016) [59].

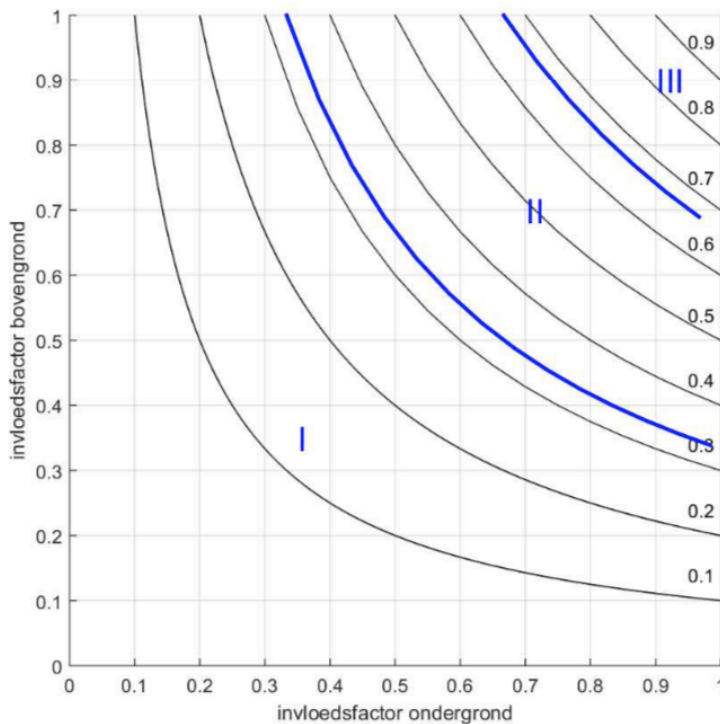


Figure 4-3. The risk matrix. The black lines are lines of equal normalized risk. The division into categories is simply done on the basis of 1/3 and 2/3 of this normalized risk. Source: SodM (2016) [59].

When the result of the grading systems falls into section I or II only screening is needed, when it lies in section III, step 3 will need to be evaluated. Step 3 contains more reservoir individual quantitative risk analysis, including dynamic modelling.

The first and second step will be most interesting for this thesis when investigating the potential seismic hazard. Most interesting is the screening potential from step 1 and the risk matrix used in the second step. As discussed before; as this risk analysis is for evaluating the seismic potential resulting from oil and gas production, some parameters are irrelevant when creating a similar methodology for geothermal operations, like the ratio of pressure drop and initial drop (DP/P_{ini}), because there will not be any pressure drop over the whole reservoir due to depletion in geothermal reservoirs.

When reviewing the influencing factors from step 2, the same conclusions can be drawn when using this methodology for geothermal purposes; geothermal operations require slightly different parameters; like for instance the importance of induced seismicity due to the intensity of the water injection, because of the heavy injection rate used in geothermal operations.

Thus the framework of the SodM methodology is useful when creating a similar framework for geothermal fields instead of gas fields. As this method is built for the seismic risk and hazard evaluation of gas exploitation, it is not as well suitable for geothermal operations. While most of the physical and theoretical background should overlap some important physical differences have to be taken into account.

4.2 Q-CON/IF METHODOLOGY

The second methodology, the Q-con/IF report, is specifically made as a protocol for seismic risk associated with geothermal systems in the Netherlands. The Q-con/IF protocols main aim is “to assist project developers in understanding and mitigating these seismicity risks”. This protocol is based on theoretical concepts and on a data set provided by global observations, geological and operational parameters. On these foundations a three-level procedure for addressing the seismic risk is build.

The Q-con/IF report follows a three level approach for seismic hazard and risk assessment. In figure 4-4 the three levels are visualized, step-by-step. Level 1 is an initial estimation of the induced seismicity potential, which is obtained by “yes/no questions” and a Quick-Scan of key-parameters. Level 2 is a guideline for a location-specific Seismic Hazard Assessment (SHA) in case level 1 indicates a medium or high risk potential. If the outcome of the level 2 SHA is not acceptable, level 3 will go into a full Seismic Risk Assessment (SRA).

Most relevant for this thesis research is the usage and interpretation of the parameters used in the Quick-Scan, because this research main focus is the physics behind the seismic hazards. Level 1 refers to this Quick-Scan for obtaining a rough estimate of the induced seismicity potential associated with geothermal operations.

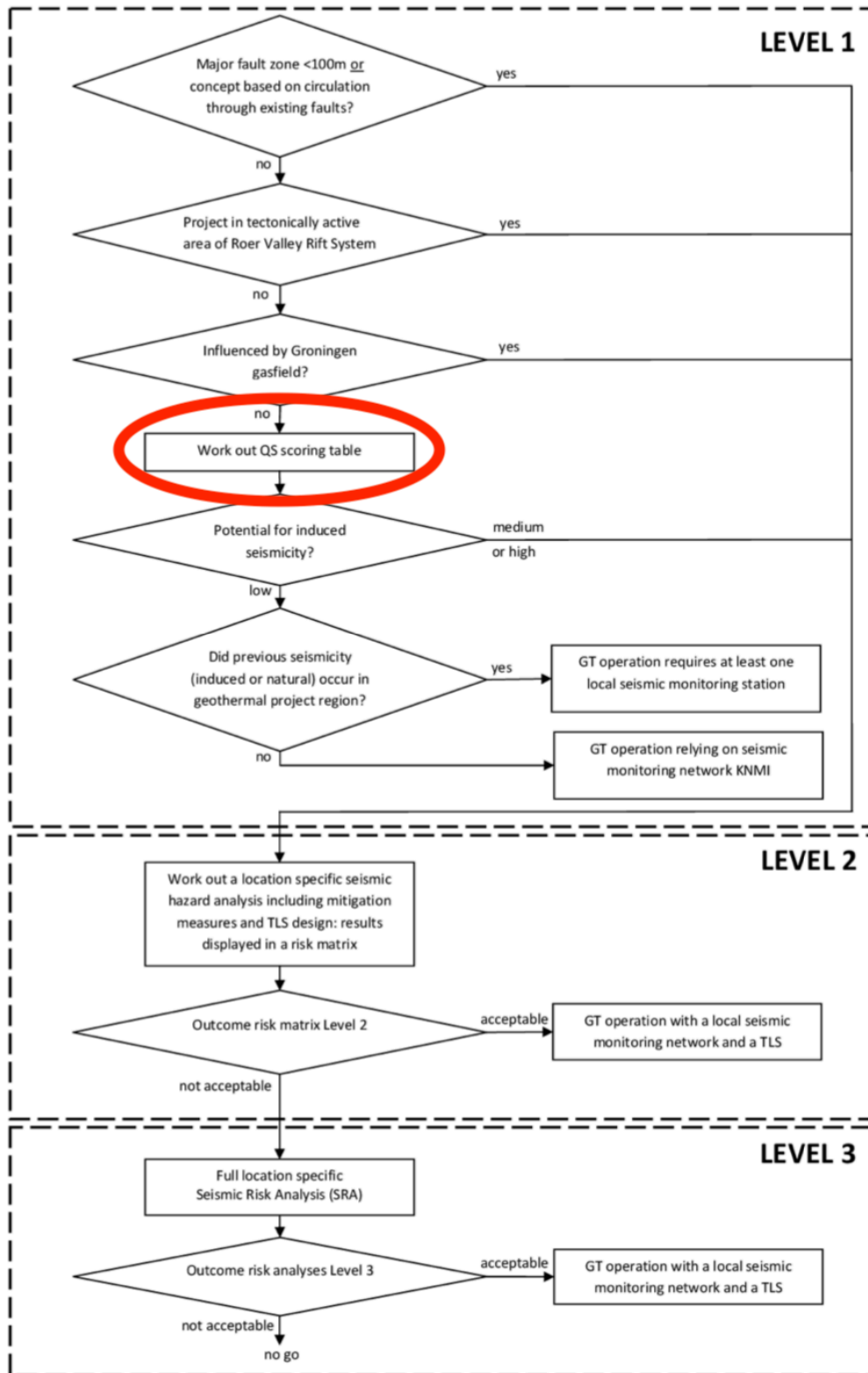


Figure 4-4. Display of the consecutive levels of the Q-con/IF SRA Methodology. Circled in red is the Quick-Scan, which is part of level I of the Q-con/IF SRA. Source: Q-con/IF (2017) [6].

Table 4-2. The quick scan table. The nine parameters in this table should be reviewed with scores of 0, 3, 7 or 10, depending on the argument inside the table box. Source: Q-con/IF (2017) [6].

score	basement connected	inter-well pressure communication	re-injection pressure [MPa]	circulation rate [m ³ /h]	epicentral distance to natural earthquakes [km]	epicentral distance to induced seismicity [km]	distance to fault [km]	orientation of fault in current stress field	net injected volume [1000 m ³]
10	yes	no	> 7	> 360	< 1	< 1	< 0.1	favorable	> 20
7	possible	unlikely	4 - 7	180-360	1 - 5	1 - 5	0.1 - 0.5	shearing possible	5 - 20
3	unlikely	likely	1 - 4	50-180	5 - 10	5 - 10	0.5 - 1.5	shearing unlikely	0.1 - 5
0	no	yes	< 1	< 50	> 10	> 10	> 1.5	locked	< 0.1

The Quick-Scan table, Table 4-2, separately evaluates 9 different parameters that may influence the seismicity. All the 9 parameters are listed further below. They are investigated on how much influence and value each parameter has. This qualification is not done in the Q-con/IF report, where the scores are simply summed and placed in a seismic potential plot, see figure 4-5. This plot will give an approximation on if the seismic hazard is either low, medium or high, after which potential further steps (level 2 and 3) should be taken.

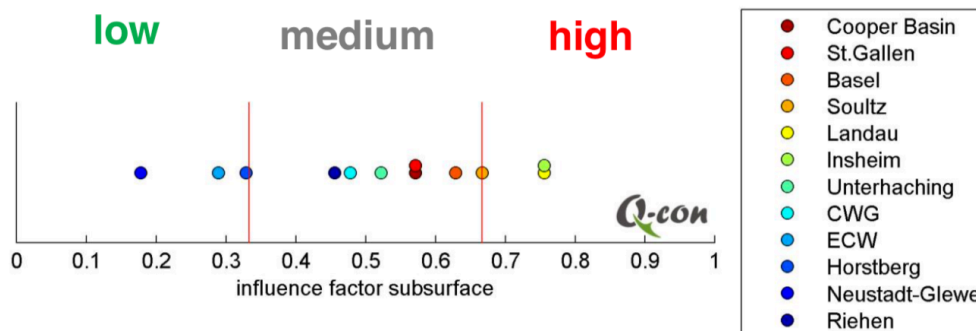


Figure 4-5. Scoring plot of the normalized Quick-Scan table results. In this example the Quick-Scan is applied to certain geothermal projects. Each coloured dot represents the seismicity potential of a geothermal project as listed in the legend. Projects are sorted according to the maximum seismicity magnitude associated with the project, with the warm colours representing large magnitude, and cold colours representing no seismicity. Source: Q-con/IF (2017) [].

The 9 parameters are listed and explanation below, while its relevance is discussed:

1. **Basement connection** - The crystalline basement that lays below the deposited sediments is commonly is a critical stress state, and thus can small stress perturbations result in induced seismic activity [65]. As the basement rock in most of the Dutch subsurface lays very deep (in the south Holland basin around 7 km deep) the significance of this parameter will be low in most parts of the Netherlands. However, when the basement is considerably closer to the reservoir, for instance when ultra-deep hydrothermal systems are considered, the basement connection can be most relevant for the SRA. The importance of basement connection also depends on the spatial footprint of the far-reaching poro-elastic effect, which is considerably higher in sedimentary rock with high porosity; injection into sedimentary rocks can lead to more distant and larger seismicity for a given volume of injection [28], as described in the previous chapter.

2. **Inter-well pressure communication** - This parameter provides an indication whether communications, flow connection, between the injector and the producer in a geothermal field is good, and if there are any barrier that may constrain this communication. Considering a field with a fairly good overall permeability and a relative small distance between the injection and production well, the inter-well communication can be considered to be good. In this case no reservoir enhancement is needed or high-pressure concentrations are created (except for possible “invisible” faults but this will be reviewed later on). This parameter cannot be physically quantified and thus is not suitable for inclusion in a simple seismic screening model. It can be however important in the viability of a geothermal project, because non-communicating wells can simply not be used in hydrothermal systems.
3. **Reinjection pressure** - This parameter is in general considered to be one of the most if not the most important parameter when investigating induced seismicity. In principle, the re-injection pressure controls the level of overpressure, in ΔP , in the reservoir formation. The specific physical relation between the overpressure and the seismic activity is strong; this will be shown in later parts of this research. As explained before the re-injection pressure causes stress changes in the reservoir that may reactivate existing faults. This parameter is easily physically quantifiable and thus can be included in a simple seismic screening model.
4. **Circulation rate** - According to Darcy’s law, see Eq. 6.20 in section 6.6, the (injection) pressure and the permeability relate to the circulation rate. Considering the inter-well connectivity to be good, in a homogeneous reservoir, and the net injection volume to be zero (the injection volume and production volume are the same), the circulation rate will have very limited influence as correlation with induced seismic activity is not obvious [47] and therefore held constant in this model. This parameter will therefore be combined with the reinjection pressure and the permeability when used in physical calculation.
5. **Epicentral distance to natural earthquakes** - Except for Limburg (and also parts of eastern Brabant) natural seismicity is lacking in the Netherlands [17], making this parameter redundant for most parts of the Netherlands. However the roll of the regional stress gradient has big influence on the determination of fault reactivation. An increase of the confining pressure and/or initial shear stress enhances the fluid pressure required at the injection site for fault reactivation [46].
6. **Epicentral distance to induced seismicity** - Here the same argument holds. It gives a better quantification of seismic hazard when the local stress orientation and levels are known.
7. **Distance to a fault** - Fault vicinity is crucial when looking at the reactivation of these faults. In this case it is not only relevant what the location of the fault is in terms of meters from the injector but also how far the pressure disturbance can “reach” in certain reservoirs [28] and what the ability of the rocks to transmit fluid stresses into the solid material is, the Biot-Willis coefficient, and the behaviour of the pore pressure away from the injector, diffusion [53] [57] All these factors (and more) make the “distance” to a fault a very relative concept, which should be investigated more closely.
8. **Orientation of fault in current stress field** - The orientation with respect to the current stress field in the subsurface is an important factor as high seismic activity and largest magnitudes occur on favourably oriented faults with large instability coefficients and low slip misfit angles, but seismic events are also registered with severely disoriented faults. Thus faults activated by fluid injections, and thus pressure disturbance, may display a broad range in orientations [42].
9. **Net injected fluid** - The net injected volume can be defined as the difference between injected and produced fluid volume. As well as the circulation rate we assume that the net injected volume is 0 and will always have this number and therefore will not be included in this investigation.

In this grading system, by giving all the parameters the same weight of importance there is no distinction made between what parameters have more influence on inducing seismicity than the others in different scenarios. There is no difference made between physical input parameters like 're-injection pressure' and inalterable parameters like 'distance to a fault', potentially giving the operator a range to which the geothermal reservoir can be graded when it comes to seismic hazard assessment. Additionally, while the parameters are all graded separately many of them are strongly connected with each other. For instance, the 're-injection pressure' and the 'circulation rate' have a strong physical relation where one influences the other (i.e. when raising the circulation rate one has to raise the re-injection pressure when keeping the permeability the same) or the 'net injected volume' and the 'inter-well pressure communication' (i.e. when there is bad inter-well connection the water will not flow from the injector to the produces leaving an automatically high net injected volume). By not accounting for these interconnections between the parameters the scoring will subsequently be exaggerated.

For this thesis, and the creation of an PSM, the main focus of this second methodology, the Q-con/IF report, will be lying on the following parameters:

- Injection pressure,
- Circulation rate,
- Distance to fault,
- Orientation of the fault

(all outlined in red in the Table 4-3). These are the parameters that should be included as variables in a simple Physical Screening Model for seismic hazards, in which these parameters will not be separately looked at separately but will be described in a physical analytical model.

The other parameters; basement connection, inter-well pressure communication, epicentral distance to natural/induces seismicity and net injected volume, will not be handled in this physical analytical model, because the lack of physical quantification of these parameters as well as its little influence in the current west-Netherlands subsurface or will remain constant (or 0) when modelling the risk of HSA geothermal systems in the west-Netherlands subsurface. Important is to note that these parameters can be very influential in other (non HSA) systems in different areas of the country or the world but will be neglected or held constant in the physical model part of this research. When for instance a geothermal project is developed in, or close to, the basement and enhancement of the permeability is needed, e.g. with EGS, then the parameters 'basement connection' and 'inter-well pressure communication' will be very important in the hazard assessment. The figure below shows which parameters will have significant influence in this further thesis and which will not.

Table 4-3. The result of the evaluation of the Quick-Scan. The red outlined parameters are physically close related and should be merged into a quantifying model, as done in this thesis. The black crossed parameters are still significant for predictions of induced seismicity, but are less related to one another and therefore will not be included in a physical model.

score	basement connected	inter-well pressure communication	re-injection pressure [MPa]	circulation rate [m ³ /h]	epicentral distance to natural earthquakes [km]	epicentral distance to induced seismicity [km]	distance to fault [km]	orientation of fault in current stress field	net injected volume [1000 m³]
10	yes	no	> 7	> 360	< 1	< 1	< 0.1	favorable	> 20
7	possible	unlikely	4 - 7	180-360	1 - 5	1 - 5	0.1 - 0.5	shearing possible	5 - 20
3	unlikely	likely	1 - 4	50-180	5 - 10	5 - 10	0.5 - 1.5	shearing unlikely	0.1 - 5
0	no	yes	< 1	< 50	> 10	> 10	> 1.5	locked	< 0.1

Step 2 and 3 will not further be evaluated as this contains a more individual reservoir approach of each geothermal system.

4.3 TNO/GEOMECH MODEL

The third methodology is a model built by TNO, to quickly look at the seismic hazard created by some operating parameters. This model looks at the maximum tolerable injection pressure and injection temperature. It determines whether the pressure and temperature differences do not create fractures or if there is a chance to reactivate faults when injecting in this fault. Not only can fracking lead to (micro)seismicity but it can also crack the seal and lead to contamination of other shallower aquifers.

In short the tool works by entering 3 kinds of parameters, from that it creates a general pressure graph like the figure below and ultimately it calculates the different Mohr-Coulomb circles from the initial situation and that of the situation when injecting is started. The parameters are divided in:

1. Depth and pressure parameters
2. Temperature parameters
3. Rock parameters

To conclude if there is a possibility of (re-)activation of faults or fracking it simply states “NO” if the Mohr-Coulomb failure envelope is not broken and “YES” if the failure envelope is broken. The figure below shows the difference in this graph.

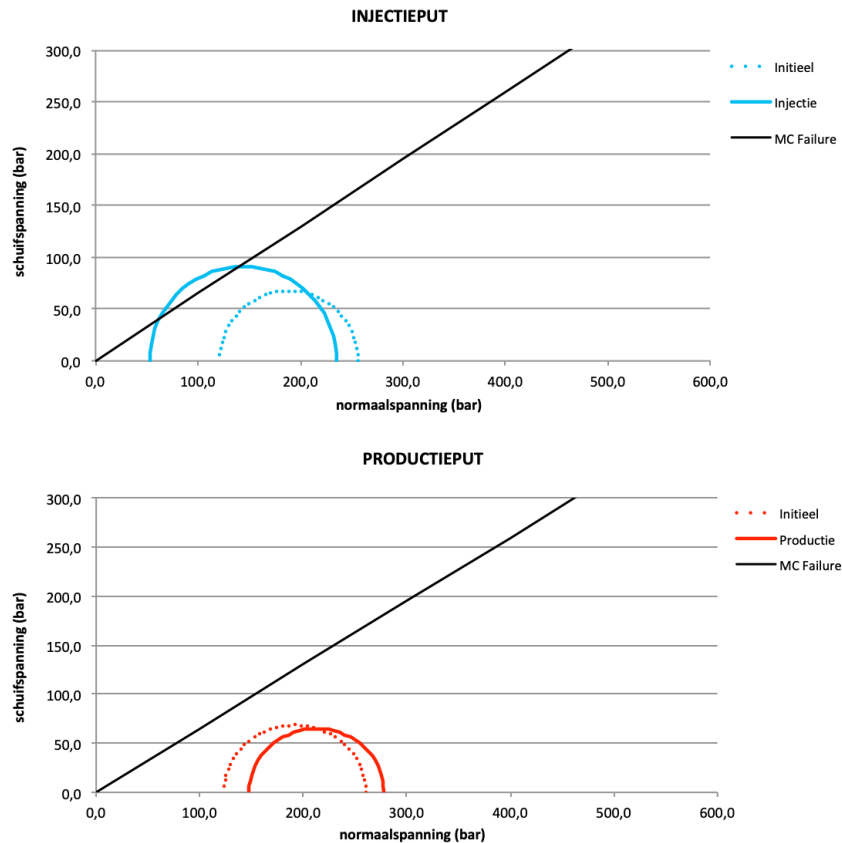


Figure 4-6. The Mohr plot results of the TNO/Geomech model. 1) Normal Mohr plot, including a Failure envelope and the initial Mohr circle and the Mohr circle after injection. 2) Mohr plot in which σ_2 is also included; creating 3D Mohr circles. Source: Excel sheet TNO/Geomech model.

Table 4-4. Output example of the TNO/Geomech model. Here the two main questions are answered; is there fracking and is there a chance on fault reactivation. Both are answered with 'NO' in this case.

Uitvoer	Waarde	Validatie
Tubing Head Pressure toegestaan volgens SodM protocol	60	JA
Maximale verschilddruk injectieput top reservoir	69	JA
Fracking		NEE
Kans op breukreactivatie		JA

There are a couple of complications and oversimplifications when working with this tool that will be discussed in the following enumeration:

1. **Simple “YES” or “NO”** – This tool simple gives a prediction of the (re-)activation of faults or fracking. First of all the “chance” of this reactivation is not quantified, it does not say that there is little chance or that there is a substantial chance. More detailed and specified analysis would give a better insight.
2. **Orientation of the fault** – As discussed in 4.2 there are two very important factors with respect to fault when evaluating the possibility of (re-)activation. These are the location of the faults (the distance to the injector) and the orientation of the fault with respect to current local stress regimes. Both of these factors are ignored in the TNO/Geomech tool, the assumption is made that the fault is in critical stress state and located at the location of the injector.
3. **No pressure decay** – The location of the fault is not evaluated in this tool as disused in the second bullet-point, this automatically means that there is no distance between the injector and the fault, which leads to the conclusion that pressure decay is not taken into account. More about the importance of this absence will be discussed in the next chapter

4. **Only direct (pore) pressure change** – The only factor influences the possible reactivation of the fault is the direct pressure change created by the overpressure from the injector. As more contemporary literature suggests [28] [55] [37] [12] that the ignored poro-elasticity could have a significant effect on (de)stabilizing faults especially in a sedimentary, high permeability, reservoir (close to the basement) relative far from the injector. More about poro-elasticity in the next chapter.
5. **Homogeneity** – Another big assumption made by the model is the homogeneity of the aquifer. To all reservoir geologist it is obvious that homogeneous sedimentary reservoir do not occur in the subsurface, but this is an assumption I can live with because of the lack of definitive information there is about these reservoirs especially on the scale we are dealing with. Of course there the aim to create a model that represents the heterogeneity of for instance a fluvial aquifer but one can never be sure if this is true, so numerical analysis is needed in that case.
6. **Magnitude prediction** – Besides the “YES” or “NO” the tool gives on the reactivation of a fault or fracking it states nothing about the magnitude of the induced seismicity this eventually leads to, which is off course the ultimate goal of a predicting tool like this. The “YES” or “NO” not only doesn’t give us a quantified “chance” indication (discussed in point 1) but is also refuses to indicate what this reactivation of a fault might possibility cause in terms of seismic moments.

Concluding on this model; all the assumptions this TNO/Geomech excel sheet tool makes a very simplified prediction model is created. Expanding and improving this model on the point discussed above, a better quantified prediction on the hazard of seismic activities can be given.

4.4 COMMON EVALUATION OF THE SRA METHODOLOGIES

Three SRA methodologies are described in the previous section. In this section a common evaluation will be carried out with the goal to define an improved SRA for geothermal operations in the Netherlands, which is the goal of this thesis. The following elements of the existing SRA methodologies will be used to define an improved SRA for geothermal operations:

- **Structure** – The SodM and the Q-con/IF methodology use similar structures. These structures contain a three-step evaluation. With in the end, step 3 being the most forceful and time consuming step where modelling and more investigating is needed to ensure the risk of seismicity is not passing an agreed limit. While the Q-con/IF methodology is starting with an arbitrary grading system (Quick-Scan), the SodM method is directly calculating potential seismic moments. Here the latter will give a more physically based number, where preliminary conclusions can be drawn from. The use of incremental steps (related to the severity of the seismic risk potential in an geothermal project) within the SRA’s seems a logical way of constructing a new SRA methodology.
- **Parameters** – The Q-con/IF report gives a clear and complete assembly of parameters that influence the potential seismicity of geothermal project. While the grading system, the Quick-Scan, does not take into account the physical interdependence of the parameters, as discussed before, the key parameters that are being used are well identified and will be used to define a new SRA methodology.
- **Calculation** – The methodology from TNO/Geomech was not really a full SRA methodology, rather a tool or model that could be part of a methodology. While this TNO/Geomech methodology is missing some significant parts and steps, this calculator is a useful tool, and a similar Physical Screening Model can be used to define the new SRA methodology.

5. NEW SEISMIC RISK ANALYSIS METHODOLOGY

In order to make a geothermal project a success, there has to be a strict planning. A project starts with a preliminary study, then the feasibility study, the exploration, field development and finally the start-up. During the feasibility study data is acquired and the project is cleared on financial analysis and risks quantification. In this part a risk analysis is included, which encompasses a SRA. With a SRA approach the project will be validated for any need of production changes or if extra research is needed to further investigate the subject.

Combining, changing and improving the three risk approaches reviewed in chapter 4, a new SRA methodology will be designed in this chapter. The convenience of this approach will be in the fact that it is quick and easy to handle. Changing certain parameters for different fields or simply to investigate different sensitivities of these parameters should be simple and easy for every operator. Apart from being quick and simple another practicality should be its applicability and accuracy. Without intensive modelling of the reservoir or its production process, this model will provide a decent indication of what seismic reaction due to fault reactivation can be expected in a simplified reservoir when producing (and injecting) at a constant rate.

RISK AND HAZARD

A hazard is associated with something that can cause harm, in this case that is induced seismicity caused by geothermal operations. While risk is the likelihood a hazard can cause harm. Thus, in this particular case this means that first the hazard must be investigated; i.e. what happens when water is injected into a reservoir, does seismicity occur and what would be the potential magnitude. After that the risk of occurring seismicity can be calculated; i.e. how big is the chance seismicity that occurs and what damage will the environment (and consequently its inhabitants, humans and animal) endure due to this seismicity. In this thesis primarily the hazard will be investigated, the physical nature of the induced seismicity due to geothermal projects. The risk of such an event happening and its environmental, financial and humanitarian results will not be investigated, although the groundwork will be laid out in the newly designed SRA.

5.1 SRA STEP 1

The new SRA will directly start with a Physical Screening Model (PSM), similar to the TNO/Geomech tool, and a Quick-Scan scoring table, similar to the Q-con/IF report. Figure 5-1 shows the complete step-by-step plan of the new SRA. With the Physical Screening Model the potential reactivation of faults over the whole reservoir during production will be evaluated; this will be the physical part of the first step in the SRA (SRA Step 1A). The second part of this first SRA step is a Quick-Scan of the missing physical parameters or non-physical parts in the risk approach (SRA Step 1B). Both the Physical Screening Model and the Quick-Scan scoring table should be computed before continuing to SRA Step 2 or directly to SRA Step 3. In order to continue directly to SRA Step 3, both the assignments (SRA Step 1A & B) need to pass, if one of those fails more investigation into the SRA is needed and SRA Step 2 will be up next.

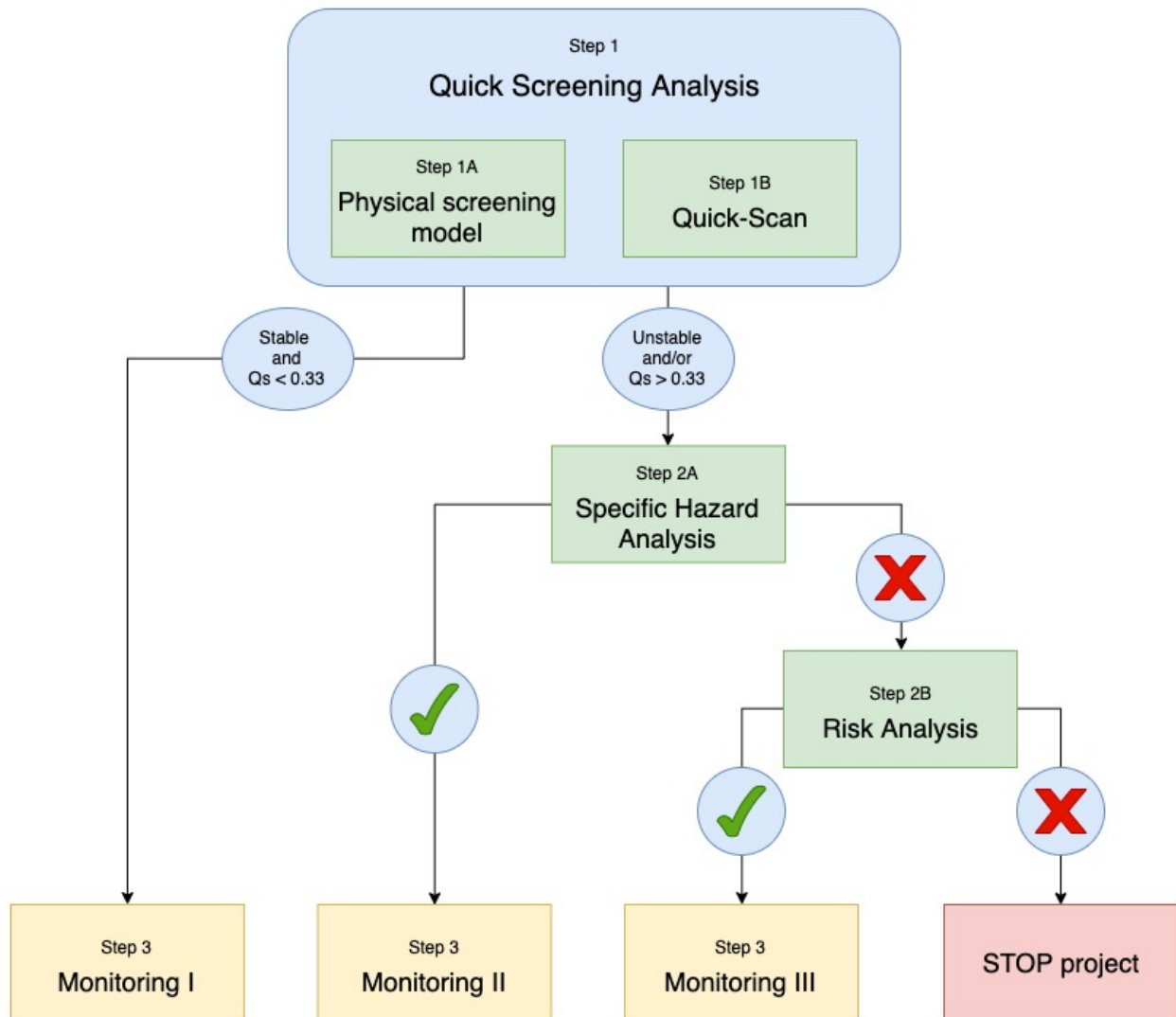


Figure 5-1. The steps that should be followed according to the new SRA.

PHYSICAL SCREENING MODEL (PSM) (SRA STEP 1A)

In a Physical Screening Model (PSM) the three hazardous physical mechanisms for geothermal production that can trigger such an event will be evaluated at any location and moment after injection. These mechanisms are the direct pore pressure, poro-elasticity and thermoelasticity (see section 2.2.2). The most important physical parameters of this model correspond to the four red outlined boxes in Table 4-3 of the Q-con/IF Quick-Scan table. Eventually, the model will provide:

1. a Mohr plot, which will show if the fault is stable or unstable,
2. the maximum Moment magnitude (M_w) combined with its,
3. Peak Ground Velocity (PGV) related to the potential seismicity.

The combination of the three outcomes will indicate whether a Specific Hazard Analysis is required (SRA Step 2A) or if the project can continue with only monitoring of the operations (SRA Step 3, Monitoring I). The full background on physics of the model will be described in chapter 6 while the working mechanism steps of the model and its results are specified in chapter 7.

The model will be based on its input parameters. These parameters can roughly be divided into reservoir (RP) and operational parameters (OP). The parameters can be altered to any reasonable number. The table below show all these 'changeable' input parameters.

Table 5-1. A summation of the input parameters, which can change per field or operation, for the physical screening model. the ranking is random. The parameters are specified by the type of parameter, either reservoir or operational, the symbol and the specific function this parameter is having in the model.

Input parameter	Type	Symbol	Function
Permeability	RP	k	Permeability influences among others the diffusivity of a reservoir. See sections 6.6, 7.1 and 8.1.1 for more.
(un)drained Lamé parameter	RP	λ and λ_u	One of the two needed Elastic modulus that controls the resistance of being deformed elastically when a stress is applied on a rock. See section 7.1 for more.
Shear modulus	RP	G (or μ)	The second of the two elastic moduli needed.
Two of the 6 Elastic moduli	RP	E, G, K, λ , ν , M	Young's modulus (E), shear modulus (G or μ), bulk modulus (K), Poisson's ration (ν), Lamé's parameter (λ) and P-wave modulus (M).
Biot-Willis coefficient	RP	α	The Biot-Willis coefficient is a poro-elastic parameter that gives the effective pressure coefficient for the bulk volume of a fluid-saturated rock. Typically between 0-1. See section 6.4 for more.
Injection rate	OP	V_{fi}	The injection rate can be regulated by the operator and creates the injection pressure difference inside the reservoir. The together with the permeability this parameter is the main manipulator of the fluid flow.
Injection Temperature	OP	T_{inj}	The temperature of the water that is re-injected into the reservoir.
Initial reservoir Temperature	RP	T_0	The temperature of the reservoir fluids before operations are started.
Rock density	RP	ρ_r	The density of the rock corresponds to the rock type, like sandstone or limestone.
Reservoir depth	RP	d_{res}	Depth of the top of the reservoir
Fault dimensions	RP	-	The dimensions of the fault, this can either be an rectangular fault (width x length) or a round fault (π x radius)
Fault location	RP	-	The fault location is in meter from the injector.

Other parameters that can be held constant (i.e. set to a default value) are:

Table 5-2. A summation of the input parameters, which can be held constant for every other field or operation, for the physical screening model. The ranking is random. The parameters are specified by the type of parameter, either reservoir or operational, the symbol and the specific function this parameter is having in the model.

Input parameter	Type	Symbol	Function
Fluid density	FP	ρ_{fl}	The density of a substance is its mass per unit volume. This is assumed to be constant at all pressures and temperatures.
Fluid viscosity	FP	η	The viscosity of the injection fluid influences the volumetric flow velocity through the reservoir. See section 8.1.1.
Heat capacity of rock	RP	C_r	The amount of heat has to be added to a given mass of rock to increase a unit of change in its temperature.
Heat capacity of fluid	FP	C_w	The amount of heat has to be added to a given mass of fluid to increase a unit of change in its temperature.
Effective thermal conductivity of the aquifer	RP	λ_{eff}	The rate of heat transfer from a moving fluid to a solid surface.
Volumetric thermal expansion coefficient	RP	β	Material, rock in this case, expands or contracts in all directions by this coefficient when their temperature is changed. See section 6.6.
Internal friction angle	RP	φ	The angle measured between the normal force and resultant force, which is attained when failure just occurs in response to a shearing stress.
Cohesion	RP	C_o	The cohesive strength of a fault, internal resistance to failure.
Hydrostatic pressure gradient	RP	-	The pressure exerted by the column of fluid per meter of true vertical depth.
Lithostatic pressure gradient	RP	-	The pressure exerted by the column of rock per meter of true vertical depth.
Minimal horizontal stress gradient	RP	-	The minimal horizontal stress exerted by the column of rock per meter of true vertical depth.

The output of the screening model is as mentioned before a Mohr circle plot, a maximum M_0 and the PGV. The Mohr circle plot visualizes the stress situation inside the reservoir at a specific location before injection and after injection at a specific time. The location of the Mohr circle inside the reservoir should correspond with the location of a fault. The time passed after the injection should be significant, need at least 300 days, what this means will be discussed in the result (chapter 7). The Mohr circle after the injection lies either (partly) in the unstable zone or completely in the stable zone, figure 6-4 (section 6.2). In case that the Mohr circle does lay in the unstable zone, the maximum Moment magnitude and the PGV should be calculated. These numbers will give an indication of what potentially the maximal moment of seismicity can be and its resulting ground movement (see section 7.4 and 7.5).

The combination of the Mohr circle and the maximum Moment magnitude gives a great indication of the stability of the system. For the SRA only the Mohr circle will indicate whether the fault is stable or unstable and if the Physical screening model fails or not.

QUICK SCAN (SRA STEP 1B)

The remaining parameters that can have an effect on seismicity during geothermal operations are similar to the remaining parameters of the Quick-scan from the Q-con/IF report, see Table 4-3. These parameters are:

- Basement connection
- Inter-well pressure communication
- Epicentral distance to natural earthquakes
- Epicentral distance to induced seismicity
- Net injected fluid

These parameters are considered constant or zero in the Physical Screening Model, SRA Step 1A, due to modelling difficulties or the lesser importance in the Dutch subsurface. Even though these parameters are excluded from the physical model, they could be of significant seismic influence when present or non-zero. For example, when there is natural or induced seismicity in the vicinity, the risk of seismicity will be higher for the geothermal project.

Similar to the Q-con/IF report these factors will be categorised and graded. Table 5-3 shows the grading table. The scores of the five parameters are added up and this total score number is divided by the total possible score, 50. The result is a normalized score between 0 and 1, giving it the symbol Q_s . When this score is below $1/3$, $Q_s < 0.33$, the Quick-Scan is passed, if the score exceeds $1/3$, $Q_s > 0.33$, it is **not** passed.

Table 5-3. The altered Quick-Scan for the new SRA. These five parameters correspond to the crossed parameters in Table 3-3. Similar to the Quick-Scan of the Q-con/IF SRA, The five parameters in this table should be reviewed with scores of 0, 3, 7 or 10, depending on the argument inside the table box.

Score	Basement connection	Inter-well pressure communication	Epicentral distance to natural earthquakes [KM]	Epicentral distance to induced seismicity [KM]	Net injected fluid [1000 m ³]
10	Yes	No	< 1	< 1	> 20
7	Possible	Unlikely	1 – 5	1 – 5	5 – 20
3	Unlikely	Likely	5 – 10	5 – 10	0.1 – 5
0	No	Yes	> 10	> 10	< 0.1

5.3 SRA STEP 2

The result of SRA Step 1 decides whether further investigation is needed. Only when all faults inside the reservoir are considered stable and the Quick-scan results in a number lower than 0.33 no additional analysis needs to be done and only monitoring I is needed. However, when these criteria are not met for SRA Step 1 A or B (or both) further investigation is required.

SPECIFIC HAZARD ANALYSIS (SRA STEP 2A)

This action implies that the analytical model and/or the Quick-scan used are not sufficient in examining the seismic hazard. Similar to step 3 of the Q-con/IF report and the SodM methodology a more detailed and full location specific SRA should be made. This part of the SRA requires considerable more effort, as it will include a reservoir specific flow-and-production model. The reservoir will not be further considered as isotropic and homogeneous but should be more precisely modelled after the well and seismic information obtained during field explorations. The reservoir model can give better details of pressure and temperature diffusion through the reservoir as well as fault dimensions and location. This more thorough and detailed treatment of parameters also requires more uncertainty analysis. In some cases more observation data will have to be assembled in order to create such a model.

When this modelling results in relative low seismic hazard SRA Step 3 Monitoring II will be sufficient. If not, an even more time investing operation will have to be carried out; SRA Step 2B.

RISK ANALYSIS (SRA STEP 2B)

Thus the subsequent step is to evaluate the risk situation of the seismic hazard. With help of the last step in the Physical Screening Model, SRA Step 1A, the ground vibrations of a seismic event can be calculated. With the severity of the ground vibrations a spider risk matrix should be created, similar to step 2 of the SodM approach. Figure 5-2 shows a cause-result relations model of induced seismicity. It shows a schematic representation of the various factors that determine whether induced seismicity can result in a strong earth movement (the influence factors subsurface) and the different factors that influence the magnitude of the possible consequences (the influence factors aboveground). The subsurface influence factors are combined and calculated in the models from SRA Step 1A and SRA Step 2A.

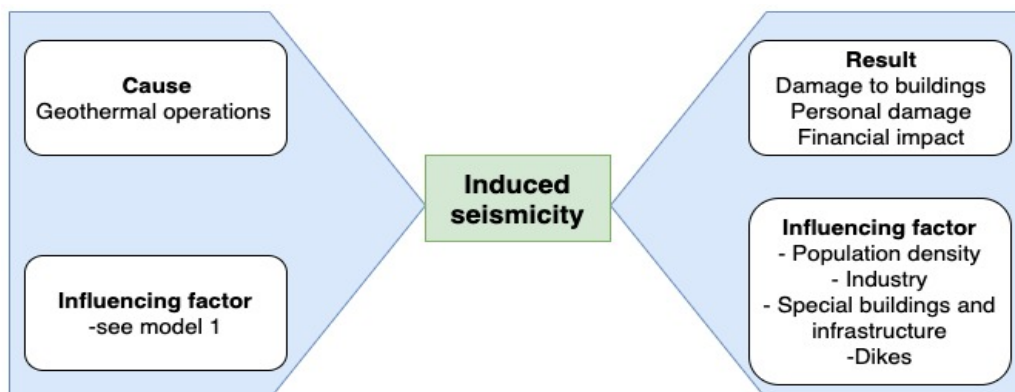


Figure 5-2. Similar to its Q-con/IF version, this is a Schematic representation of the threats and consequences of induced seismicity and the various influencing factors that play a role in that

Analogue to step 2 of the SodM approach, the various factors are analysed quantitatively and ranked based on the outcome per factor. This quantitative analysis should be done according to the same

ranking method as in the SodM method, see Appendix A. The scores of the individual factors are summed, so that a total score is determined for the influencing factors above ground. These scores are normalized with the maximum number of points that can be obtained. The two scores are plotted against each other which qualitatively determines a risk category (Figure 5-3).

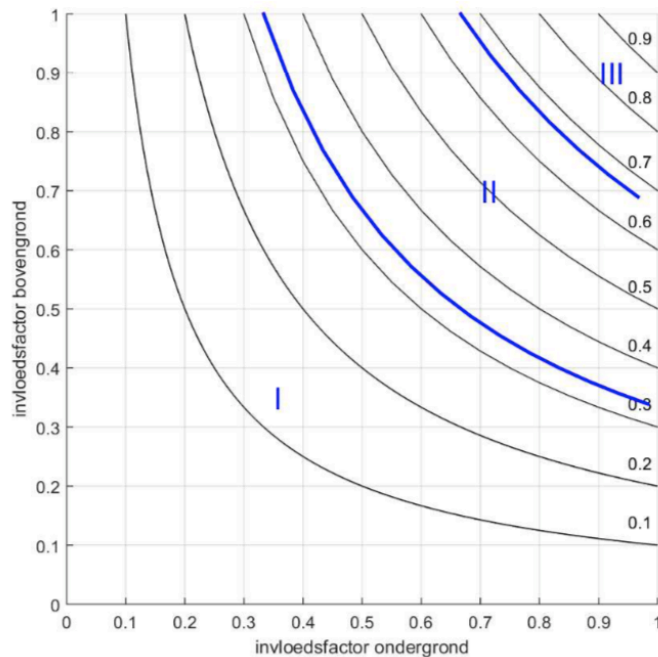


Figure 5-3. The risk matrix similar to the Q-con/IF SRA. The black lines are lines of equal normalized risk. The division into categories is simply done on the basis of 1/3 and 2/3 of this normalized risk.

The location in the risk matrix depends on the combination of the scores for the model, influencing factors subsurface, and the influencing factors aboveground. For fields for which seismic risk due to geothermal operations fall into categories I and II, no further follow-up steps are necessary, only monitoring III. When the risk falls in section III, the plans for the geothermal project should be reconsidered.

5.4 SRA STEP 3

For all the three outcomes in the new SRA, figure 5-1, when operations can be carried out, monitoring is required. However the intensity of this monitoring will differ per outcome. There are three different levels of monitoring and figure 5-1 shows when to use which level. This differentiation in the levels of monitoring corresponds with those of the SodM SRA.

MONITORING I

The first monitoring level is the simplest case. It should be applied when SRA Step 1 results in a stable outcome from the Physical Screening Model with a low number resulting from the Quick-scan. In this case only monitoring with the current geophone and accelerometer network from the KNMI is needed.

MONITORING II

If a Specific Hazard Analysis is preformed, after SRA Step 1 failed, and the result are beneficial still a more through monitoring process is required. This is due to the fact that failing SRA Step 1 implies a

higher risk regardless even though SRA Step 2A proves that there is no immediate seismic hazard. Monitoring of level two includes the following actions:

- Monitoring with a minimal catalogue completeness in the surrounding of the field should be enforced,
- In the surrounding of the field additional placement of accelerometers on geophone locations,
- Implementation of generic seismic-risk management plan.

MONITORING III

In the ultimate case that the Specific Hazard Analysis fails but subsequently the Risk Analysis turns out satisfactory, an even more rigorous monitoring system should be applied. This level three monitoring contains the coming steps:

- Monitoring with a minimal catalogue completeness in the surrounding of the field should be enforced,
- Additional placement of accelerometers on geophone locations,
- Monitoring of vibrations of buildings, especially houses,
- Implementation of a specific seismic-risk management plan on basis of a “Meet- en Regelprotocol”.

6. THEORY BEHIND PHYSICAL SCREENING MODEL

As of this chapter the thesis will continue its development and investigation in the new Physical Screening Model (PSM), which investigates the reactivation of faults inside the geothermal producing reservoir. In order to better understand the complete theoretical background of the reactivation of faults, it is essential to provide a more profound physical background story. This chapter will present more about the important role of stress and pressures, and what the effect of changing these has on the faults inside the producing reservoir.

This theoretical overview will mainly be based on four sources, educational textbooks: Turcotte and Schubert (2002) [66], Engelder (1993) [20], Jaeger et al. (2007) [36] and Guo et al. (2017) [31]. Other references will be mentioned separately.

6.1 STRESS

Stress in the subsurface is a force acting on a solid part of a rock. This causes mechanical resistance in the subsurface and can be divided into three components perpendicular to each other. When transforming these stress vectors into shear stress components and normal stress components, the Cartesian coordinate system is formed, shown in figure 6-1 as X_1 , X_2 and X_3 . This can be explained by showing the following equations:

$$\vec{\sigma} = \lim_{\Delta A \rightarrow 0} \frac{\Delta \vec{F}_0}{\Delta A} \quad [6.1]$$

$$\text{into } \sigma_n = \lim_{\Delta A \rightarrow 0} \frac{\Delta \vec{F}_n}{\Delta A} \quad \text{and} \quad \tau = \lim_{\Delta A \rightarrow 0} \frac{\Delta \vec{F}_s}{\Delta A} \quad [6.2] \ \& \ [6.3]$$

where \vec{F}_0 = surface force [$\text{kg}\cdot\text{m}/\text{s}^2$]

\vec{F}_n = force normal to the surface [$\text{kg}\cdot\text{m}/\text{s}^2$]

\vec{F}_s = force parallel to the surface [$\text{kg}\cdot\text{m}/\text{s}^2$]

A = fault surface [m^2]

τ = shear stress [Pa]

σ_n = normal stress [Pa].

The subsurface can be divided into a three dimensional coordinate system (x , y , z). Combining this with separation of the surface force into a normal stress and a shear stress, the state of stress can be mathematically expressed into 9 components, with each has its own orientation and magnitude. This state of stress can be expressed in the following stress tensor matrix:

$$\sigma_{ij} = \begin{bmatrix} \sigma_{xx} & \sigma_{xy} & \sigma_{xz} \\ \sigma_{yx} & \sigma_{yy} & \sigma_{yz} \\ \sigma_{zx} & \sigma_{zy} & \sigma_{zz} \end{bmatrix} \quad [6.4]$$

In this matrix σ_{xx} , σ_{yy} and σ_{zz} are the normal stresses while σ_{xy} , σ_{xz} , σ_{yx} , σ_{yz} , σ_{zx} and σ_{zy} represent the shear stresses.

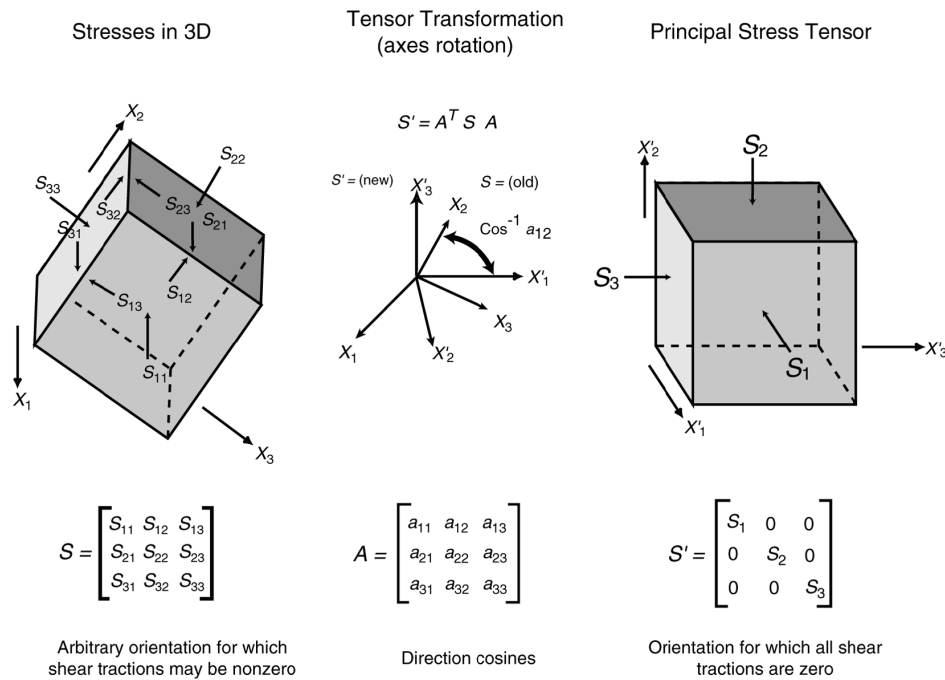


Figure 6-1. Definitions of 1) stress tensors in Cartesian coordinates, 2) tensor transformation through direction cosines, 3) the principle stress axis. It shows the relation between primary stresses and the corresponding normal and shear stresses. Source: GeoMechanics Intl. Inc.

Here one can see that the surface force (\vec{F}_0) is separated into the force normal to the surface (\vec{F}_n) and the force parallel to the component (\vec{F}_s), resulting in the normal stress (σ_n) and shear stress (τ). Figure 6-2 provides a simple relation between these stress components.

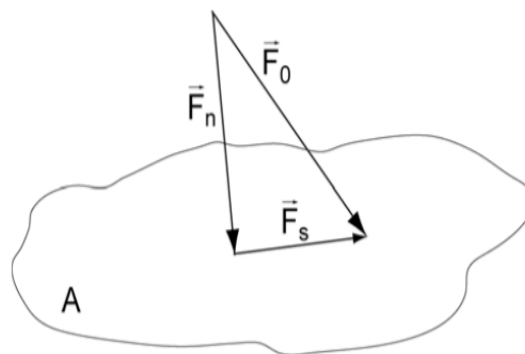


Figure 6-2. Surface force (\vec{F}_0), force normal to the surface (\vec{F}_n) and force parallel to the component (\vec{F}_s) all acting on a surface. Source: Altmann (2010) [4].

PRINCIPAL STRESS

When the principal axis is transformed in such a way that the shear stresses are diminished and the coordinate system is aligned with the three normal stresses, they are called the principal stresses, σ_1 , σ_2 and σ_3 , see figure 6-1(3). When dealing with the subsurface and especially with stresses acting on a (fault) plane these principal stresses are used to describe the general regimes of the system. In the right hierarchy σ_1 symbolizes the maximum stress, while σ_3 corresponds with the lowest principal stress and σ_2 then lies in between those two [11].

When fitting the principle stresses (σ_1 , σ_2 and σ_3) into a geological tectonic stress regimes, they have to be coupled to one of the three stress orientation: σ_v , σ_H and σ_h . These represent the vertical stress,

the maximum horizontal stress and the minimum horizontal stress. These couplings correspond to three different tectonic stress regimes, normal, thrust and strike-slip faulting (see figure 6-3) like Table 6-1 shows.

Table 6-1. The three different faulting regimes and their corresponding stress configuration

Type	Configuration
Normal faulting regime	$\sigma_1 = \sigma_v$, $\sigma_2 = \sigma_H$ and $\sigma_3 = \sigma_h$
Thrust faulting regime	$\sigma_1 = \sigma_H$, $\sigma_2 = \sigma_h$ and $\sigma_3 = \sigma_v$
Strike-slip faulting regime	$\sigma_1 = \sigma_H$, $\sigma_2 = \sigma_v$ and $\sigma_3 = \sigma_h$

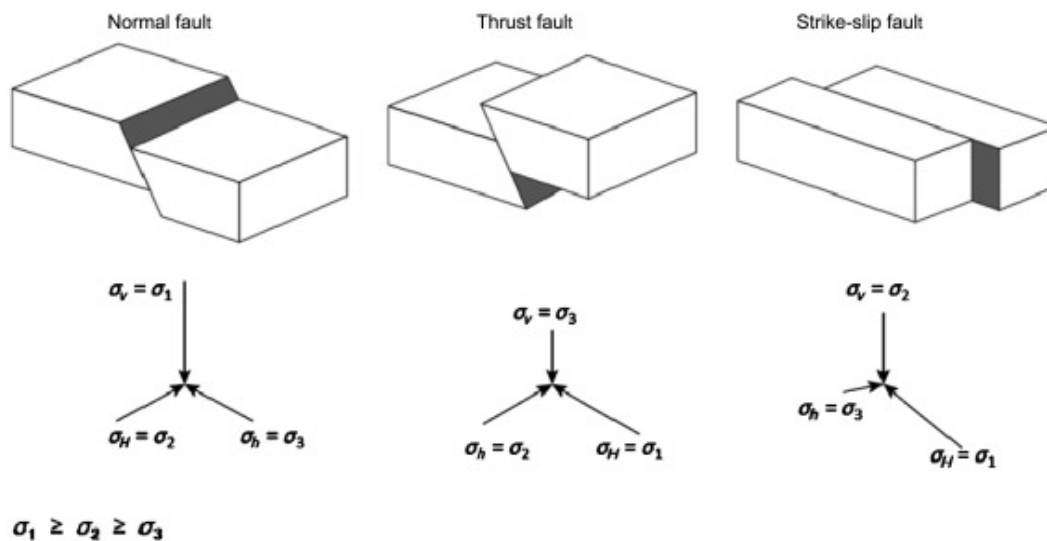


Figure 6-3. Schematic visualisation of the three different faulting regimes and their corresponding stress configuration. Source: Petroleum Production Engineering (Second Edition), 2017 [31].

In general it is assumed that at a certain depth the vertical stress, σ_v , always corresponds to the maximum principal stress, σ_1 , due to the high pressure created by the overlying rock, this stress is also known as the overburden pressure. This means that the other two minor principal stresses are usually found in the horizontal plane. In the Dutch surface there is only little tectonic movement, only in Limburg this can be an issue, and thus most of the stress regimes find the vertical stress to be the σ_1 .

6.2 MOHR CIRCLE

In geotechnical engineering the best fashion to visualize the stress state is by making a Mohr circle of the situation, this is especially important when dealing with fractures and faults. The stress state acting on a rock mass or fault plane is determined by the local tectonic stress field. As described in the previous section, this can either be a normal, thrust or strike-slip regime. The more critical the stress field is, the more likely the rock mass is to fail or fault plane is to reactivate. This failure can potentially lead to seismic activity. How critical, or how big the threshold should be to cause such a failure or reactivation can be visualized by the Mohr circle and calculated by the Mohr-Coulomb failure criterion [11].

A Mohr diagram in general visualizes the relationship between the normal and shear stress acting on planes like faults in a stressed body. It is a tool to quickly see if the stressed planes are in a critical

state and if more extensive research is needed. In a semicircle all possible combinations of shear stress, τ , and normal stress, σ_n , on a fault are described, with a varying angle θ (the angle of the plane with the smallest stress σ_3 , see figure 6-4) between 0 to 90 degrees ($0^\circ \leq \theta \leq 90^\circ$). This is what is called the Mohr circle in a τ - σ_n -diagram. An example of an Mohr circle is given in figure 6-4 and its general equations of are describe by:

$$\sigma_n = \frac{1}{2}(\sigma_1 + \sigma_3) + \frac{1}{2}(\sigma_1 - \sigma_3) \cos\left(\frac{\theta\pi}{180}\right) \quad [6.5]$$

$$\tau = \frac{1}{2}(\sigma_1 - \sigma_3) \sin\left(\frac{\theta\pi}{180}\right) \quad [6.6]$$

where σ_n = normal stress [Pa]

σ_1 = largest principle stress [Pa]

σ_3 = smallest principle stress [Pa]

θ = angle with the fault plane [-]

τ = shear stress [Pa].

These equations describe the arbitrary shear stress τ and normal stress σ_n in a situation with the principal stresses σ_1 and σ_3 acting on an inclined plane, with the angle θ . Figure 6-4 visualizes this situation of stresses acting on a potential fracture or fault.

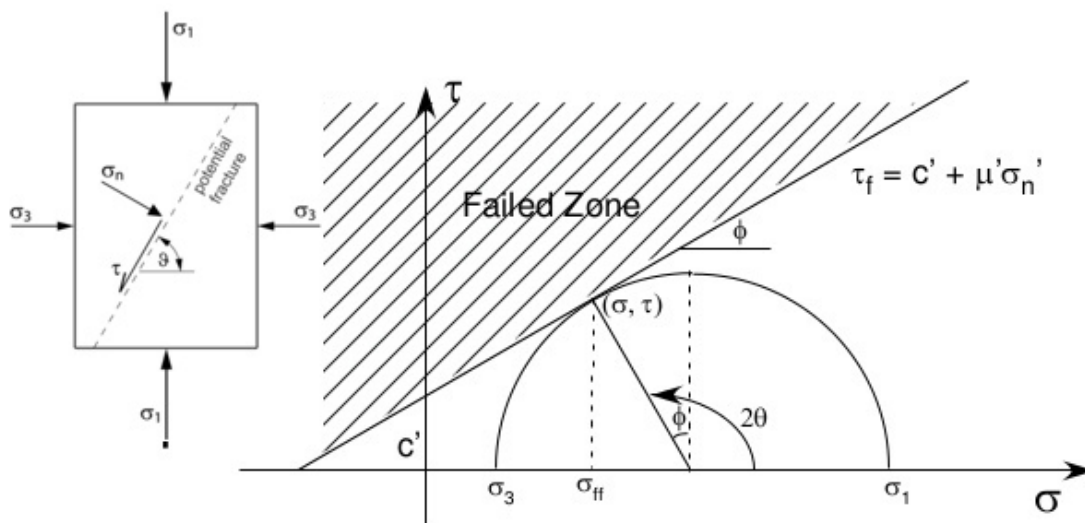


Figure 6-4. Schematic overview of the primary stresses in an angular relation to the normal and shear stress that act on a plane, i.e. potential fault or fracture, combined with the corresponding positions of these stresses in a Mohr plot. In the Mohr circle the difference is made between the unstable zone, the failed zone, and the stable zone. Source: Eisbacher (1996) [19].

MOHR-COULOMB FAILURE CRITERION

The Mohr-Coulomb failure criterion describes the stability of a plane, which can be a fault or fracture. It shows under which shear stress and normal stress the plane is unstable and is likely to fail or slide. It is the most commonly used criterions for compressive stresses. The Mohr-Coulomb failure criterion in this case is defined as a linear envelope with a certain cohesion, C , and angle of internal friction, ϕ , or the friction coefficient, μ .

$$\tau = C + \sigma \tan(\phi) \quad \text{or} \quad \tau = C + \sigma \mu \quad [6.7] \text{ \& \ } [6.8].$$

Eq. 6.5 - 6.8 create a plot containing a Mohr circle and the Mohr-Coulomb failure envelope, like figure 6-4. Failure of the rock mass or fault is assumed when the failure line is tangent to the Mohr circle.

Failure of intact rock only occurs with more stress decrease than failure of faults and fractures. This is because faults and fractures are crosscuts into the subsurface rock and are forming planes of weaknesses. In other words; the weakest part of rock in the subsurface are faults and fractures. This means that the cohesive strength of intact rock is higher than that of faults and thus the corresponding failure envelope of intact rock lies more to the left, see figure 6-5.

FAULT ORIENTATION

The orientation of a fault or a fracture is the angle of the fault plane with respect to the principle stresses in real space. This angle is called θ . In a Mohr diagram, so called Mohr space, this orientation is visualized by the Mohr circle itself. In figure 6-4 it can be seen that the angle between the smallest principle stress, σ_3 , and the fault plane times two corresponds with the angle between the x-axis and the position of the fault on the Mohr circle. Typically a fault is called 'critically orientated' when the angle is 60° in real space and thus 120° in Mohr space. Figure 6-5 shows the difference between critically orientated and poorly orientated faults.

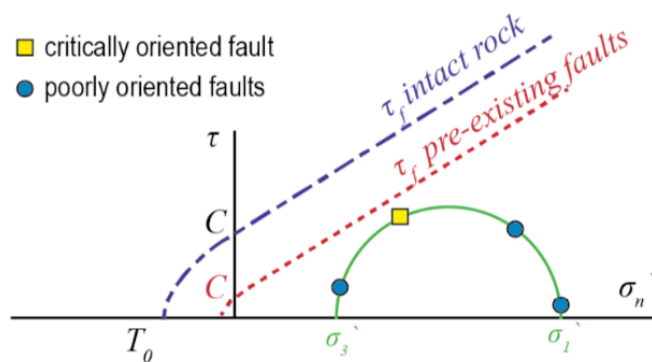


Figure 6-5. The difference between the Mohr coulomb envelope of an intact rock and that of a pre-existing fault. Additionally four of many possible fault orientations are shown on the Mohr circle, with yellow the most critically orientation of a fault is visualized. Source: Buijze et al. (2019) [10]

6.3 PORE PRESSURE

The pressure of a fluid within the pore space of a reservoir is also known as the pore pressure. In general it is assumed that the pore pressure is equal to the weight of the overlying fluid, which means that the total vertical stress in deep reservoirs is equal to the weight of the overlying rock and the overlying fluid. Changing the pore pressure can have disastrous effect on the stress regimes in the subsurface and thus lead to subsurface activities, especially when (active) faults are present.

When including pore pressure into the state of stress, effective stress will be calculated. Effective stress was introduced by Terzaghi (1943) [62] and is simply the difference between the total stress, σ , and the change in pore pressure, P :

$$\sigma_{eff} \text{ or } \sigma' = \sigma - P \quad [6.9]$$

Pore pressure in hydrostatic and thus will be the same in all directions, hence:

$$\sigma_1' = \sigma_1 - P \quad , \quad \sigma_2' = \sigma_2 - P \quad , \quad \sigma_3' = \sigma_3 - P \quad [6.10], [6.11] \text{ \& } [6.12]$$

By increasing the pore pressure ($P < 0$) the effective stress is lowered and a decrease in pore pressure ($P > 0$) means an increase in the effective stress. In geothermal reservoirs fluids are injected: increasing the fluid pressure (to create flow) in a reservoir causes pressure in the connected pore space of rocks to increase (the pore space includes pores, cracks, vicinities of grain contacts, and all other possible voids in rocks). This leads to an increase of pore pressure at the critical locations as well. Such an increase consequently causes a decrease of the effective normal stress, usually acting compressional on arbitrary internal rock surfaces. This leads to sliding along pre-existing, favourably oriented subcritical cracks [56]. This sliding can lead to seismic activity, especially close to the injection well. The effective stress, σ_{eff} , is thus heavily influenced by the pore pressure change.

The influence that the pore pressure on the effective stress presumably has on the Mohr circle is a shift to the left or the right in τ - σ_n -diagram. This means that for an increase of pressure, which corresponds to injection of fluids, the circle moves to the left and comes dangerously closer to the failure envelope. While a decrease of pore pressure, which corresponds to fluid extraction, lets the Mohr circle move to the right, making the rock mass or fault less perceptible for failure. Figures 6-6 and 6-7 show these differences.

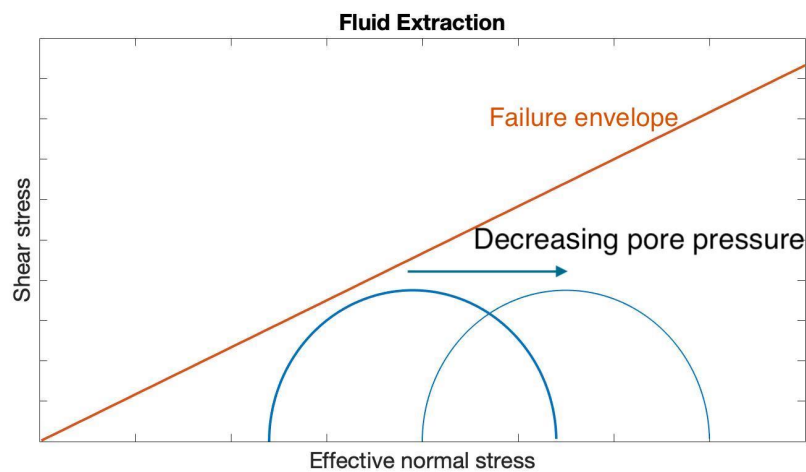


Figure 6-6. Mohr plot indicating the typical movement of the Mohr circle during fluid extraction, when decreasing the pore pressure.

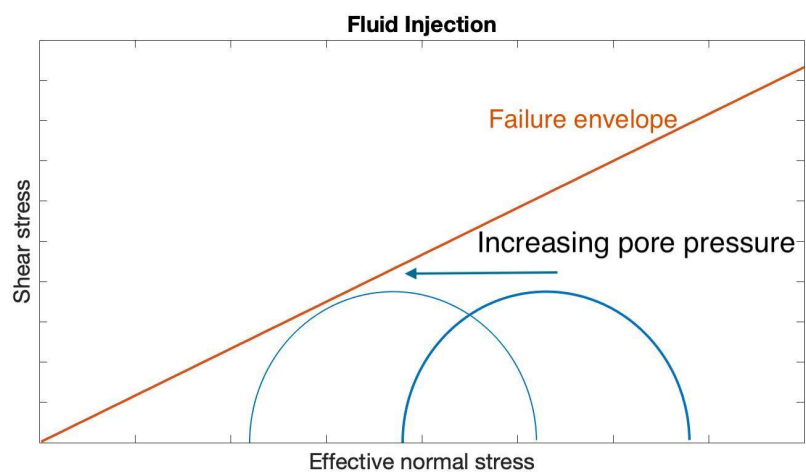


Figure 6-7. Mohr plot indicating the typical movement of the Mohr circle during fluid injection, when increasing the pore pressure.

6.4 PORO-ELASTIC COUPLING

In section 2.2.2 poro-elasticity is already introduced as potentially being a factor in the seismic hazard calculations at geothermal operations. There poro-elasticity is describes as being the physical process of rock deformation as well as fluid flow through deformable pores and more accurately estimates the changes in stress and pore pressure within the subsurface.

The “necessity” of introducing poro-elasticity in the stress and pore pressure equations comes from the observations of seismicity in depleting oil and gas field. While one would expect no seismic activity due to extraction (of oil and gas), because according to the Mohr diagram in figure 6-6 rock should be stabilizing, many examples of seismicity during reservoir depletion are found around the world as well as in the Netherlands [67] [68]. This strongly suggest that the stress and pore pressure are coupled, to be more specific this concerns a σ_h (minimal horizontal stress) pore pressure coupling. According to research the strength of the coupling can be expressed by the ratio of the $\sigma_h/\Delta P$, so in general we can assume that the larger the minimal horizontal stress the stronger the coupling [34].

6.4.1 BIOT-WILLIS COEFFICIENT

The theory of poro-elasticity describes the changes of the minimal horizontal stress, σ_h , depending on these of the pore pressure, P . In determining the poro-elasticity of the rock, the elastic parameters like the Young’s modulus and the Poisson’s ratio are evaluated. In general it is assumed that deformation of rock is entirely elastic. The elastic response of porous rocks to pore pressure changes depends on the stress carried by the framework of grains compared to the stress carried by the pore fluid, which can be described using Biot-Willis coefficient, α [10]. It is essentially the relation between the total stress and the effective stress, and thus the Terzaghi’s effective stress becomes:

$$\sigma' = \sigma - \alpha P \quad [6.13]$$

Terzaghi’s Eq. 6.10, 6.11 and 6.12 are useful and valid for most soils; because soils are soft and their framework is highly compressible, while their partials itself have a very small compressibility. This justifies the use of 1 for the Biot-Willis coefficient. However for solid rock it is a different story. When the Biot-Willis coefficient is between 0 and 1 this means that the pore pressure changes itself creates volumetric changes in the framework/matrix of the rock, leading to a change in stress. A reservoir can have vertical and horizontal contraction (P decrease) or expansion (P increase), depending on the type of operation it undergoes. Under uniaxial strain conditions, it is assumed that the reservoir is horizontally infinite and has no lateral expansion (or contraction), the theory of poro-elasticity produces a space and time independent relationship between the vertical stress, σ_v , minimal horizontal stress, σ_h , and the pore pressure, P :

$$\sigma_h = \frac{v}{1-v} \sigma_v + \alpha \frac{1-2v}{1-v} P \quad [6.14]$$

where v is the Poisson’s ratio and the Biot-Willis coefficient α can be described as:

$$\alpha = 1 - \frac{K_d}{K_g} \quad [6.15]$$

where K is the bulk modulus, and d stands for the drained form, while g stands for grains. Adding another assumption that vertical stress, σ_v , created by the overburden (assuming a normal fault regime), is not changing during injection or production, leads to the following relationship:

$$\Delta\sigma_h = \alpha \frac{1-2v}{1-v} \Delta P \quad [6.16].$$

This formulation proves that an increase of pore pressure decreases the differential stress. Again when considering a normal fault regime, where the vertical stress, σ_v , is created by the overburden, this will result in a smaller size Mohr circle. Decreasing the pore pressure will increase the differential stress and consequently result in a larger size Mohr circle. Figures 6-8 and 6-9 present both situations, note that this shows the case for a normal fault regime. These stress changes are independent of the direct pressure change and are calculated with Eq. 6.16. They only result in the elastic deformation.

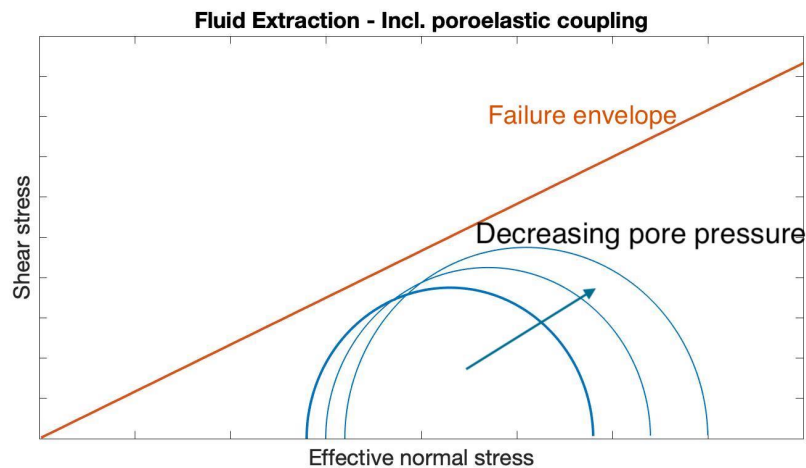


Figure 6-8. Mohr plot indicating the typical movement of the Mohr circle during fluid extraction, when decreasing the pore pressure, including poro-elastic coupling.

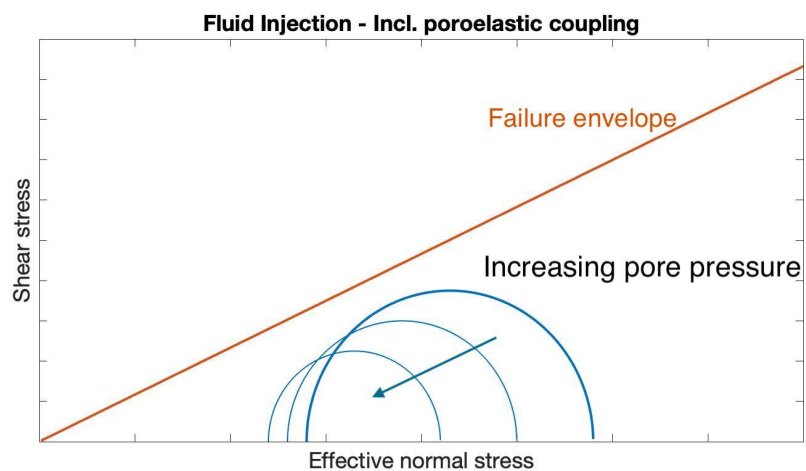


Figure 6-9. Mohr plot indicating the typical movement of the Mohr circle during fluid injection, when increasing the pore pressure, including poro-elastic coupling.

Variation in the Biot-Willis coefficient and Poisson's ratio can strongly influence the ratio of the $\sigma_h/\Delta P$ and thus the coupling strength. Eq. 6.15 on itself shows that α is depending on reservoir parameters and thus can change significantly when producing from different reservoirs.

6.4.2 DIFFERENT FAULT REGIMES

Figures 6-8 and 6-9 illustrate the influence that poro-elastic coupling has on the rock mass and fault stability in a normal fault regime. In a normal fault regime it is assumed that the maximum stress corresponds with the vertical stress while the minimum stress is equal to the minimal horizontal stress, see Table 6-1 in the principal stress section.

NORMAL FAULT REGIMES

In a normal fault regime, as discussed before, σ_v is not affected by pore pressure changes. As figure 6-10 shows an increase of pore pressure can lead to stabilization of the rock, while decrease of stress can destabilize the rock. Poro-elasticity can thus inverse the predictions done when looking at the stabilization result of only the direct pore pressure change. The result of poro-elasticity on the effective stress, Eq. 6.17 and 6.18, is:

$$\sigma'_{v,eff} = \sigma_{v,eff} - \Delta P' \quad \sigma'_{h,eff} = \sigma_{h,eff} + \frac{\Delta\sigma_h}{\Delta P} \Delta P' - \Delta P' \quad [6.17] \text{ \& } [6.18]$$

where $\sigma'_{v,eff}$ = poro-elastic effective vertical stress [Pa]

$\sigma'_{h,eff}$ = poro-elastic effective smallest horizontal stress [Pa].

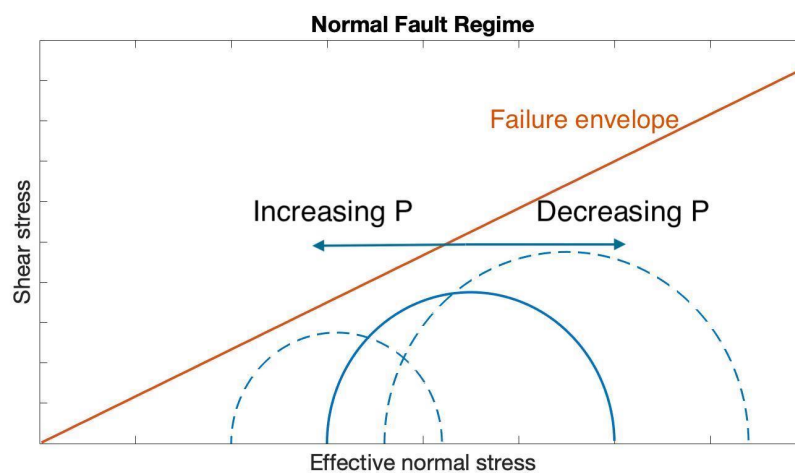


Figure 6-10. Mohr plot indicating the typical movement of the Mohr circle for increasing and decreasing the pore pressure in a normal fault regime.

THRUST FAULT REGIMES

In thrust fault regimes the case is very different. Regarding Table 6-1 the principal stresses in this situation are different. In a normal fault regime the assumption is that the vertical stress is unaffected by poro-elasticity. The same holds for the thrust fault regime but here the vertical stress is not the maximal stress but the minimum stress; $\sigma_{1/\max} = \sigma_H$ and $\sigma_{3/\min} = \sigma_v$. Here due to poroelastic coupling, when decreasing the pore pressure, σ_H is also decreasing. This while σ_v is not affected by the coupling effect. This lead to a Mohr circle that moves to the right (because of direct pore pressure effect) but also becomes smaller, resulting intense stabilisation during depletion.

On the contrary, the maximum stress, σ_H in thrust fault regimes, increases when pore pressure is increase due to injection, and thus enlarging the Mohr circle while it moves to the left (because of the direct pore pressure) moving it closer to the failure envelope. This means that for injection poro-elasticity increasingly destabilizes potential faults lying in the reservoir with a thrust fault regime. Figure 6-11 shows this coupling effect and pore pressure effect on thrust fault regimes.

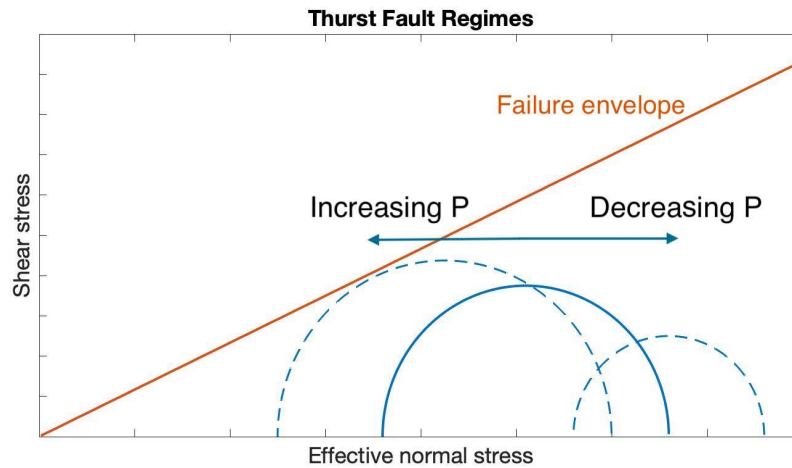


Figure 6-11. Mohr plot indicating the typical movement of the Mohr circle for increasing and decreasing the pore pressure in a thrust fault regime.

Interestingly the difference between the two fault regimes, thrust and normal, is that poro-elasticity effect and direct pore pressure effect superimpose in normal fault regimes, they superpose in thrust fault regimes. Making the effect of poro-elastic coupling contradictory.

STRIKE-SLIP FAULT REGIMES

The final regime describes strike-slip faults, where both the maximum and the minimum stresses are horizontal, $\sigma_{1/\max} = \sigma_H$ and $\sigma_{3/\min} = \sigma_h$. As both stresses are horizontal both are equally influenced by the poro-elastic coupling effect, resulting in a similar plot like figure 6-7. No differential stress is affected and thus the size of the Mohr circle does not change.

That the size of the Mohr circle remains unchanged does not mean that the poro-elastic coupling has no effect on the stabilisation of the fault. The coupling between the pore pressure and the total horizontal stress lets both $\sigma_{1/\max}$ and $\sigma_{3/\min}$ increase as pore pressure is increased (injection), as well as it decreases those stresses when pore pressure is decreased (depletion). Moving the Mohr circle a bit to the right when it just moved to the left (increasing P) and vice-versa.

6.5 DIFFUSION OF PORE PRESSURE AND PORO-ELASTIC STRESS

In the previous two sections the effect of pore pressure increase or decrease on the stress field is explained. In order to investigate this effect in the whole geothermal reservoir it is necessary to calculate to which extent the pore pressure and poro-elastic stresses can reach. Water is injected in to the reservoir with a certain pressure; this pressure is diffused through the reservoir with a particular speed and declining rate. This spatio-temporal evolution can be calculated analytically, done by Rudnicki (1986) [51]. Rudnicki derived the equations needed for spatio-temporal pore pressure and stress change evolution, which included pore pressure stress coupling, for an infinite homogeneous reservoir space.

Starting with Darcy's experiment, where he measured the water flowing through a column of sand, developing Darcy's law of the empirical relationship describing fluid flow through a porous medium:

$$q_z = -k_f \frac{dh}{dz} \quad [6.19]$$

where q_z = fluid flow per unit area and time [m^2/s]

k_f = hydraulic conductivity [m/s]

h = head [m]

z = elevation head [m].

Now replacing the hydraulic conductivity for gravitational acceleration, g , the permeability, k , and the fluid properties like viscosity, η , and fluid density, ρ_f . While also compartmentalize the head into an elevation head, z , and a pressure head, $p/\rho_f g$, the Darcy's law can be written down in a three-dimensional form like

$$\vec{q} = -\frac{k}{\eta} \vec{\nabla} P \quad [6.20]$$

where $\vec{\nabla} P$ = directional pressure difference [Pa].

Including an external source, Q , which represents the injection in this case, a continuity equation can be combined with Eq. 6.20. This is under the assumption that k and h are constant over the whole reservoir space. Resulting in the following partial differential equation:

$$\frac{\partial \zeta}{\partial t} - \frac{k}{\eta} \vec{\nabla}^2 P = Q \quad [6.21].$$

Where ζ is the dimensionless variable that expresses the fluid volume transported out or into a storage and t is the time. This dimensionless variable includes the increment (or decrease) of the mean stress, σ ($=(\sigma_1 + \sigma_2 + \sigma_3)/3$), and pore pressure and the stress pore pressure coupling, it can be expressed as (see Appendix B for its construction)

$$\zeta = \frac{\alpha}{K_d} \sigma + \frac{\alpha}{K_{dB}} P \quad [6.22]$$

where α = Biot-Willis coefficient [-]

K_d = drained bulk modulus [Pa]

B = Skempton's coefficient which is defined by defined as ratio of pore pressure change due to a change in applied stress under undrained conditions [-].

Substituting the Eq. 6.22 into Eq. 6.21 leads to an inhomogeneous diffusion equation for the pore pressure

$$\frac{\alpha}{K_{dB}} \left[\frac{B}{3} \frac{\partial \sigma_{xx}}{\partial t} + \frac{\partial P}{\partial t} \right] - \frac{k}{\eta} \vec{\nabla}^2 P = Q. \quad [6.23]$$

When Eq. 6.22 is solved for the mean stress, σ , and substituted into Eq. 6.23, a diffusion equation for the increment of fluid content, ζ , is found

$$\nabla^2 [\sigma_{xx} + 4\psi P] = -\frac{1+\nu}{1-\nu} \vec{\nabla} \cdot \vec{F} \quad [6.24]$$

where $\psi = \frac{1-2\nu}{2(1-\nu)} \alpha$, poro-elastic stress coefficient derived from Eq. 6.14 [-]

F = body force [kg·m/s²]

ν = Poisson's ratio [-].

Arriving to the diffusion equation for ζ

$$\frac{\partial \zeta}{\partial t} = \frac{k}{\eta S} \nabla^2 \zeta + Q + \frac{k}{\eta} \frac{\lambda_u - \lambda}{\alpha(\lambda_u + 2G)} F_{k,k} \quad [6.25]$$

where S = uniaxial specific storage [m^3]

$F_{k,k}$ = body force [$kg \cdot m/s^2$]

λ = lame parameters (and λ_u = undrained lame parameter) [Pa]

G = shear modulus [Pa].

Eventually Rudnicki solved the diffusion Eq. 6.25 for an infinite homogeneous poro-elastic medium in a case where fluid injection is continuous at one injection point. Also introducing the spatio-temporal pore pressure and stress changes the equation can be written as

$$\Delta P(x, t) = \frac{\Phi}{\rho_{fc}} \frac{1}{4\pi r} \left[\frac{(\lambda_u - \lambda)(\lambda + 2G)}{\alpha^2(\lambda_u + 2G)} \right] \operatorname{erfc} \left(\frac{1}{2} \xi \right) = \frac{q}{\rho_{fc}} \frac{1}{4\pi r} \frac{\eta}{k} \operatorname{erfc} \left(\frac{1}{2} \xi \right) \quad [6.26]$$

$$\Delta \sigma_{ij}(x, t) = -\frac{\Phi}{\rho_{fc}} \frac{(\lambda_u - \lambda)G}{4\pi r \alpha(\lambda_u + 2G)} \left\{ \delta_{ij} \left[\operatorname{erfc} \left(\frac{1}{2} \xi \right) - \frac{2}{\xi^2} g(\xi) \right] + \frac{x_i x_j}{r^2} \left[\operatorname{erfc} \left(\frac{1}{2} \xi \right) + \frac{6}{\xi^2} g(\xi) \right] \right\} \quad [6.27]$$

where $\xi = \frac{x}{\sqrt{ct}}$

t = injection time [s]

x = distance from the injector [m]

Φ = fluid mass density [kg/m^3]

ρ_f = fluid density [kg/m^3]

$c = \frac{\kappa(\lambda_u - \lambda)(\lambda + 2\mu)}{\alpha^2(\lambda_u + 2\mu)}$, where: $\left(\kappa = \frac{k}{\eta} \right)$ = diffusivity [m/s]

λ = Lamé parameter (and λ_u = undrained lame parameter) [Pa]

G = shear modulus [Pa]

α = Biot-Willis coefficient = $1 - \frac{K}{K_g}$ [-]

k = permeability [m^2]

η = viscosity [Pa.s]

with $g(\xi)$ being:

$$g(\xi) = \frac{1}{2\sqrt{\pi}} \int_0^\xi s^2 \exp\left(-\frac{1}{4}s^2\right) ds = \operatorname{erf}\left(\frac{1}{2}\xi\right) - \frac{1}{\sqrt{\pi}} \xi \exp\left(-\frac{1}{4}\xi^2\right) \quad [6.28].$$

It is assumed that the system is isotropic and homogeneous, meaning there is radial symmetry and only the radial and tangential stress components are considered. The radial stress is considered to be the coupling between the pore pressure, P , and the normal stress, σ_{ii} , along the i -axis of the Cartesian coordinate system, which has the injection point as origin. See figure 6-12. For the radial stress, σ_{rad} , holds that for σ_{ij} $i = j$.

The tangential stress, σ_{tan} , is the normal stress component, σ_{ij} , which is observed along the j-axis. For this stress holds that for $\sigma_{ij} \ i \neq j$. The radial and tangential stresses relate differently to stress regimes during injection and are dependent on the type of stress regime.

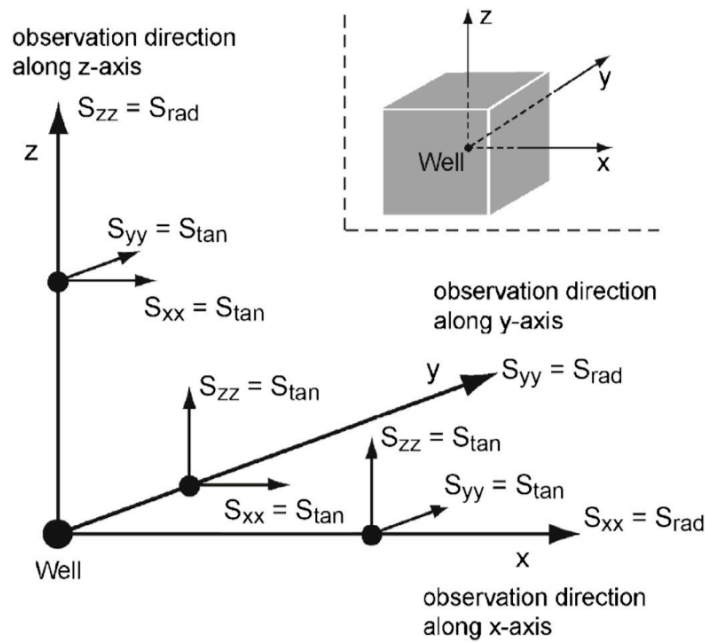


Figure 6-12. Schematic visualisation of the different stress components with respect to the injection point and co-ordinate axes. Source: Altmann (2014) [5].

This leads to the differentiation of Eq. 6.27 into two equations for the stress difference calculation used in my model, first for radial stress:

$$\Delta\sigma_{rad}(x, t) = -\frac{\Phi}{\rho_{fc}} \frac{(\lambda_u - \lambda)G}{4\pi r \alpha (\lambda_u + 2G)} \left[2 * \operatorname{erfc}\left(\frac{1}{2}\xi\right) + \frac{4}{\xi^2} g(\xi) \right] \quad [6.29]$$

and for tangential stress:

$$\Delta\sigma_{tan}(x, t) = -\frac{\Phi}{\rho_{fc}} \frac{(\lambda_u - \lambda)G}{4\pi r \alpha (\lambda_u + 2G)} \left[\operatorname{erfc}\left(\frac{1}{2}\xi\right) - \frac{2}{\xi^2} g(\xi) \right] \quad [6.30].$$

From the injection point the distribution of pore pressure disturbance spreads isotropic through the homogeneous reservoir. The injection is constant and will eventually result in an infinite distribution through the infinite reservoir. As the coupling of poro-elasticity is taken into account, the stress in the system will be influenced directly by the pore pressure difference. The difference in pore pressure (ΔP) and poro-elastic stress ($\Delta\sigma_{poro}$) will lead to changes in the total stress state that can reactivate faults.

6.4.3 OBSERVATION POINT

As figure 6-12 indicated, the location of the observation point (i.e. a potential fault) relative to the injection point matters when looking at the orientation of the radial and tangential stress. When investigating an observation point (i.e. fault) lying along the x-direction the orientation of σ_{tan} and σ_{rad} is different when it is lying in the z-direction regarding the local primary stresses, σ_1 , σ_2 and σ_3 . This implies that the calculations of the effective primary stresses are different in the three primary directions. Combining this directional dependent stress calculations with the three different fault regimes, combining figure 6-12 with figure 6-13, many different local primary stresses can be

calculated, which done below. As a Mohr circle is constructed by the maximal and minimal stress, it should be evaluated in both the maximal, σ_1 , direction and the minimal direction, σ_3 .

Regime	Relative stress magnitudes	Differential stress $\sigma_1 - \sigma_3$
NF: Normal Faulting regime	$S_v > S_H > S_h$	$S_v - S_h$
SS: Strike Slip Faulting regime	$S_H > S_v > S_h$	$S_H - S_h$
TF: Thrust Faulting regime	$S_H > S_h > S_v$	$S_H - S_v$

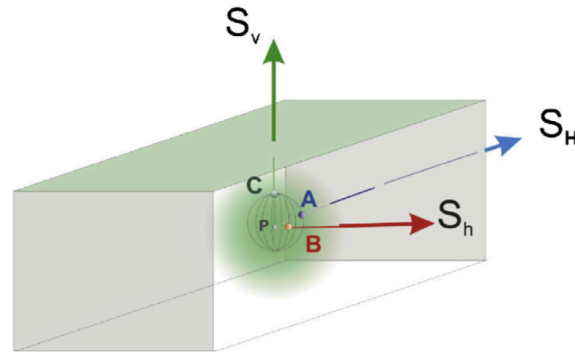


Figure 6-13. Schematic visualisation of the different stress components with respect to the injection point and the local stress regimes. The combination with figure 6-12 will provide 9 different principal stress calculations. Source: Altmann (2014) [5].

NORMAL FAULT REGIME

(MAXIMAL) VERTICAL DIRECTION

It subsequently follows that in a normal fault regime the primary stresses can be solved like this:

$$\sigma_1 = \sigma_{V,eff} = \sigma_V - \Delta P(x, t) \quad (\text{without coupling}) \quad [6.31]$$

$$\sigma_3 = \sigma_{h,eff} = \sigma_h - \Delta P(x, t) \quad (\text{without coupling}) \quad [6.32].$$

Now the coupling between the pore pressure and the stress comes involved, as described earlier. As the observation point is located on the σ_V axis, the σ_V is seen as a radial stress (see figure 6.12) and alterations are calculated by Eq. 6.33. This means that the σ_h is observed as the tangential stress and should be altered with Eq. 6.34.

$$\sigma_1 = \sigma_{V,eff} = \sigma_V - \Delta P(x, t) + \Delta\sigma_{rad}(x, t) \quad (\text{with coupling}) \quad [6.33]$$

$$\sigma_3 = \sigma_{h,eff} = \sigma_h - \Delta P(x, t) + \Delta\sigma_{tan}(x, t) \quad (\text{with coupling}) \quad [6.34].$$

When also including the temperature in the story (see the next section 6.6), the equations differ from each other. Because the temperature only has influence on the tangential/horizontal area of the reservoir it only decreases the pressure on the two smallest principle stress, σ_2 and σ_3 (in case of a normal faulting regime):

$$\sigma_1 = \sigma_{V,eff} = \sigma_V - \Delta P(x, t) + \Delta\sigma_{rad}(x, t) \quad (\text{with coupling and T}) \quad [6.35]$$

$$\sigma_3 = \sigma_{h,eff} = \sigma_h - \Delta P(x, t) + \Delta\sigma_{tan}(x, t) - \sigma_T(x, t) \quad (\text{with coupling and T}) \quad [6.36].$$

(MINIMAL) HORIZONTAL DIRECTION

The construction of the primary stresses are the same, only now the whole system is turned 45 degrees resulting in the substitution of the radial and tangential stresses. The possible fault, observations point, now lies in the horizontal direction of the injection well.

For a normal fault regime now the σ_h is radial and σ_v is tangential:

$$\sigma_1 = \sigma_{V,eff} = \sigma_V - \Delta P(x, t) + \Delta\sigma_{tan}(x, t) \quad (\text{with coupling and T}) \quad [6.37]$$

$$\sigma_3 = \sigma_{h,eff} = \sigma_h - \Delta P(x, t) + \Delta\sigma_{rad}(x, t) - \sigma_T(x, t) \quad (\text{with coupling and T}) \quad [6.38].$$

An important note here it that further down in section 7.3 the PSM will use slightly different equations because of the lateral extensive character of the reservoir as this means that there is no vertical stress change.

TRUST FAULT REGIME

(MAXIMAL) HORIZONTAL DIRECTION

For thrust fault regimes the situation is slightly different as $\sigma_1 \neq \sigma_v$ as in the normal fault regime but $\sigma_1 = \sigma_H$ and $\sigma_3 \neq \sigma_h$ but $\sigma_3 = \sigma_v$. This results in the following calculations of the primary stresses:

$$\sigma_1 = \sigma_{H,eff} = \sigma_H - \Delta P(x, t) \quad (\text{without coupling}) \quad [6.39]$$

$$\sigma_3 = \sigma_{V,eff} = \sigma_V - \Delta P(x, t) \quad (\text{without coupling}) \quad [6.40].$$

Here the observation point is along the σ_H axis. This means that σ_v represents a tangential stress while σ_H a radial stress describes. For the temperature holds that it only influences the horizontal area. As in a thrust fault regime the σ_1 is the maximum horizontal stress and σ_3 is vertical, the temperature component only has influence on σ_1 . For thrust fault regimes Eq. 6.39 and 6.40 are changed into:

$$\sigma_1 = \sigma_{H,eff} = \sigma_H - \Delta P(x, t) + \Delta\sigma_{rad}(x, t) - \sigma_T(x, t) \quad (\text{with coupling and T}) \quad [6.41]$$

$$\sigma_3 = \sigma_{V,eff} = \sigma_V - \Delta P(x, t) + \Delta\sigma_{tan}(x, t) \quad (\text{with coupling and T}) \quad [6.42].$$

(MINIMAL) VERTICAL DIRECTION

Just like with the normal fault regime for a thrust fault regime the σ_{poro} are also inverted when changing the direction from horizontal to vertical:

$$\sigma_1 = \sigma_{H,eff} = \sigma_H - \Delta P(x, t) + \Delta\sigma_{tan}(x, t) - \sigma_T(x, t) \quad (\text{with coupling and T}) \quad [6.43]$$

$$\sigma_3 = \sigma_{V,eff} = \sigma_V - \Delta P(x, t) + \Delta\sigma_{rad}(x, t) \quad (\text{with coupling and T}) \quad [6.44].$$

STRIKE SLIP REGIME

(MAXIMAL) HORIZONTAL DIRECTION

In strike slip regimes the principal stresses are classified like this: $\sigma_1 = \sigma_H$, $\sigma_2 = \sigma_v$ and $\sigma_3 = \sigma_h$. This implies that both the maximal and the minimal stresses extend along the horizontal axis. Here the primary stresses are determined as follows:

$$\sigma_1 = \sigma_{H,eff} = \sigma_H - \Delta P(x, t) \quad (\text{without coupling}) \quad [6.45]$$

$$\sigma_3 = \sigma_{h,eff} = \sigma_h - \Delta P(x, t) \quad (\text{without coupling}) \quad [6.46].$$

In agreement with the other regimes, σ_v axis is considered to be the observation point. The maximal horizontal stress, σ_H , is a radial stress and the minimal stress, σ_h , is a tangential stress. This peculiar situation suggests that both the σ_1 and σ_3 , which are on the horizontal plane together, will be

affected by the stress alteration due to the temperature change. This creates the following equations for the primary stresses:

$$\sigma_1 = \sigma_{H,eff} = \sigma_H - \Delta P(x, t) + \Delta\sigma_{rad}(x, t) - \sigma_T(x, t) \quad (\text{with coupling and T}) \quad [6.47]$$

$$\sigma_3 = \sigma_{h,eff} = \sigma_h - \Delta P(x, t) + \Delta\sigma_{tan}(x, t) - \sigma_T(x, t) \quad (\text{with coupling and T}) \quad [6.48].$$

(MINIMAL) HORIZONTAL DIRECTION

For a strike slip fault regime the minimal stress direction is also horizontal, leading to the following primary stress calculations:

$$\sigma_1 = \sigma_{H,eff} = \sigma_H - \Delta P(x, t) + \Delta\sigma_{tan}(x, t) - \sigma_T(x, t) \quad (\text{with coupling and T}) \quad [6.49]$$

$$\sigma_3 = \sigma_{h,eff} = \sigma_h - \Delta P(x, t) + \Delta\sigma_{rad}(x, t) - \sigma_T(x, t) \quad (\text{with coupling and T}) \quad [6.50].$$

6.6 THERMOELASTIC STRESSING

Production from a geothermal reservoir at saturated conditions (in an aquifer) not only results in a pressure difference but also in a temperature decline as heat is extracted as hot water from the production well, and cold water is re-injected via the injector well. As discussed in section 2.2.2, thermoelastic stressing describes the shrinking and expansion of rocks in a reservoir due to cooling or heating. This activity leads to a reduction or an increase of normal stress and shear stress. In general, the order of magnitude of the thermoelastic stress changes is assumed to be similar to the pressure related stress change. In low enthalpy geothermal doublets the difference between the temperature of the injected water and the reservoir water is generally about 30°C -70°C and the diffusion of this temperature difference takes a lot more time compared to the pore pressure diffusion, but the thermal stress changes in the vicinity of the injection well can be significant [39].

TEMPERATURE TO STRESS

The conversion from temperature change to the relative magnitude of stress change in a geothermal system needs to be quantified. According to Jaeger et al. [36] the basic assumption of linear thermal elasticity is that if the rock is subjected to both temperature change and stress change, the strain in this case is the sum of the thermal strain and the stress induced strain, which is:

$$\varepsilon = \frac{1}{2G}\tau - \frac{\nu}{2G(1+\nu)}trance(\sigma)I - \alpha_t(T - T_0)I \quad [6.51]$$

where ε = total strain [-]

G = shear modulus [Pa]

σ = stress [Pa]

ν = Poisson's ratio [-]

α_t = linear thermal expansion coefficient [-]

I = identity matrix as here considered to be a three directional situation [-]

$T - T_0 = \Delta T$ = temperature difference [°C].

Simplifying and converting this equation into terms of strains it is found to be like this:

$$\sigma = 2G\varepsilon - \lambda \text{trance}(\varepsilon)I - 3\alpha_t K \Delta T I \quad [6.52]$$

which can be written explicitly as

$$\Delta\sigma_{xx} = 2G\varepsilon_{xx} - \lambda(\varepsilon_{xx} + \varepsilon_{yy} + \varepsilon_{zz}) - 3\alpha_t K \Delta T \quad [6.53]$$

$$\Delta\sigma_{yy} = 2G\varepsilon_{yy} - \lambda(\varepsilon_{xx} + \varepsilon_{yy} + \varepsilon_{zz}) - 3\alpha_t K \Delta T \quad [6.54]$$

$$\Delta\sigma_{zz} = 2G\varepsilon_{zz} - \lambda(\varepsilon_{xx} + \varepsilon_{yy} + \varepsilon_{zz}) - 3\alpha_t K \Delta T \quad [6.55]$$

$$\Delta\sigma_{xy} = 2G\varepsilon_{xy}, \quad \Delta\sigma_{xz} = 2G\varepsilon_{xz}, \quad \Delta\sigma_{yz} = 2G\varepsilon_{yz} \quad [6.56], [6.57] \text{ \& } [6.58].$$

As the poro-elastic stress part is already discussed in the sections above, the interesting part of these equations is the last terms on the right hand side of Eq. 6.53, 6.54 and 6.55. This is often referred as the thermal stress. This means that in the case of laterally constrained rocks, i.e. in a lateral extensive reservoir, the thermal stress can be found using this equation:

$$\Delta\sigma_T = \frac{\alpha_t E \Delta T}{(1-\nu)} \quad (\text{TNO Buijze, 2019}) \quad [6.59]$$

where $\Delta\sigma_T$ = thermal stress change [Pa]

E = Young's modulus [Pa].

Thus, according to Eq. 6.59 a decrease in temperature leads to a decrease in thermal stress. As the assumption is that the reservoir is laterally extensive and that vertical stress, σ_v , created by the overburden (assuming a normal fault regime), is not changing during injection or production, the Mohr circle will change in size. Due to the decrease in temperature at a specific time and location the rock in the reservoir will contract and the horizontal stress will decrease. In a normal stress regime this will result in a growth of the Mohr circle, destabilizing the rock mass or fault. Figure 6-14 shows that case.

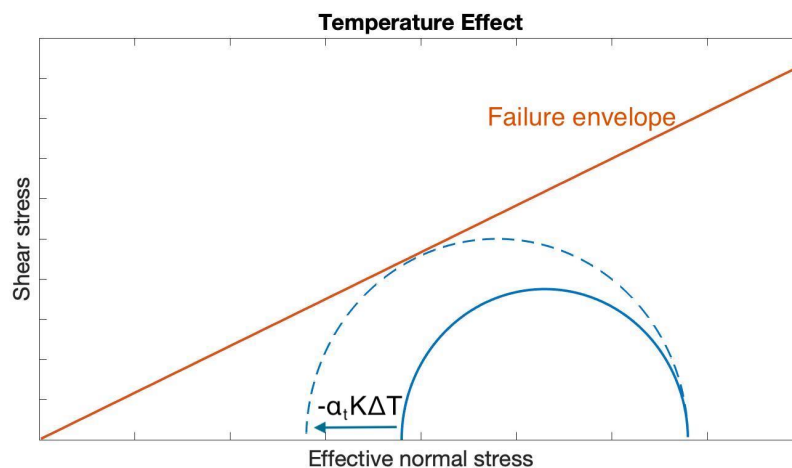


Figure 6-14. Mohr plot indicating the typical movement of the Mohr circle for decreasing the reservoir temperature.

TEMPERATURE DIFFUSION

Similar to previous section, 6.5, diffusion of the pressure difference, in this case the temperature difference, can eventually give an indication of what the stress decrease or increase result can be at a certain time and location. This is important when critically stressed fault lies inside the produced

reservoir. The diffusion of temperature is of a different timeline then that of the pore pressure. While the pore pressure and stress transfer move rapidly through a reservoir, as it is controlled by hydraulic diffusivity, pressure diffusional waves, the diffusion of temperature is controlled by the advancement of the thermal front that is calculated by a transient temperature distribution following Darcy's law of flow.

Using the Laplace transformation technique it is possible to solve the one dimensional heat transportations equation in porous media. This can be described by transient temperature distribution. Like the pore pressure diffusion we assume the reservoir to be homogeneous. Variation of fluids and rock properties over time and space are neglected. Prior to the injection of cold water into the geothermal reservoir the whole system is assumed to have a uniform initial temperature. This leaves the governing differential equation for the heat transport in porous medium with advective and conductive heat transport derived using the energy balance principle, from Ganguly and Kumar (2014) [24]:

$$\frac{\partial}{\partial t} [(1 - \phi)\rho_r C_r T(x, t) + \phi\rho_w C_w T(x, t)] + \frac{\partial}{\partial x} [u_w \rho_w C_w T(x, t)] = \frac{\partial}{\partial x} \left[\lambda_{c,eff} \frac{\partial T(x, t)}{\partial x} \right] \quad [6.60]$$

where ρ_r & ρ_w = density of the rock and water [kg/m³]

C_r & C_w = heat capacity of the rock and water [J/kg·°C]

ϕ = porosity [-]

u_w = flow velocity of water [m/s]

t = injection time [s]

x = longitudinal direction [m]

$\lambda_{c,eff}$ = effective thermal conductivity of the porous medium [W/m·°C].

Transforming the Eq. 6.60 using partially differential equation and setting the boundary conditions a general analytical solution can be found. The governing equation for a homogeneous reservoir is a constant coefficient thus Eq. 6.60 can be written as

$$K_1 \frac{\partial T(x, t)}{\partial t} + K_2 \frac{\partial T(x, t)}{\partial x} = \lambda_c \frac{\partial^2 T(x, t)}{\partial x^2} \quad [6.61]$$

where $K_1 = (1 - \phi)\rho_r C_r + \phi\rho_w C_w$

$K_2 = \rho_w C_w u_w$

λ_c = thermal conductivity of the porous medium [W/m·°C].

Using the Laplace transformation of Eq. 6.61 and setting the initial conditions as

$$T(Z, t) = T_0, \quad Z \geq 0, t = 0 \quad [6.62]$$

creates

$$\lambda_c \frac{d^2 \bar{T}}{dx^2} - K_2 \frac{d\bar{T}}{dx} - K_1 s \bar{T} + K_1 T_0 = 0 \quad [6.63].$$

This leads to the general equation for Eq. 6.60 as

$$\bar{T} = c_6 \exp \left[\frac{K_2 x}{2\lambda_c} \left\{ 1 + \left(1 + \frac{4K_1 \lambda_c}{K_2^2} s \right)^{\frac{1}{2}} \right\} \right] + c_7 \exp \left[\frac{K_2 x}{2\lambda_c} \left\{ 1 - \left(1 + \frac{4K_1 \lambda_c}{K_2^2} s \right)^{\frac{1}{2}} \right\} \right] + \frac{T_0}{s} \quad [6.64].$$

Thus we arrive at the particular solution:

$$\bar{T} = \frac{T_0}{s} - \frac{(T_0 - T_{in})}{s} \exp \left[\frac{K_2 x}{2\lambda_c} \left\{ 1 - \left(1 + \frac{4K_1 \lambda_c}{K_2^2} s \right)^{\frac{1}{2}} \right\} \right] \quad [6.65].$$

This is then inverted, transformed with the inverse Laplace equation and again intergraded (see Appendix C for the steps) so it can be written as

$$T(x, t) = T_0 - \frac{2}{\pi^{\frac{1}{2}}} (T_0 - T_{in}) \exp \left(\frac{K_2 x}{2\lambda_c} \right) \int_L^\infty \exp \left(-\zeta^2 - \frac{K_2^2 x^2}{16\lambda_c^2 \zeta^2} \right) d\zeta \quad [6.66]$$

$$\text{where: } L = \frac{x}{2} \left(\frac{K_1}{\lambda t} \right)^{0.5}$$

T_0 = initial temperature [°C]

T_{in} = injection temperature [°C].

6.7 MOMENT

There is more research needed than only a Mohr circle in order to predict anything about the magnitude of a seismic event. There are different ways of expressing the strength of an earthquake. The most publicly known is Richter's magnitude scale; it was the first method that actually measured the energy release of a seismic event. The name is later revised to Local magnitude scale, M_L . Most seismological authorities currently use an improved method, the moment magnitude scale, M_W . This moment magnitude is more precise; more directly related to the energy release of an earthquake and does not underestimate the earthquakes. It is directly related to what physically occurs with the energy release of an earthquake by the seismic moment, M_0 .

SEISMIC MOMENT

Seismic moment is one of the most important source parameters in seismicity calculations. It is measured in "Newton meters" and is the "work" done by the earthquake; it forms the basis for the more important scale, the moment magnitude. The general form in which the seismic moment can be expressed created by Madariaga (1979) [41] is:

$$M_0 = \mu_r \int_S dA D(x, y) = \mu_r \bar{D} A \quad [6.67]$$

where M_0 = seismic moment [Nm]

μ_r = rigidity [-]

D = offset of the fault [m]

A = total area of the fault [m²]

\bar{D} = total slip of the fault [m].

From this equation it is shown that M_0 is a scalar. The assumption is also made that there is only one fault plane. The onset of slip depends on the change of the Coulomb failure function, ΔCFF , in relation to the in situ stresses [35]:

$$\Delta CFF = \Delta\tau - \mu\Delta\sigma_n \quad [6.68].$$

Note that in this case μ represents again the faults friction coefficient. Compressive stresses result in a positive number; in the Mohr circle this will show as a crossing of the Mohr-coulomb envelope and indicates instability. In order to use Eq. 6.67 the amount of total slip of the fault needs to be known, this happens when ΔCFF exceeds the yield surface. Various methods have been created over the years to determine the area of slip and displacement of a fault surface. Madariaga (1979) [41], Van Wees (2018) [71] and Stein (2006) [60] provide analytical approaches to approximate the seismic moment density from the elastic stress solution. In an elastic solution ΔCFF results in an average excess Coulomb stress, $\Delta\sigma$, relative to the Mohr–Coulomb failure criterion over the rupture length, l . The seismic moment density, M_{0M} , of the fault per unit length in strike becomes (Van Wees, 2017) [71]:

$$M_{0M} = \Delta\sigma \frac{l^2}{\sqrt{\pi}} \quad [6.69].$$

Considering this is the density of the seismic moment that needs to cover the whole fault in order to find the result of the complete seismic moment and later the moment magnitude of an event. Assuming slip starts over one rupture length and moves with a certain slip velocity. In iterative models a fault area is divided into patches, when one patch begins to slip it activates surrounding patches by transferring the stress. The amount of stress converted to other patches differs per model, eventually resulting in a discontinuation of slip when the transferred stress is not sufficient to initiate slip in that particular patch. For simplicity, now assuming that once the stress drop initiates the slip it moves instantly over a simple smooth fault on which the stress drop is uniform, erasing the iterative process of moving parts a fault normally has. The fault is considered straight, simple, and has no branches. The only internal friction it has corresponds to the friction coefficient found in Eq. 6.8. This will lead to an overestimation of the seismic moment, but will give a decent indication of its maximum strength. Resulting in the alteration of Eq. 6.67 for a simple circular fault with area A and radius R the following form (Madariaga, 1979) [41]:

$$M_o = \frac{16}{7\pi} R\Delta\sigma A \quad [6.70].$$

While for a rectangular fault with height w and length L it will look like this (stein, 2006) [60]

$$M_o = \frac{3\pi}{8} \Delta\sigma(w^2L) \quad [6.71].$$

From analysis of Van Thienen-visser (2014) [69] and Van Wees (2017) [71] the movement of the fault is limited to the reservoir itself. This means that dimensions of the faults used in Eq. 6.70 and 6.71 can at its maximum be equal to the outer boundaries of the reservoir, especially in lateral extensive reservoirs the height of the reservoir, w , will be a limiting factor.

In all cases, Eq. 6.70 and 6.71, it is assumed that the seismic moment is directly released and is not effected by energy loss or changing friction properties of the fault. The assumption here is that the change in stress created by the injection (pressure, stress, and temperature differences) will be changed back into its original stress state by one single seismic event. This process is visualized in figure 6-15.

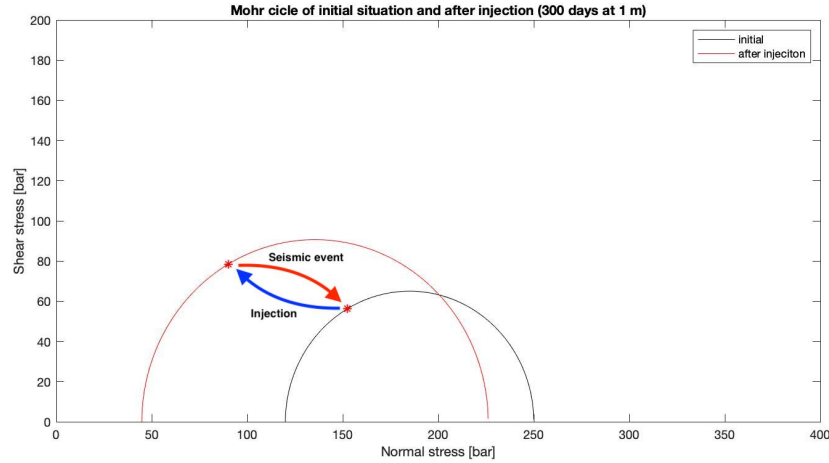


Figure 6-15. A Mohr plot with the initial Mohr circle and the Mohr circle after injection. The red asterisk is the orientation of the fault. The blue arrow indicated the decreased normal stress and increased shear stress acting on the fault from before and after injection. The red arrow indicates the maximal stress alteration one single seismic event can generate, assuming the total stress drop is used for one maximal event.

MOMENT MAGNITUDE

Now that the seismic moment is calculated it is only a simple step to the calculation of the moment magnitude, because it is only a logarithmic transformation (Hanks and Kanamori, 1979) [33]:

$$M_w = \frac{10 \log(M_0) - 9.1}{1.5} \quad [6.72]$$

where M_w = moment magnitude of a seismic event [-].

According to Abercrombie (1995) [1] the natural stress drop of a fault is between the 1 and 100 bar, while according to Van Thienen-Visser (2018) [69] induced events in the Netherlands (until now) have a maximum stress drop of 50 bar per event.

When the seismic moment is calculated is relatively easy to find the average slip of the fault. This is the displacement/offset change between the two sides of the fault. The average slip can be found by rearranging and differentiating Eq. 6.67 to:

$$u = \frac{M_0}{GA} \quad [6.73]$$

where G = shear modulus [Pa]

A = total area of the fault [m^2].

6.8 GROUND VIBRATIONS

To eventually get the best idea of the hazard created by the induced seismicity the moment magnitude needs to be converted into ground motion. The prediction of the ground motion during a seismic event is critical when it comes to the prognosis of risk for peoples and building damage. The most important feature of this ground motion prediction is the ground acceleration, which defines the seismic hazard on the ground level. The ground motion conversions from M_L are purely empirical and are different for every subsurface succession (stratigraphy) and depth of the seismic event. For the Groningen gas fields there are multiple ground motion prediction equation developed, these are

the most similar to the subsurface situation in the Netherlands. For comparison we are presenting two, created by the NAM [7] and TNO [49].

Important part of this step is the conversion of magnitude scales. In the previous section we used the more physically based moment magnitude M_w , while NAM and TNO observe the seismic event on the surface via a faster and standardized determination, the local magnitude M_L . Empirical studies about the conversion between these magnitudes show that in general the scaling is 1:1, but this is not the case for low magnitudes $M_L < 2.5$. In the Groningen case it has been shown that above $M_L = 2.5$, M_w is approximately 0.2 smaller. Leaving us with the equation:

$$M_L = M_w + 0.2 \quad \text{For } M_L < 2.5 \quad [6.74].$$

TNO MODEL

TNO developed its Ground Motion Prediction Equation (GMPE) in 2009 by investigating data from five earthquakes measured in Noord-Holland (2) and Groningen (3). The expected value for the vibration speed at a certain distance from the epicentre at ground level for the 5 cases is obtained from the attenuation relationship of the KNMI. The attenuation curve is calculated on the basis of the attenuation relationship of the KNMI for the Northern Netherlands, based on accelerometer data and borehole seismometer data (Dost, pers. Comm., 2007). The attenuation relationship is formulated as follows:

$$\text{Log}V_h(R_{epi}) = -1.83 + \log(OS) + 0.74M_L - 0.00139\sqrt{(d^2 + R^2)} - 1.33 \log\left(\sqrt{(d^2 + R_{epi}^2)}\right) \quad [5.75]$$

where R_{epi} = distance to epicentre [-]

d = depth of hypocentre [m]

M_L = local magnitude [-]

V_h = peak ground velocity [cm/s]

OS = opslingerfactor [-].

While all the parameters are self-explanatory, there is one that needs an introduction, the “opslingerfactor”. This factor is related to the relative shallow depth of the earthquake. Both the strength of the earthquake and the vibration of the surface are determined by the structure of the shallow surface. With a weak shallow surface, as we find in the Netherlands, the signal can be amplified. This amplification is called the opslingerfactor (“amplification factor”). The downside of this factor is that it is different for each location as the subsurface in the Netherlands changes a lot laterally, the difference between the subsurface in Groningen and Zuid-Holland for the first four kilometres not very similar.

The standard deviation in this attenuation curve is relatively high, namely $\sigma = 0.33$. The high uncertainty primarily originates from the great spread of speeds (peak ground velocity) at a certain distance emerged from the hypocentre of the earthquake. Apart from that the ‘opslingerfactor’ and the depth of the hypocentre add to the deviation.

NAM MODEL

The GMPE developed by the NAM was created in 2017, an improvement of the model created by TNO. This model is based on a database containing the data of 47 earthquakes, varying between an M_L of 1.8 to 3.6. Therefore this model is deemed useful for earthquakes with the magnitude in the range of $M_L = 1.8$ and 3.6. Though the use of this larger database they found the following equations, with the fundamental equation being

$$\ln(PGV) = c_1 + c_2 M_L + g(R) \quad [6.76]$$

where PGV = peak ground velocity [cm/s]

M_L = local magnitude [-]

$$R = \text{distance term} = \sqrt{R_{epi}^2 + [\exp(0.4233M - 0.6083)]^2}$$

R_{epi} = distance to epicentre [m].

The distance term, R , defines the magnitude-dependent near-source saturation of the attenuation curve. For the distance the geometrical spreading term is segmented over three distances:

$$g(R) = c_4 \ln(R) \quad R \leq 6.32 \text{ km} \quad [6.77]$$

$$g(R) = c_4 \ln(6.32) + c_{4a} \ln\left(\frac{R}{6.32}\right) \quad 6.32 < R \leq 11.62 \text{ km} \quad [6.78]$$

$$g(R) = c_4 \ln(6.32) + c_{4a} \ln\left(\frac{11.62}{6.32}\right) + c_{4b} \ln\left(\frac{R}{11.62}\right) \quad R > 11.62 \text{ km} \quad [6.79].$$

In order to find the coefficients of the functional form a maximum likelihood regression was performed. This resulted in the peak ground velocity coefficients of three definitions:

Table 6-2. Coefficients of Eq. 6.55-6.57 for the prediction of GPV

Coefficient	PGV _{GM}	PGV _{larger}	PGV _{maxrot}
C₁	-5.9357	-5.6419	-5.4801
C₂	2.4036	2.4613	2.4509
C₄	-1.8819	-2.0024	-2.0385
C_{4a}	-1.2274	-1.2137	-1.195
C_{4b}	-1.7343	-1.7721	-1.7878

For the NAM model the standard deviation is an integral part of the equations. As these equations predict rather a probabilistic distribution of the peak ground velocity than a deterministic estimates of unique values. Other than the TNO model this standard deviation, σ_{dev} , consist of two components; the between earthquake component, τ , and the within earthquake component, ϕ :

$$\sigma_{dev} = \sqrt{\tau^2 + \phi^2} \quad [6.80].$$

The values of the standard deviation are grouped per definition shown in Table 6-3. Table 6-3 also shows that on average the standard deviation is almost double the deviation the TNO model has.

Table 6-3. Standard deviations of the PGV prediction models

Coefficient	PGV _{GM}	PGV _{larger}	PGV _{maxrot}
τ	0.4226	0.428	0.4264
ϕ	0.4607	0.5167	0.5115
σ_{dev}	0.6252	0.671	0.6659

7. PHYSICAL SCREENING MODEL

The main aim in creating this Physical Screening Model, PSM, is to provide a quick quantification of the seismic hazard of a hydrothermal project before operation starts. This quantification includes modelling certain parameters like the density, vicinity and stress orientation of faults. From the results of this modelling the impact of the different parameters can be found, combined with a good indicator on the likelihood of this event happening in a (sedimentary) reservoir. This will be done by creating a simple analytical approach that will ultimately develop a Mohr plot and further more provide the corresponding ground vibrations, done by following the steps visualized in a diagram below. In this diagram the blue boxes symbolize input parameters while the green boxes embody the steps in which the calculations are done:

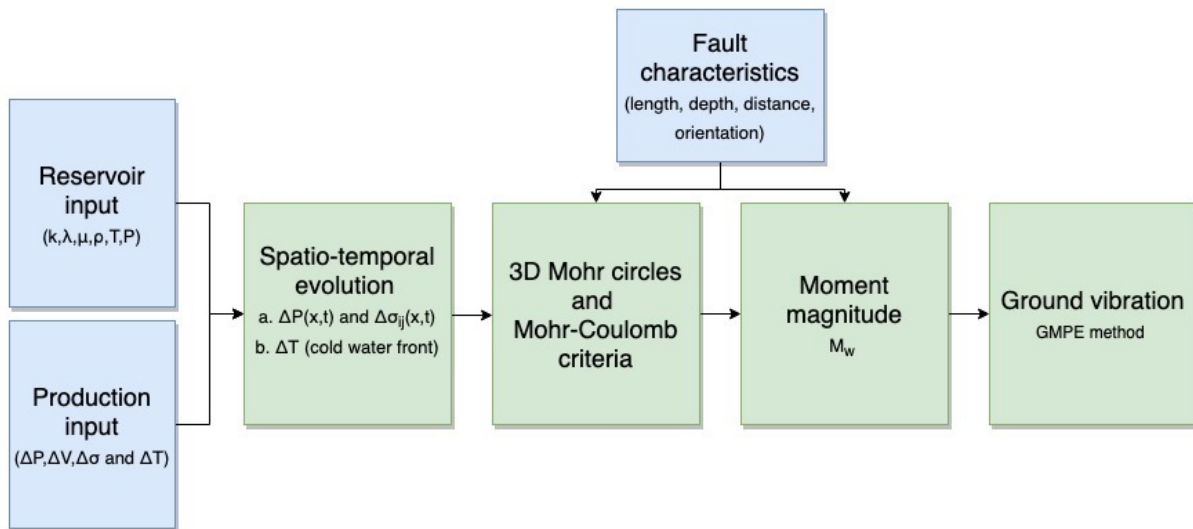


Figure 7-1. Schematic displays of the Physical Screening Model. In green: Step 1-4 of the PSM. In blue: Input parameters that form the basis for the calculations done in the steps.

The green boxes, step one to four, will be further elucidated in this chapter.

There are some big assumptions that hold for the entire physical model listed below, if steps have their individual assumptions they will be listen separately in the section itself. The main assumptions are:

- **Infinite homogeneous reservoir** – The reservoir in this model will be as general as it can be. This means that we assume the reservoir is homogeneous; all the reservoir parameters are isotropic. The focus is also only on this reservoir, thus we assume that it is infinite in all direction and no under or overlaying rock is present.
- **Constant injection rate** – When calculating the spatio-temporal evolution of the direct pore pressure, the poro-elastic stress and the thermal front, the injection rate should be held constant from the start of injection until the end.
- **Good inter-well connection** – In order investigate the fluid flow, pressure diffusion and thermo-elasticity originating from the injection well, the inter-well connection is considered to be good. Pressure accumulation due to the heterogeneity of the reservoir on the other hand can have influence on the model, but that will not be studied in this model.
- **Zero net injected volume** – In the model the boundaries should be such that there is no accumulation of pressure or water due to reservoir borders. This can be established by

making the reservoir model sufficient big or to create an artificial infinite boundary. This way the assumption that the injected water will be equal to produced water is established.

- **No (big) previous seismicity** – To solely examine the seismic activity originating from a single project the background seismicity should be considered absent. Even with this assumptions there still can be a substantial ((sub-)critical)pressure regime.
- **Far from basement** – As discussed before, any basement vicinity in this model is ignored. This model only looks at seismic hazards in the injected reservoir.
- **Open and permeable faults** – The faults in this model will be assumed to be open and permeable, as opposed to sealed and impermeable, making flow through the faults possible. This way pressure cannot build up close to the fault, which can lead to destructive stress alteration and ultimately to reactivation of this fault.
- **Normal fault regime** – In most parts of the deeper subsurface of the Netherlands (and the world in general) the stress regime acts like is does in a normal fault regime; the greatest principle stress, σ_1 , originates from the overburden and is in the vertical direction, while the other two principle stresses, σ_2 and σ_3 , act in the horizontal directions. While in this chapter all three regimes (normal fault, thrust fault and strike slip regime) will be discussed, eventually for the PSM only the normal fault regime will be included.
- **Horizontally extensive** – Similar to the previous assumptions also in this case most of the reservoirs in the sedimentary subsurface in the Netherlands are horizontally extensive. This means that this reservoir consist of little vertical height, often only an order of magnitude of 10s of meters, compared to its horizontal dimensions, often kilometres wide. This lateral extensive character has influence on the thermo-elastic calculations but also on the stress calculations and thus the Mohr circle directly. Instead of a spherical directional approach this model will regard at the reservoir in a radial orientation. Looking at this from a geo-mechanical standpoint this model will assume there is zero lateral strain and thus uniaxial compaction. For the reservoir stress this will mean that there will be no change along the vertical direction while the horizontal stress will change and have influence on possible fault reactivation.

7.1 PSM STEP 1A: SPATIO-TEMPORAL EVOLUTION OF STRESS AND PRESSURE

Following the diagram in figure 7-1, the first step of this Physical Screening Model will be the spatio-temporal evolution of pore pressure, stress and temperature. As discussed in chapter 6 the diffusion calculations of all three parameters will be done analytically. With PSM Step 1a the first two, the diffusion of direct pore pressure and poro-elastic stress, will be evaluated. For the analytical investigating the spatio-temporal evolution of the pore pressure and stress change the equations of Rudnicki (1986) are used, from section 6.5. These equations provide the changes of stress and pore pressure distribution for a continuous flow of fluid injection:

$$\Delta P(x, t) = \frac{\Phi}{\rho_{fc}} \frac{1}{4\pi r} \left[\frac{(\lambda_u - \lambda)(\lambda + 2G)}{\alpha^2(\lambda_u + 2G)} \right] \operatorname{erfc}\left(\frac{1}{2}\xi\right) = \frac{\Phi}{\rho_f} \frac{1}{4\pi r} \frac{\eta}{k} \operatorname{erfc}\left(\frac{1}{2}\xi\right) \quad [6.26]$$

$$\Delta\sigma_{ij}(x, t) = -\frac{\Phi}{\rho_{fc}} \frac{(\lambda_u - \lambda)G}{4\pi r\alpha(\lambda_u + 2G)} \left\{ \delta_{ij} \left[\operatorname{erfc}\left(\frac{1}{2}\xi\right) - \frac{2}{\xi^2} g(\xi) \right] + \frac{x_i x_j}{r^2} \left[\operatorname{erfc}\left(\frac{1}{2}\xi\right) + \frac{6}{\xi^2} g(\xi) \right] \right\} \quad [6.27]$$

with $g(\xi)$ being:

$$g(\xi) = \frac{1}{2\sqrt{\pi}} \int_0^\xi s^2 \exp\left(-\frac{1}{4}s^2\right) ds = \operatorname{erf}\left(\frac{1}{2}\xi\right) - \frac{1}{\sqrt{\pi}} \xi \exp\left(-\frac{1}{4}\xi^2\right) \quad [6.28].$$

It is assumed that the system is isotropic and homogeneous, meaning there is radial symmetry and only the radial and tangential stress components are considered. From section 6.5 the following equations are used to describe the radial and tangential stress components, first for radial stress:

$$\Delta\sigma_{rad}(x, t) = -\frac{\Phi}{\rho_{fc}} \frac{(\lambda_u - \lambda)G}{4\pi r \alpha(\lambda_u + 2G)} \left[2 * \operatorname{erfc}\left(\frac{1}{2}\xi\right) + \frac{4}{\xi^2} g(\xi) \right] \quad [6.29]$$

and for tangential stress:

$$\Delta\sigma_{tan}(x, t) = -\frac{\Phi}{\rho_{fc}} \frac{(\lambda_u - \lambda)G}{4\pi r \alpha(\lambda_u + 2G)} \left[\operatorname{erfc}\left(\frac{1}{2}\xi\right) - \frac{2}{\xi^2} g(\xi) \right] \quad [6.30].$$

7.1.1 RESULTS

Using Rudnicki's Eq. 6.26, 6.29 and 6.30 the following results could be obtained. When primarily looking at the pressure and stress difference at a certain location and moment in time it is important to keep all the input parameters equal. This will be done for this entire chapter in which the screening model is presented, unless when specifically mentioned differently. The input parameters are divided into either reservoir parameters or flow/production parameters. In the table below the input parameters of PSM Step 1a are given.

Table 7-1. Input parameters of PSM step 1a

Input parameter	Symbol	Used in model
Permeability	k [m2 or D]	3*10 ⁻¹³ m2 ~ 0.3 Darcy
Biot-Willis coefficient	α [-]	0.70
Shear modulus	G or μ [Pa]	7 GPa
Lame parameter (drained)	λ [Pa]	6 GPa
Lame parameter (undrained)	λ _u [Pa]	7.98 GPa
Poisson ratio	ν [-]	0.25
Young modulus	E [Pa]	15 GPa
Bulk modulus	K [Pa]	10.7 GPa
Fluid density	ρ [kg/m3]	1000
Fluid viscosity	η (Pa.s)	0.4*10 ⁻³
Volumetric flow rate	Q [m3/s]	250

Note that the parameters used here are not automatically corresponding to the typical South Holland basin fluvial sandstone reservoirs.

OVER DISTANCE

First a look is taken at the distribution of pressure and stress over distance. By setting the time at 1000 days for the start of the injection, the distribution profile can best be observed. Figure 7-3 show this spatial distribution for this system with the location from the injection on a logarithmic scale, to emphasize the top in ΔP and Δσ_{poro}.

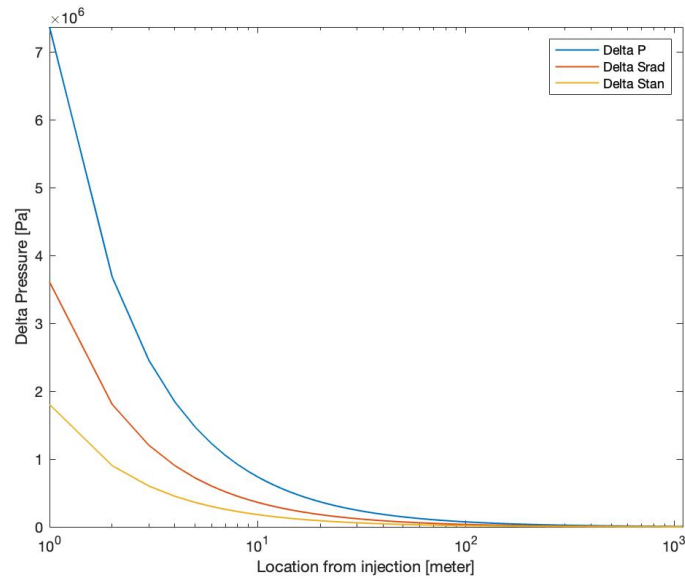


Figure 7-3. Plot of the ΔP , $\Delta\sigma_{rad}$ and $\Delta\sigma_{tan}$ diffusion over location from the injector after 3000 days of injection. The scale of x-axis that represents the distance from the injector is logarithmic.

From figure 7-3 is observed that the pore pressure (ΔP) decreases faster over distance than the radial and tangential stress difference ($\Delta\sigma_{poro}$). The direct pore pressure also starts at a bigger disparity than $\Delta\sigma_{poro}$. This phenomenon can be explained by the different ways of progradation of the stress and pore pressure through the subsurface. Pore pressure difference is created in the pores of a matrix and flows through these pores (as the name indicates) and thus the speed of the direct pore pressure diffusion strongly depends on the void spaces of the rock and thus the permeability of the rock. The poro-elastic stress on the other hand is transferred by the matrix of the rock, via the solid grains. Pressure and stress waves generally travel faster through rock than through water or air. As permeability becomes larger, the pores are generally getting bigger, thus relatively decreasing the grains share. This will lead to lower pressure differences and an even faster decrease. The exact effects on the permeability will be covered in the sensitivity chapter. Figure 7-3 further displays the quantitative difference between the tangential and the radial stress, where the radial stress is almost twice as big as the tangential stress.

The graph in figure 7-4 displays the same lines as figure 7-3 only here the x-axis does not have a logarithmic scale. After 1000 days of injection the tangential stress is negative from about 800 meters of the injector. This indicates that the tangential stress becomes slightly tensile at larger distances, while it is compressive in the first 800 meters. In general it means that tangential stress starts off tensile but later adds to the general compressive behaviour of the injection process.

Both the radial and tangential stresses still have non-zero values long after the ΔP has decreased to 0, in this case after 2200 meters. Even more significant is that $\Delta\sigma_{rad}$ is greater than the ΔP after ± 1000 meters. Both these differences between the stress and pressure are due to the different nature of diffusion explained earlier. A result of the lengthier range of the poro-elastic stresses can lie in the reactivation of faults that do not lay in the reservoir itself but for instance the basement. This stress change can provide seismic problems [28].

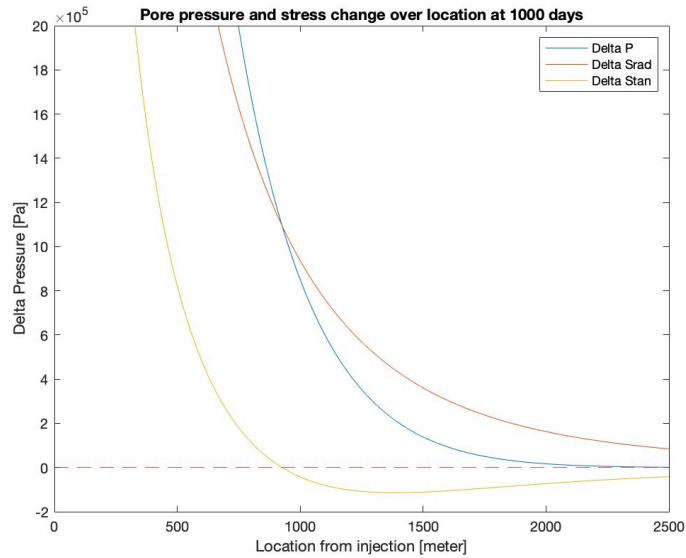


Figure 7-4. Plot of the ΔP , $\Delta\sigma_{rad}$ and $\Delta\sigma_{tan}$ diffusion over location from the injector after 1000 days of injection. Normal scales on both axis's, while the y-axis is limited at 2 MPa.

In order to visualize the rate at which the ΔP and the $\Delta\sigma_{poro}$ 'settle' inside a typical 1100m radius reservoir figure 7-5 shows the ΔP after different injection periods. See Appendix D for the figures for $\Delta\sigma_{rad}$ and $\Delta\sigma_{tan}$. For ΔP the settling period arises fairly quickly. While after only 1 day of injection the pressure inside the reservoir is changed by a significant amount even at its outer boundary (1100M in this case). The ΔP , over the whole reservoir, does not change significantly anymore after about 100 days, when maintaining the same injection rate.

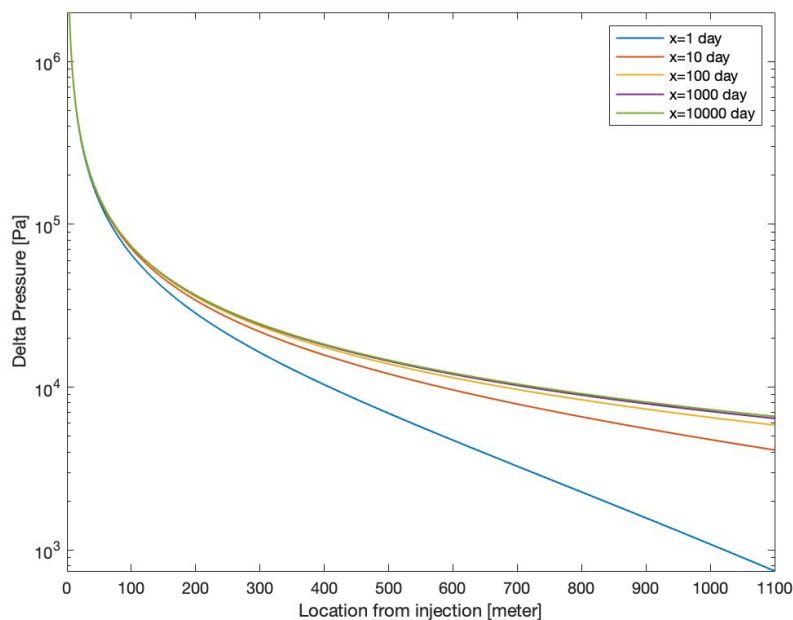


Figure 7-5. Plot of the ΔP over location from the injector after five different time scales. The change in pore pressure over the whole system is negligible after 100 days, while this holds after 1 day up to a 75-meter radius from the injector.

To give a good overview of the pressure disturbance in a typical reservoir figure 7-6 shows a top view map. The horizontal reach of the ΔP is visualized after 4 intervals, 1 to 10000 days.

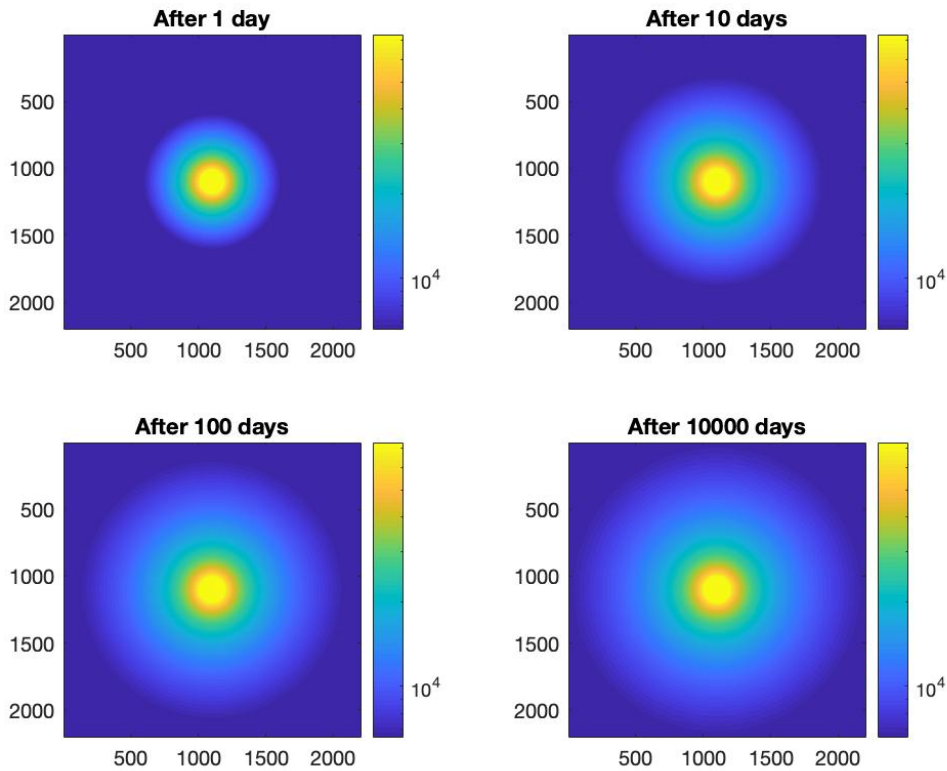


Figure 7-6. Top view of the reservoir for the diffusion of ΔP after four different time intervals.

OVER TIME

After presenting the changing pore pressure and stress over location, now the temporal evolution of the ΔP and the $\Delta\sigma$ will be demonstrated. With taking the same parameters as in Table 7-2, figure 7-7 gives the evolution of ΔP , $\Delta\sigma_{\text{tan}}$ and $\Delta\sigma_{\text{rad}}$ over time at 4000 meters from the injector. Both the $\Delta\sigma_{\text{tan}}$ and $\Delta\sigma_{\text{rad}}$ react almost directly after injection even at 4000 meters from the injection point, while ΔP takes a few days to arrive. This phenomenon can once more be credited to the different physical way of diffusion as computed before. At 4000 meter from the injection the values of ΔP are insignificantly low, but in Appendix D it can be seen that when decreasing the permeability and thus the diffusive character of the reservoir the values are found to be much higher.

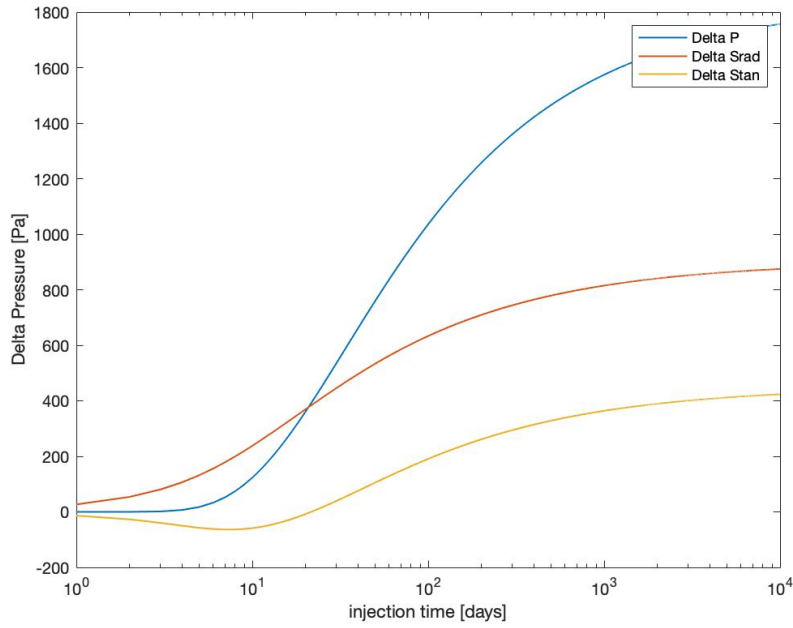


Figure 7-7. Plot of the ΔP , $\Delta\sigma_{rad}$ and $\Delta\sigma_{tan}$ diffusion over time from the injector after 3000 days of injection. The scale of x-axis that represents the injection time is logarithmic.

Here again it can be observed that the tangential stress is negative and thus tensile before becoming compressional after ± 50 days. Since the stresses are affected prior to the pore pressure difference, for the first couple of days the radial stress will be higher and have more influence than the ΔP . About ± 20 days into the operation the ΔP surpasses the $\Delta\sigma_{rad}$ quickly. The regressing shape of all the three lines indicate that after ± 200 days about 70% of the total changes in pore pressure and stress changes are made, while after ± 1000 days almost all of it is done.

7.2 PSM STEP 1B: SPATIO-TEMPORAL EVOLUTION OF TEMPERATURE

In geothermal operations warm water is produced and used as an energy source. On the injector side cold water is injected into the subsurface. This results in heat depredation in the reservoir. The governing equation used in model was introduced in section 6.6 and can be written as

$$T(x, t) = T_0 - \frac{2}{\pi^2} (T_0 - T_{in}) \exp\left(\frac{K_2 x}{2\lambda}\right) \int_L^\infty \exp\left(-\zeta^2 - \frac{K_2^2 x^2}{16\lambda^2 \zeta^2}\right) d\zeta \quad [6.66].$$

Using this equation the reservoir temperature can be calculated at any given time and location, just like PSM Step 1A, where the diffusion of pressure and stress are calculated.

In this model the temperature is calculated by the axisymmetric heat transport Eq. 6.66 in porous medium. The model considers the reservoir to be homogeneous and infinite. It is important to note that in this model no upper and underlying rock or interlaying clay layers are included, these elements can influence the temperature distribution by emitting external heat.

Illustrated in section 6.6 the ΔT influence the stress levels inside the reservoir. The simple expression given to convert this difference in heat to stress difference is given by Eq. 6.59. In combination with the bulk modulus the thermal stress decrease due to the cold injection water is:

$$\Delta\sigma_T = \frac{\alpha_t E \Delta T}{(1-\nu)} \quad [6.59].$$

In a normal faulting regime the horizontal effective stresses are reduced due to the contraction of the reservoir rocks, as earlier described where cooling of the rock leads to thermal-contraction. The vertical effective stresses are primarily determined by the weight of the overburden rock and thus are no subject to thermal-contraction [10].

7.2.1 RESULTS

With the temperature calculations a different influence on the stress alterations inside a producing reservoir is calculated. This is a unique element of geothermal operation, the thermal difference inside a reservoir can have a significant influence on the stress “situation” and thus on possible fault reactivation. The input parameters used are listed in Table 7-2. The input parameters of PSM Step 1A remain the same.

Table 7-2. Input parameters of step 1B

Input parameter	Symbol	Used in model
Initial temperature	T_0 [°C]	70
Injection temperature	T_{in} [°C]	35
Density of rock	ρ_r [kg/m ³]	2650
Heat capacity of rock	C_r [J/kg°C]	850
Heat capacity of water	C_w [J/kg°C]	4180
Thermal conductivity of the porous media	λ [W/m °C]	2
Linear thermal expansion factor	α_v [-]	1^{-5}

The results from the temperature evolution though the reservoir is fairly simple, because of the homogeneous character of the reservoir. The temperature of the reservoir gradually decreases as the thermal front moves through the reservoir. The velocity of this front is reasonably slow as can be seen in figure 7-8, it fully depends on the flow velocity of the water inside the reservoir, which mainly realise on the injection pressure and the permeability of the rock (see section 8.1.1). According to figure 7-8, after about 25 years the temperature of the reservoir at 500 meters from the injector is cooled down to 35 °C. Figure 7-9 indicates that after 21 years the temperature at a 600 meter radius from the injector is indeed still 70 °C.

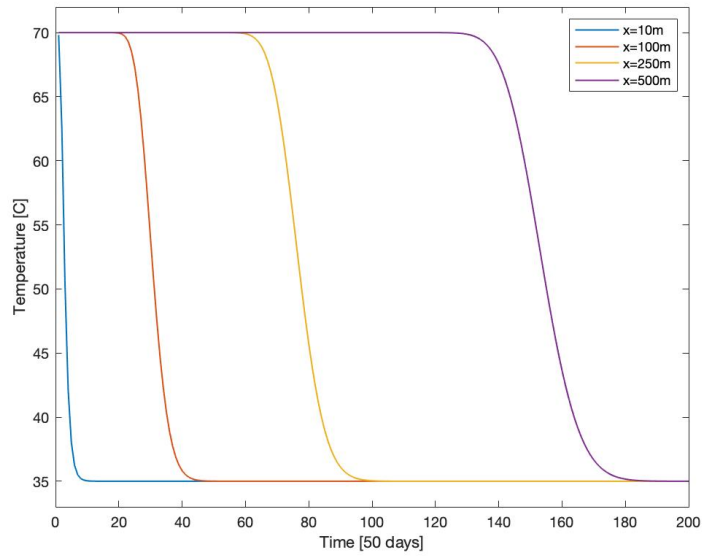


Figure 7-8. Plot of the thermal front evolution over time at four different locations, 10, 100, 250 and 500 meters from the injection point. Note that it takes longer for the thermal front to decrease the reservoir temperature at a farther distance from the injector. The x-axis has a 50 day time scale.

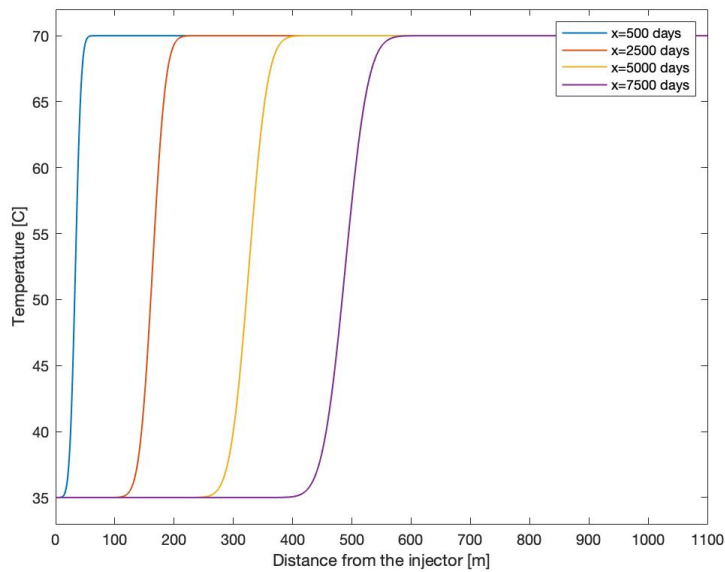


Figure 7-9. Plot of the thermal front evolution over location at four different time intervals, 500, 2500, 5000 and 7500 days of injection. Note that it takes longer for the thermal front to decrease the reservoir temperature at a farther distance from the injector, just as in figure 7-8. The thermal front becomes more lateral extensive.

Noteworthy is that the length of the thermal front increase over time. While the length of the transition between 35 °C and 70 °C after 500 days is ± 50 meters long, it enlarges to ± 200 meters after 7500 days of injection.

The stress decrease due to the temperature is linear to the temperature change, assumed that no changes or movement have occurred to the reservoir after the lowering of the temperature. In figure 7-10 it can be seen that the stress decrease with the current input parameters never exceeds 40 bar. When comparing figure 7-8 and 7-9 with figures 7-10 and 7-11 the relatively linear relation between temperature and stress change is visible.

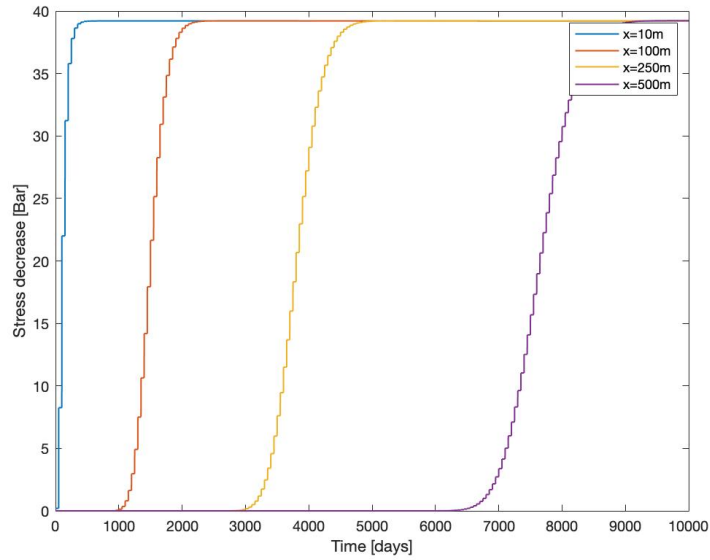


Figure 7-10. Plot of the thermal stress evolution over time at four different locations, 10, 100, 250 and 500 meters from the injection point. The stress follows the same but inverted path of figure 7-8.

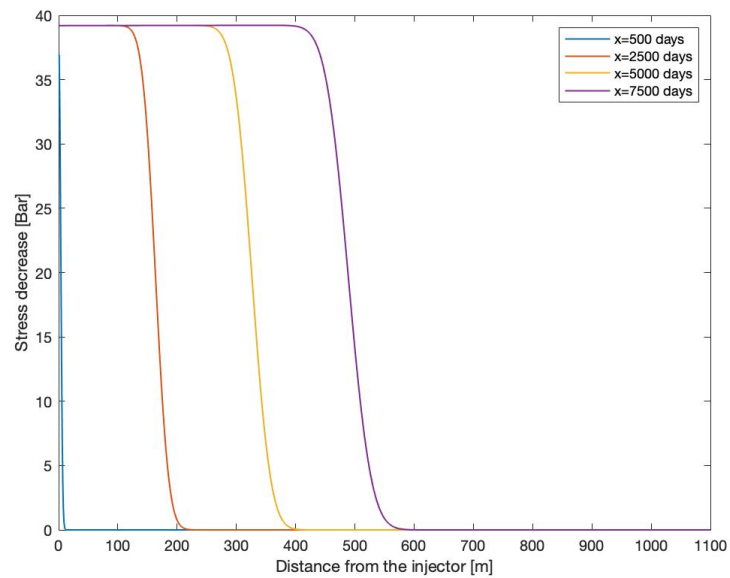


Figure 7-11. Plot of the thermal stress evolution over location at four different time intervals, 500, 2500, 5000 and 7500 days of injection. The stress follows the same but inverted path of figure 7-9.

In order to show the lateral change in temperature the four figures below illustrate the temperature diffusion at four different time intervals from a top view angle of the reservoir.

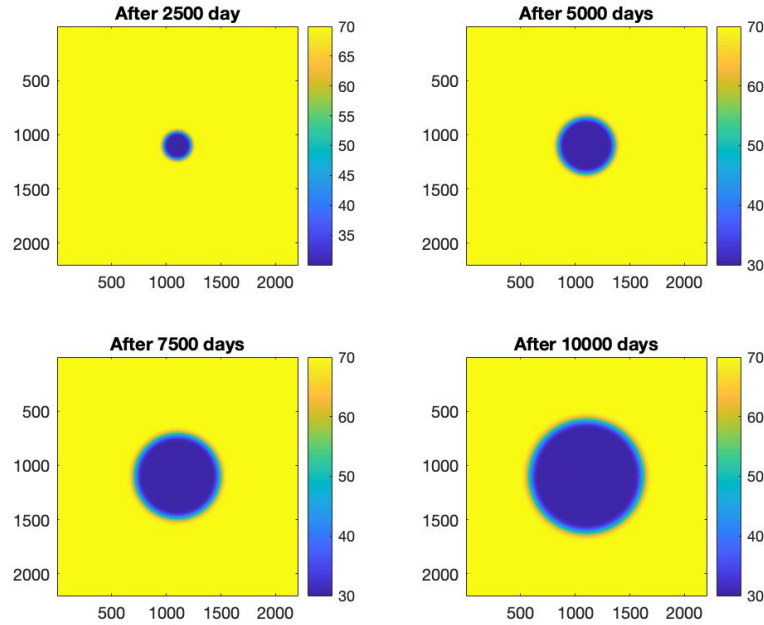


Figure 7-12. Top view of the reservoir for the diffusion of the thermal front after four different time intervals.

7.3 PSM STEP 2: STRESS STATE

In geotechnical engineering the best way to visualize the stress state in the subsurface is by making a Mohr circle of the subsurface stress situation, the same holds for fractures and/or faults strength calculations. The second step of the Physical Screening Model will provide a visual aid for the investigation of the fault stability. In section 6.3 is the usage of the Mohr circle and the Mohr-Coulomb criterion in this situation explained and thereby provided the three main equations for these calculations:

$$\sigma_n = \frac{1}{2}(\sigma_1 + \sigma_3) + \frac{1}{2}(\sigma_1 - \sigma_3) \cos\left(\frac{\theta\pi}{180}\right) \quad [6.5]$$

$$\tau = \frac{1}{2}(\sigma_1 - \sigma_3) \sin\left(\frac{\theta\pi}{180}\right) \quad [6.6]$$

$$\tau = c + \sigma \tan(\varphi) \quad [6.8].$$

Now these equations will be used with the changing pore pressure, poro-elastic stresses and temperature calculated in the previous step. With that a Mohr plot can be created.

7.3.1 EFFECTIVE STRESS

In geothermal reservoirs fluids are injected: Increasing the fluid pressure in a reservoir causes pressure in the connected pore space of rocks to increase (the pore space includes pores, cracks, vicinities of grain contacts, and all other possible voids in rocks). This leads to an increase of pore pressure at the critical locations as well. Such an increase consequently causes a decrease of the effective normal stress, usually acting compressional on arbitrary internal rock surfaces. This leads to sliding along pre-existing, favourably oriented subcritical faults [56]. The sliding along these faults can lead to seismic activity, especially close to the injection well. The effective stress σ_{eff} is affected by a changing pore pressure, which is calculated in PSM Step 1.

OBSERVATION POINT

Discussed in 6.4.3 the observation point, i.e. fault, influences the relative direction of the pore-elastic stresses and thus the change in effective stress. Changing the location of the fault or its local stress regime can ultimately have critical effects on the prediction of fault failure. In order to fit the equations of 6.4.3 into this model certain changes have to be made.

NORMAL FAULT REGIME

The reservoir for this PSM is assumed to be laterally extensive, instead of the spherical direction only the horizontal radial direction is regarded. This means that within the boundaries of the reservoir the vertical length is limited leading to zero lateral strain and uniaxial compaction. As this is the case most Dutch geothermal systems, in further calculations the Mohr circles will only be calculated for observation points in the horizontal direction. Changing Eq. 6.37 and 6.38 and using the following alterations of eq. 7.1 and 7.2, where in the vertical stress direction, σ_V , (also the largest primary stress, σ_1) no poro-elastic stress is added:

$$\sigma_1 = \sigma_{V,eff} = \sigma_V - \Delta P(x, t) \quad (\text{with coupling and T}) \quad [7.1]$$

$$\sigma_3 = \sigma_{h,eff} = \sigma_h - \Delta P(x, t) + \Delta\sigma_{rad}(x, t) - \sigma_T(x, t) \quad (\text{with coupling and T}) \quad [7.2].$$

THRUST FAULT REGIME

In a thrust fault regime the same principles are applied as with the normal fault regime, as the reservoir is assumed to be horizontally extensive Eq. 6.43 and 6.44 should be altered to:

$$\sigma_1 = \sigma_{H,eff} = \sigma_H - \Delta P(x, t) + \Delta\sigma_{rad}(x, t) - \sigma_T(x, t) \quad (\text{with coupling and T}) \quad [7.3]$$

$$\sigma_3 = \sigma_{V,eff} = \sigma_V - \Delta P(x, t) \quad (\text{with coupling and T}) \quad [7.4].$$

STRIKE SLIP REGIME

In strike slip regimes the principal stresses are classified like this: $\sigma_1 = \sigma_h$, $\sigma_2 = \sigma_v$ and $\sigma_3 = \sigma_h$. This implies that both the maximal and the minimal stresses extend along the horizontal axis and thus no changes follow.

7.3.2 RESERVOIR STRESS CALCULATIONS

Initial stress in Mohr circle is simply calculated by the lithostatic gradient and the minimal horizontal gradient:

$$\sigma_1 = d_{aq} * Litgrad - P_{aq} \quad [7.5]$$

$$\sigma_3 = d_{aq} * Horgrad - P_{aq} \quad [7.6]$$

$$\sigma_2 = d_{aq} * Horgrad2 - P_{aq} \quad [7.7]$$

where d_{aq} = depth of aquifer [m]

Litgrad = lithostatic gradient [-]

Horgrad = minimal horizontal gradient [-]

Horgrad2 = $1.32 * Horgrad - 0.32 * \text{hydrostatic gradient}$ = maximal horizontal gradient [-]

P_{aq} = aquiferic pressure [Pa].

7.3.3 RESULTS

With the equations from the section above, Mohr plots can be created at every time and at every location from the injection well. Thus, in case a fault is positioned at a certain location within the producing reservoir, it can be shown at which time there might be risk of reactivation or if there will be no risk at all.

The results in this part will only include calculations concerning a normal fault (stress) regime, as this is in many parts of relatively deep the subsurface in the Netherlands the case. For additional results from the thrust fault and strike slip regimes, see appendix E.

The specific input parameters used in this step are listed in Table 7-3 below. The parameters from the previous step remain the same.

Table 7-3. Input parameters of PSM Step 2

Input parameter	Symbol	Used in model
Cohesion	C [Pa]	0
Internal friction angle	Φ [-]	33
Lithostatic gradient	-	0.225
Hydrostatic gradient	-	0.106
Minimal horizontal gradient	-	0.16
Depth aquifer	d_{aq} [m]	2500

Investigating the two different observation points in a normal fault regime results in the two different Mohr circles displayed in figure 7-13. In this figure only the different observations points are regarded at, this means no thermal elasticity, $\Delta\sigma_T$, is included here, using Eq. 7.1, 7.2, 7.3, 7.4, 6.49 and 6.50 (leaving out the thermo term in all equations). As explained before, as the assumptions is that the geothermal reservoir is horizontal and laterally extensive the model will only incorporate the Mohr circle calculations in the horizontal direction, using Eq. 7.1 and 7.2.

To provide a good indication of what a Mohr circle in this case would look like, the results of the Mohr circle after 3000 days of injection in a 1-meter radius from the injection well are shown in figure 7-14. Figure 7-14 primarily highlights the difference between the Mohr circles without coupling, with coupling and with coupling and Temperature. The graph corresponds to the steps the Mohr circle is expected to move in this situation, like described in chapter 6 and visualized in figures 6-6 – 6-11. The circle moves to the left when only the pore pressure is accounted for, then it slightly shifts to the left while it also becomes smaller when also poro-elastic coupling is taken into account and finally it relocates to the top left when thermo-elasticity is included.

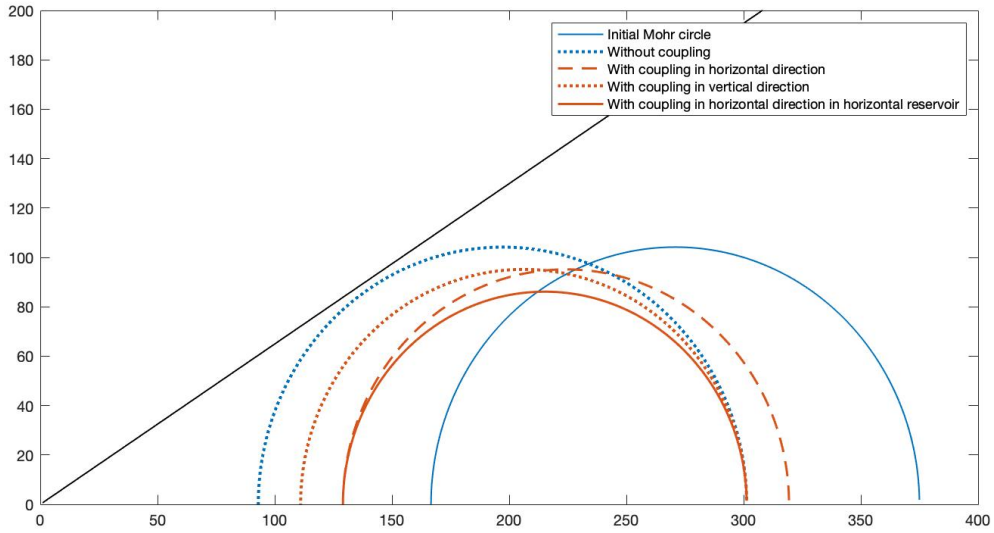


Figure 7-13. Mohr plot with the two different observation points and a failure envelope. Except for the initial Mohr circle all the Mohr circle are after 3000 days of injection at a 1-meter radius from the injector. The three red Mohr circles include $\Delta\sigma_{poro}$ but not $\Delta\sigma_T$. The dotted blue Mohr circle is without thermo-elastic and poro-elastic coupling.

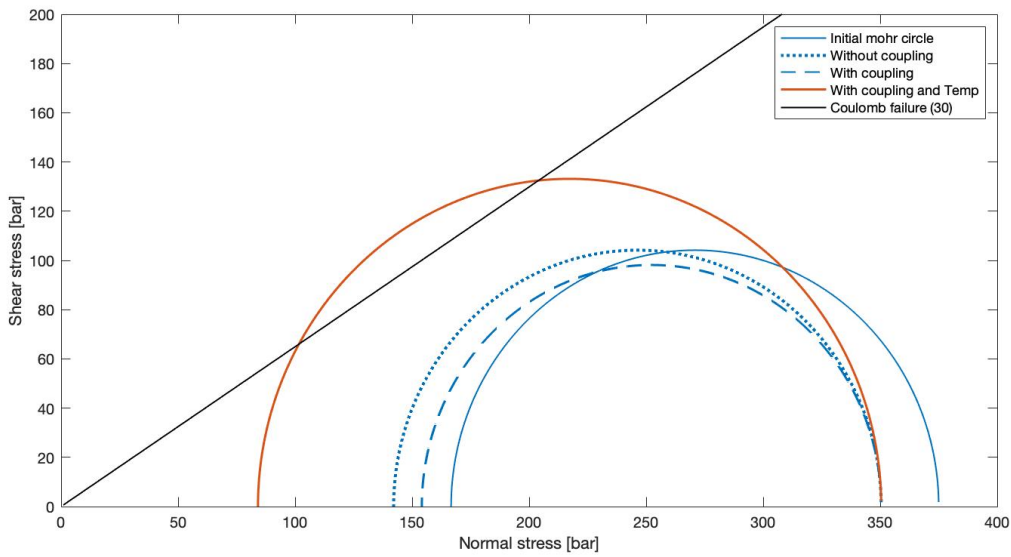


Figure 7-14. Mohr plot with four different Mohr circles and a failure envelope. Except for the initial Mohr circle all the Mohr circle are after 3000 days of injection at a 3-meter radius from the injector. The difference between the Mohr circles with and without poro-elastic coupling is considerable.

Figure 7-15 emphasizes more on the end result and only shows the initial Mohr circle before injection and the Mohr circle after injection, including ΔP , $\Delta\sigma_{poro}$ and ΔT . It also acknowledges the minimum and maximum angle of the fault plane with the minimal principle stress. In this example the angles in the figure 7-15 correspond for the θ_{min} , 46.3° , and the θ_{max} , 68.7° . These are found by calculating the interceptions between the Mohr circle and the Mohr-Coulomb friction coefficient.

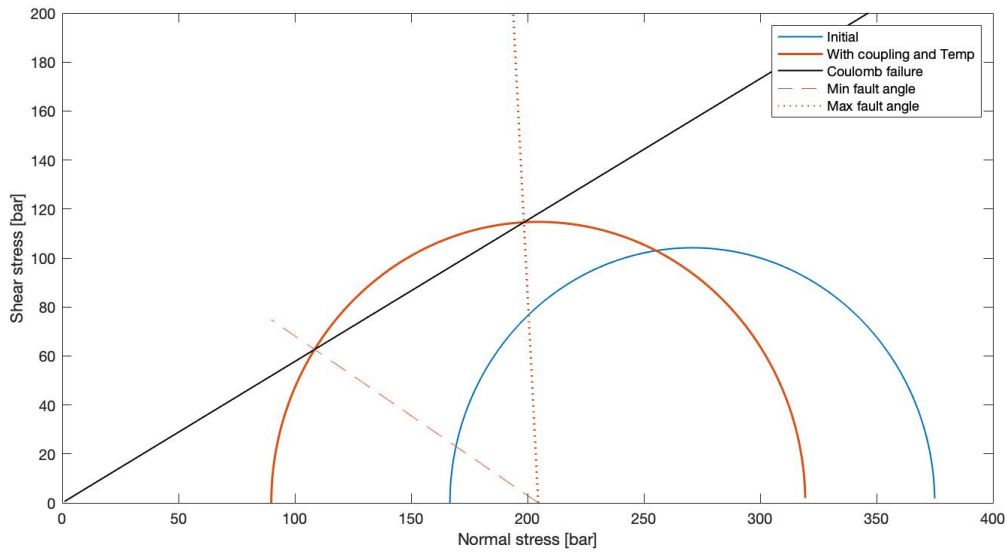


Figure 7-15. Mohr plot including the initial Mohr circle and the Mohr circle after injection. The dotted lines indicate the maximum and minimum angle of the fault plane with the minimal principle stress. If the fault plane lies between the two angles found in this figure the fault lays in the unstable zone.

The orientation and location of the fault as well as the angle with respect to the principle stresses (σ_1 , σ_2 and σ_3), and thus with respect to the in-situ stress (σ_v , σ_H and σ_h), needs to be known or in many cases assumed. In the figure 7-16 the most critical orientation of the fault is shown, this is the case when the fault make a 30° angle with σ_1 , a 60° angle with the σ_3 , and 90° angle with σ_3 .

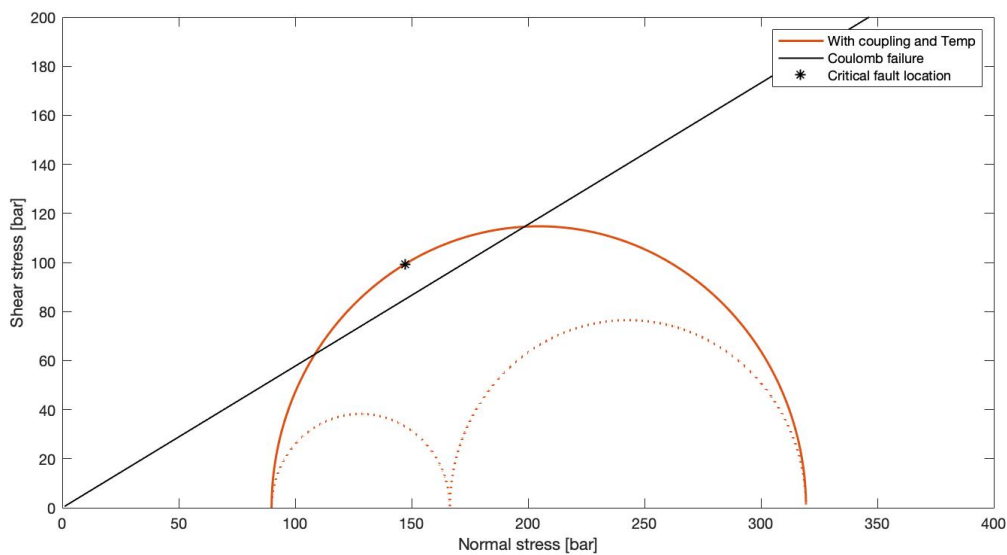


Figure 7-16. An example of the critical fault orientation, which lies in the unstable zone.

In the figure 7-16 it can be observed that the fault is in the most unstable location, it is further above the Mohr-Coulomb failure criterion. The location of the fault and its corresponding stress alteration compared with the initial stress situation in the fault will be important in PSM Step 3, section 7-4, when determining the seismic moment.

In general the orientation of the fault can differ in all direction but in the Mohr diagram it only can be placed between the two smaller circles and the big circle, indicated with the red surface in the figure below 7-17.

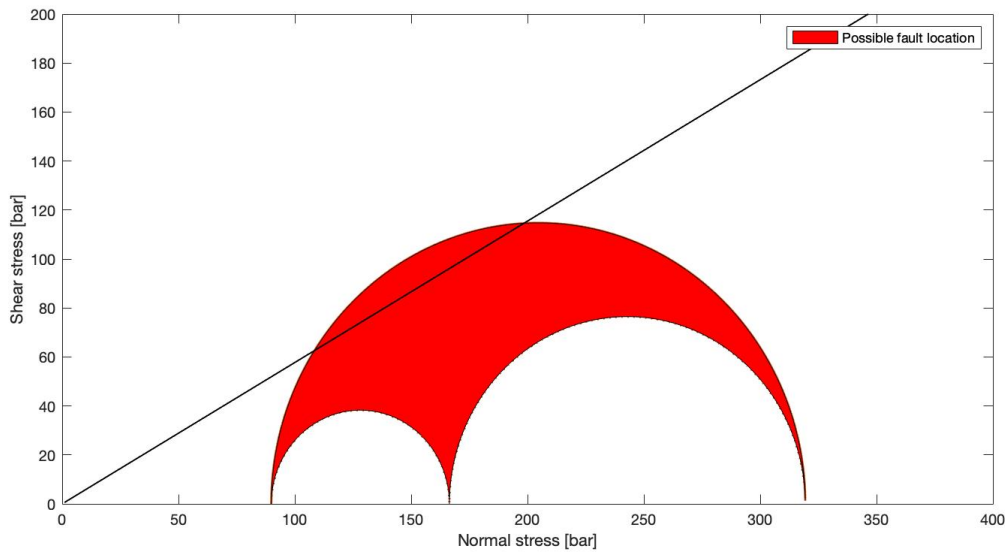


Figure 7-17. The red area of the Mohr circle indicates the possible orientation of the fault.

Figure 7-18 shows Mohr circles at different locations after 3000 days of injection, varying from 1 to 100 meter distance of the injector. The most important observation is that between a 0 to 10 meter radius of the injector faults, with the right critical angles, are unstable. Beyond this 10 meter radius the Mohr circle lies completely in the stable region. After 10 meters the effect of ΔP and $\Delta\sigma_{\text{poro}}$ is neglectable and the $\Delta\sigma_{\text{termo}}$ will be the dominating factor in decreasing the stress. This is because the permeability is relatively good; with lower permeabilities the influence of ΔP and $\Delta\sigma_{\text{poro}}$ will reach farther into the reservoir.

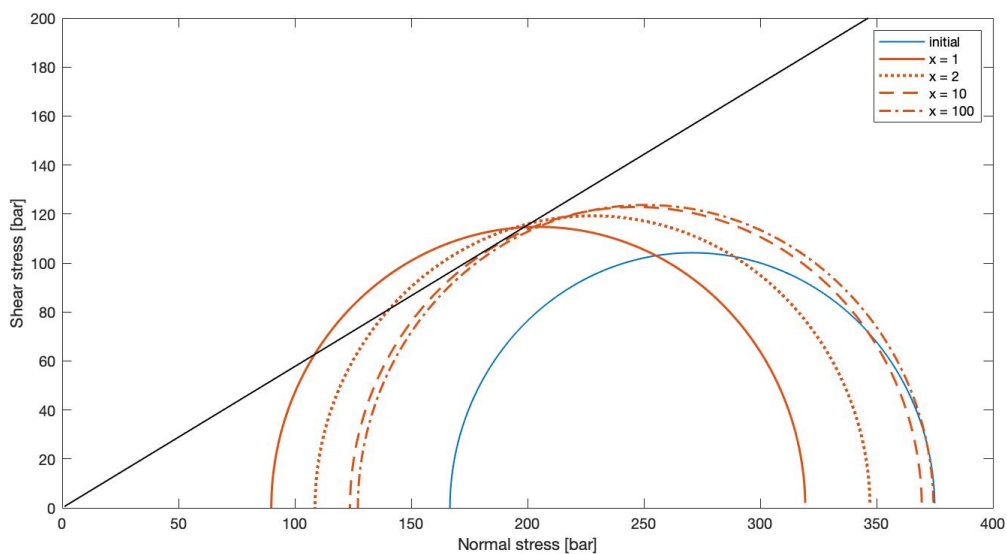


Figure 7-18. Mohr circles at different locations after 3000 days of injection, varying from 1 to 100 meter distance of the injector.

7.4 PSM STEP 3: FROM STRESS TO SEISMIC MOMENT

Where a Mohr-Coulomb failure criterion is a sophisticated manner of showing when a fault or fracture is stable or unstable, it does not indicate what the gravity of the situation is, it does not show how strong a possible failure or how much slip a fault can go for. Step 3 of the PSM approach is the conversion from stress difference to moment magnitude, M_w . The relation between those two is investigated in section 6.7, resulting in two slightly different methods for defining the moment magnitude and three Eq. 6.70, 6.71 and 6.72. The first originates from Madariaga (1979) [41] and can be used for simple round faults:

$$M_o = \frac{16}{7\pi} R \Delta \sigma A \quad [6.70]$$

While the second method by Stein (2006) [60] is used for rectangular faults:

$$M_o = \frac{3\pi}{8} \Delta \sigma (w^2 L) \quad [6.71]$$

The moment magnitude is subsequently calculated by:

$$M_w = \frac{10 \text{Log}(M_o) - 9.1}{1.5} \quad [6.72]$$

To investigate the moment magnitude the dimensions of the fault needs to be known or assumed. In a SRA, which eventually will lead to the design of mitigation measures, the magnitude of the moment depends on the slip-dependent reduction of the faults strength, cohesion and friction.

The average slip of a seismic event is found by rearranging and differentiating Eq. 6.51 to:

$$u = \frac{M_o}{GA} \quad [6.73].$$

7.4.1 RESULTS

In the results only rectangular faults will be assumed, thus using only Eq. 6.71 and 6.72. The results of this step will only consist of two numbers, the seismic moment M_o and the moment magnitude M_w . These numbers will be subject to a substantial amount of assumptions but it will present an indicative seismic moment that corresponds to a certain stress drop within the fault. Continuing on the previous two steps, thus after 3000 days of injection, the fault is located at a 3 meter radius from the injector and the fault is orientated in its most critical orientation (with the primary stress orientations), then according to Eq. 6.71 and 6.72 the M_o and M_w are $9.50 \cdot 10^{12}$ Nm and 1.91, respectively. This is assuming we are dealing with a 10m (height) by 2000m (length) rectangular fault.

To get a better overview of the evolution of the moment magnitude figure 7-19 show the M_w at a 3-meter radius from the injection over time. This graph gives an indication of the magnitude of the seismicity if the fault is most favourably orientated and critically stressed. In other words, when the fault lies in the unstable zone of the Mohr diagram (in the red area that crosses the Mohr-Coulomb envelope in figure 7-16, section 7.3) and it slips at a certain time, then the maximum moment magnitude can be read from the graph in figure 7-19 corresponding with that specific time, x-axis, and location, 3 meters from the injector in this case.

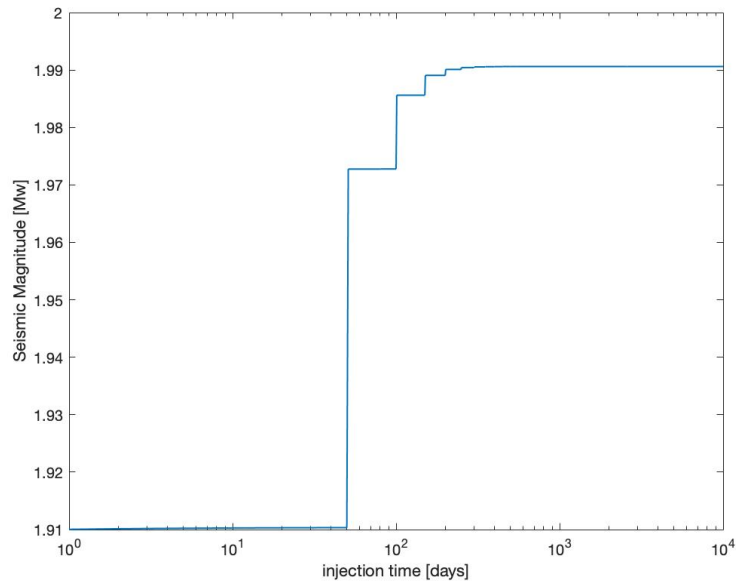


Figure 7-19. Plot of the maximum moment magnitude of a seismic event over injection time at a 3-meter radius from the injector. This gives an indication of the maximum magnitude of one single event if the fault lies in the unstable zone of a Mohr plot.

Figure 7-20 illustrates the moment magnitude over time after 3000 days of injection. This figure gives once more the maximum moment magnitude of an seismic event, but here the time interval is set, 3000 days after the start of the injection, and a location has be chosen to find the corresponding M_w .

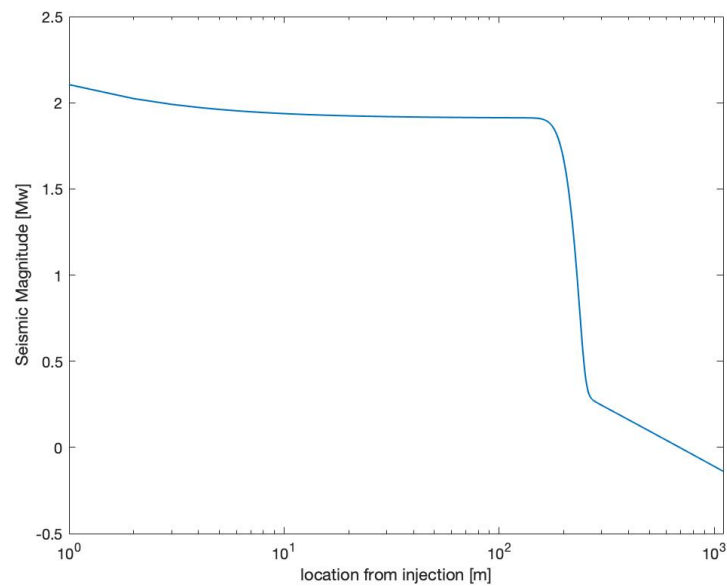


Figure 7-20. Plot of the maximum moment magnitude of a seismic event over distance from the injector after 3000 days of injection. This gives an indication of the maximum magnitude of one single event if the fault lies in the unstable zone of a Mohr plot.

The average slip of the rupture along the fault follows more or less the same pattern as the graphs of the moment magnitude over time and over location. Here it is also visible that the amount of slip takes a dive, when looking at the M_w over location (figure 7-20), and rises quickly, when looking at the M_w over time (figure 7-19), when the thermal front reached the location.

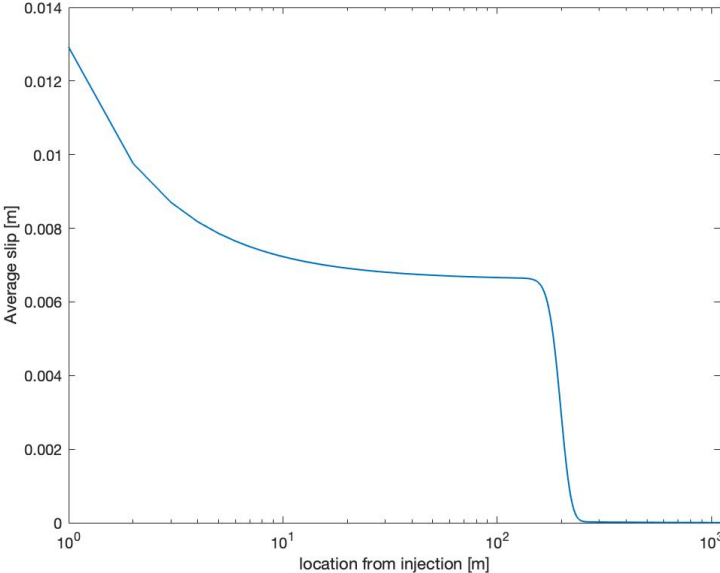


Figure 7-21. Plot of the maximum average slip of the whole fault of a seismic event over distance from the injector after 3000 days of injection. With the dimensions of the fault being 10 meters (width) by 2000 meter (length).

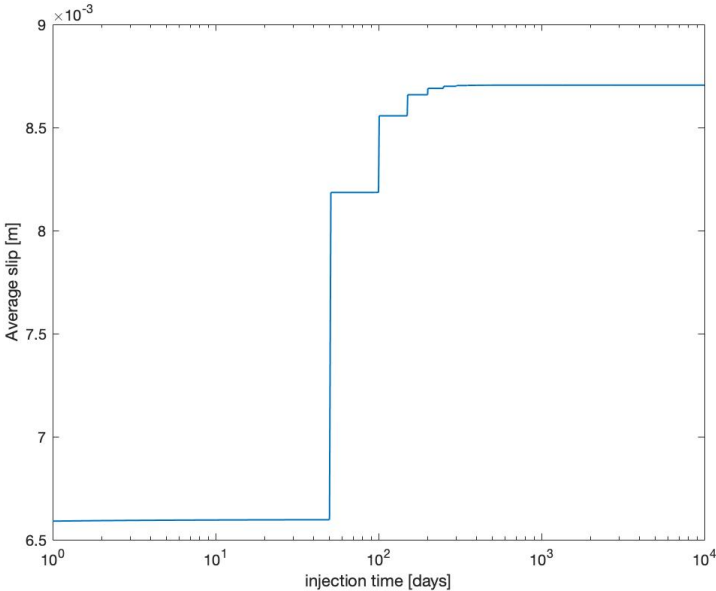


Figure 7-22. Plot of the maximum average slip of the whole fault of a seismic event over injection time at a 3-meter radius from the injector. With the dimensions of the fault being 10 meters (width) by 2000 meter (length).

7.5 PSM STEP 4: GROUND MOTION PREDICTION

The last step in the Physical Screening Model is the conversion to ground motion prediction. With this step the use of this model can be extended for the use in the SRA, the ground movement is an important parameters in a SRA. With the calculation of the ground movement, assumption and

calculations can be done with respect to the risk of damaging building or infrastructure that are on the surface close to a seismic event. From section 6.8 the most accurate and contemporary model is used, the model created by the NAM. The corresponding equations are as follows:

$$\ln(PGV) = c_1 + c_2 M_L + g(R) \quad [6.76]$$

$$\text{with } R = \text{distance term} = \sqrt{R_{epi}^2 + [\exp(0.4233M - 0.6083)]^2}.$$

For the distance the geometrical spreading term is segmented over three distances:

$$g(R) = c_4 \ln(R) \quad R \leq 6.32 \text{ km} \quad [6.77]$$

$$g(R) = c_4 \ln(6.32) + c_{4a} \ln\left(\frac{R}{6.32}\right) \quad 6.32 < R \leq 11.62 \text{ km} \quad [6.78]$$

$$g(R) = c_4 \ln(6.32) + c_{4a} \ln\left(\frac{11.62}{6.32}\right) + c_{4b} \ln\left(\frac{R}{11.62}\right) \quad R > 11.62 \text{ km} \quad [6.79].$$

7.5.1 RESULTS

The result of the peak ground velocity is defined over radial distance from the epicentre. It is depending on the moment magnitude found in the previous step and thus based on the time (3000 days), location (3m radius from injector), orientation (most critical) etc. of the fault and the parameters of the reservoir in general.

Figure 7-23 shows the PGV following the NAM calculations with the reservoir and operational parameters from the previous three PSM steps. The maximum magnitude was found to be 1.91, this line is visualized in figure 7-23. The PGV_{GM} (averaged) from Table 6-2 is used with a maximum distance of 15 kilometres from the epicentre.

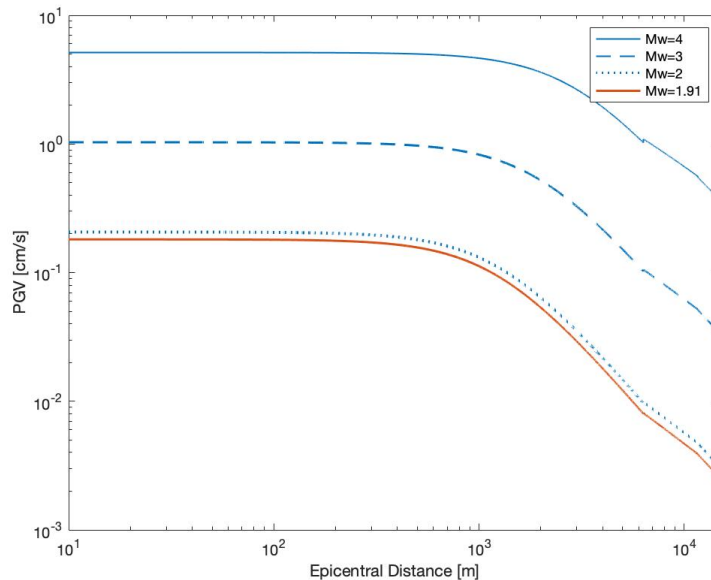


Figure 7-23. Predicted median PGV values against distance for four magnitudes, including the earlier found magnitude of 1.91.

From this figure it can be seen that the maximum PGV is relatively constant over a long distance. The PGV for $M_w=4$ it is around 5.14 cm/s, for $M_w=3$ around 1.03 cm/s and for $M_w=2$ around 0.21 cm/s. The M_w 1.91 is below the lowest indicator and its PGV is ± 0.18 cm/s. It is also noticeable that the

distance, over which this PGV is constant, becomes shorter when the moment magnitude is lower. With $M_w=4$ the fairly constant PGV hold until an epicentral distance of 1000 meters while with at $M_w=2$ the PGV already starts decreasing after 450 meters.

8. PHYSICAL SCREENING MODEL RESULT ANALYSIS

The results of the physical screening model, presented in the previous chapter, are at most instances one-dimensional; the impact of the whole model and all its features are occasionally difficult to visualize as only examples of certain situations could be displayed.

Thus, in order to provide additional information, this chapter will contain studies about the most dominating factors of the PSM. This additional information is given by performing following two types of analyses:

- Sensitivity analysis
- Two Case studies.

When these analyses are conducted the model can be easier interpreted and fitted better into the final SRA.

8.1 SENSITIVITY ANALYSIS

With a sensitivity analysis it is possible to study the uncertainty of an output of this model that is generated by the variety of the models input. Sensitivity analyses are used to determine the influence of one input parameters on the total output of the model. Ultimately it should be used to rank the input parameters in order of influence. For this case it will be used to see what operational or reservoir input parameter has the most influence on the total stress difference (visualized in a Mohr circle).

The input parameters that will be investigated are listed below:

- Permeability (k [m^2])
- Injection rate (V_{fi} [m^3/h])
- Injection temperature (T_{inj} [$^{\circ}C$])
- Elastic moduli (Poisson's ratio, ν [-], and Young's modulus, E [Pa]).

These four parameters are chosen because two, the permeability and the elastic moduli, are the most significant reservoir parameters. The Injection rate and the injection temperature are two operational parameters that can be influenced by the operator and thus its necessary to investigate what the influence of these two parameters is on the stress output.

8.1.1 PERMEABILITY

Permeability is an important factor in the reservoir production industry. The permeability is used in the investigation into the diffusion of pore pressure, poro-elastic stress and temperature through the reservoir, PSM Step 1 of the model (section 7.1 and 7.2). Changing the permeability of the reservoir in this model will have three mayor impacts on the system:

- The permeability, k , has a strong influence on the diffusivity, c , of the reservoir and therefore the diffusion of ΔP , $\Delta\sigma_{poro}$ and ΔT . The relation between k and c is given by:

$$c = \frac{k}{\eta S} \quad [8.1].$$

Where η is the fluid viscosity and S is the uniaxial specific storage (a rock characteristic). An increase in permeability will also increase the diffusivity. As diffusivity is the rate of diffusion and the speed at which particles can spread, pore pressure will be spread at a quicker rate while it will be of a lower difference at the same time and place, as Eq. 8.1 suggests.

- According to Darcy's law, a higher permeability will increase the flow velocity:

$$q = -\frac{k}{\mu} \Delta p \quad [8.2].$$

Where q is the flow velocity in m/s, μ is the dynamic viscosity and p is the pressure difference. A faster flow velocity q will increase the distribution of the injected cold water, thus according to Eq. 8.2 the reservoir will cool down quicker.

- With changing the permeability the porosity is also changed or vice versa. A lower permeability usually corresponds to a lower porosity, and with that comes less rock surface to transport the heat, or in this case the cold, from the injected fluid to the rock. Thus is the assumption that a lower permeability leads to a slower movement of the thermal front through the reservoir.

The permeabilities used in this sensitivity analysis are based on the range of average permeabilities found in the Delft sandstone in the subsurface of South-Holland, (see case study) [72]. In order to correctly analyse the results, five linearly compatible permeabilities are taken: 1 Darcy (D), 0.5D, 0.25D, 0.125D and 0.0625D.

RESULTS

The result of changing the permeability has a significant influence on the pore pressure change. As expected an increase in permeability will decrease the pore pressure difference. The permeability was divided by two every step, this linear relation can be seen in figure 8-1, where the pore pressure change is plotted over the distance from the injection well with the five different permeabilities. The same relationship is observed for both the $\Delta\sigma_{rad}$ and $\Delta\sigma_{tan}$, the plots can be found in Appendix F.

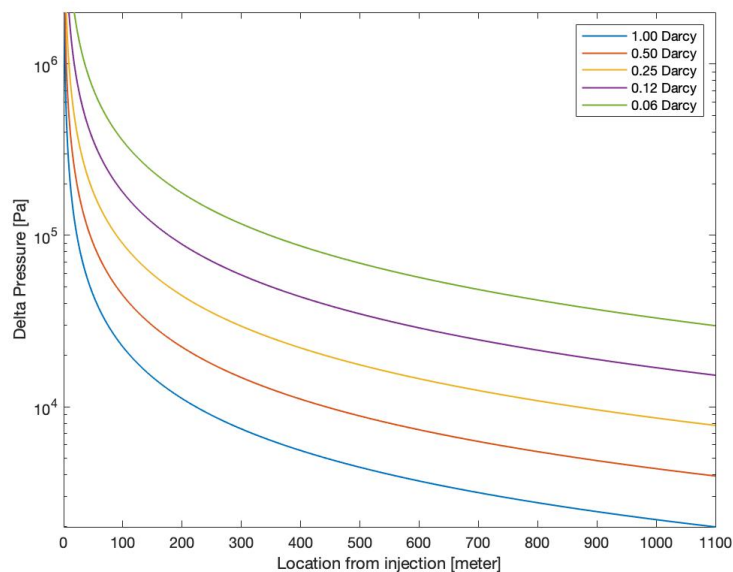


Figure 8-1. Plot of the ΔP over location from the injector after 1000 days with five different permeabilities.

The numerical difference between the ΔP is significant. After 1000 days of injection at 100-meter radius from the injection well the difference between the ΔP created by 1D and ΔP created by 0.06D is ± 2.6 bar, 15 times higher. Table 8-1 below shows all the ΔP corresponding with the five different permeabilities.

Table 8-1. The different Δp , $\Delta\sigma_{rad}$ and $\Delta\sigma_{tan}$ at a 100 meters radius from the injector after 1000 days of constant injection corresponding with the five different permeabilities.

Permeability [Darcy]	ΔP at 10 meters after 1000 days [Bar]	$\Delta\sigma_{rad}$ at 10 meters after 1000 days [Bar]	$\Delta\sigma_{tan}$ at 10 meters after 1000 days [Bar]
1	2.24	1.09	0.549
0.5	4.47	2.19	1.10
0.25	9.00	4.38	2.19
0.125	17.9	8.78	4.39
0.0625	35.8	17.6	8.77

The influence of the permeability on the temperature is less significant. It is assumed that as the flow velocity through the reservoir becomes smaller, the ΔT will diffuse slower. The average flow velocity over the whole systems does change due to the permeability alteration but this effect is lowered by a higher porosity creating less fluid-rock contact, and thus reducing the influence of permeability on the temperature diffusion. Figure shows only this small difference in ΔT over time and location. Table 8-2 shows that the difference is less significant.

Table 8-2. The different ΔT at a 500 meters radius from the injector after 10000 days of constant injection corresponding with the five different permeabilities.

Permeability [Darcy]	ΔT at 500 meters after 10000 days [C]
1	44.3
0.5	46.1
0.25	48.6
0.125	50.8
0.0625	53.5

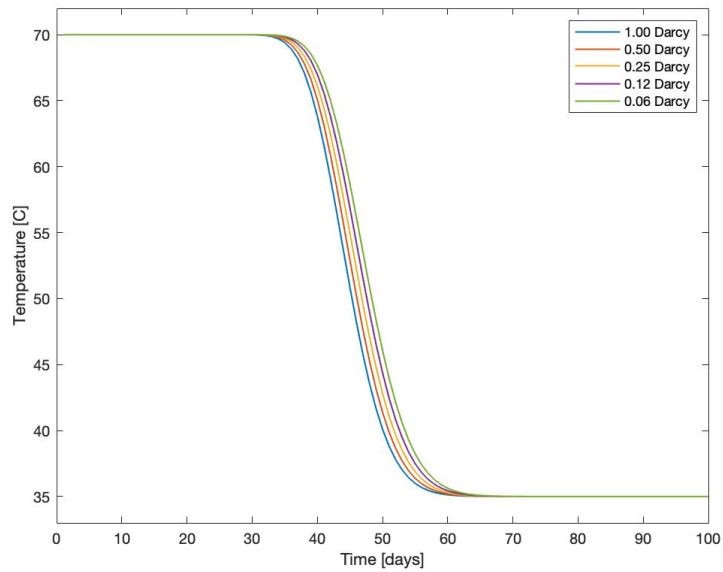


Figure 8-2. Plot of the thermal front over time at 150 meters from the injector with the five different permeabilities. The difference between the five different permeabilities is minimal.

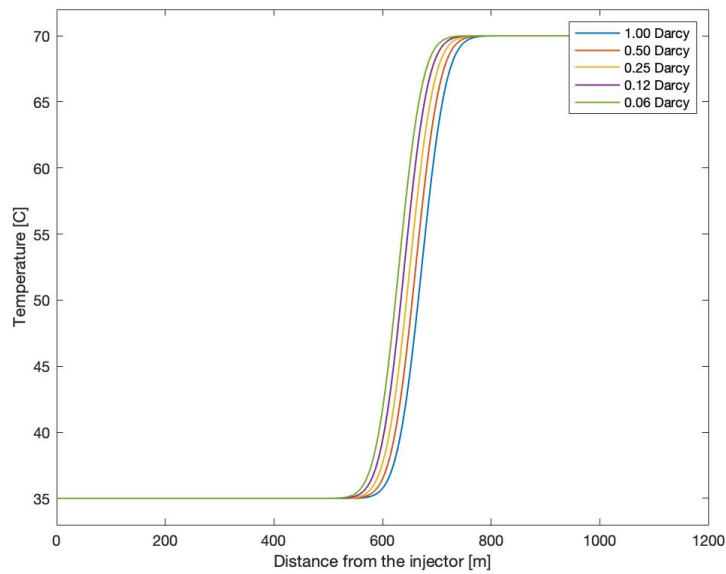


Figure 8-3. Plot of the thermal front over distance from the injector after 40 years of constant injection with the five different permeabilities. Similar to figure 8-2, the difference between the five different permeabilities is minimal.

Figure 8-4 gives an example of the different Mohr circles with different permeabilities. In all the five circles the thermal front has passed, thus making the thermoelastic stress decrease similar for all five permeabilities. Very noticeable is the difference in size between the Mohr circles, this is due to the influence of the poro-elastic stresses when the permeability is lower. Lower permeabilities implies lower porosities, this means more inter-granular contact, though which the poro-elastic stresses are diffused. As the poro-elastic stresses are easier and better diffused they tend to be higher compared to the relative lower direct pore pressure diffusion.

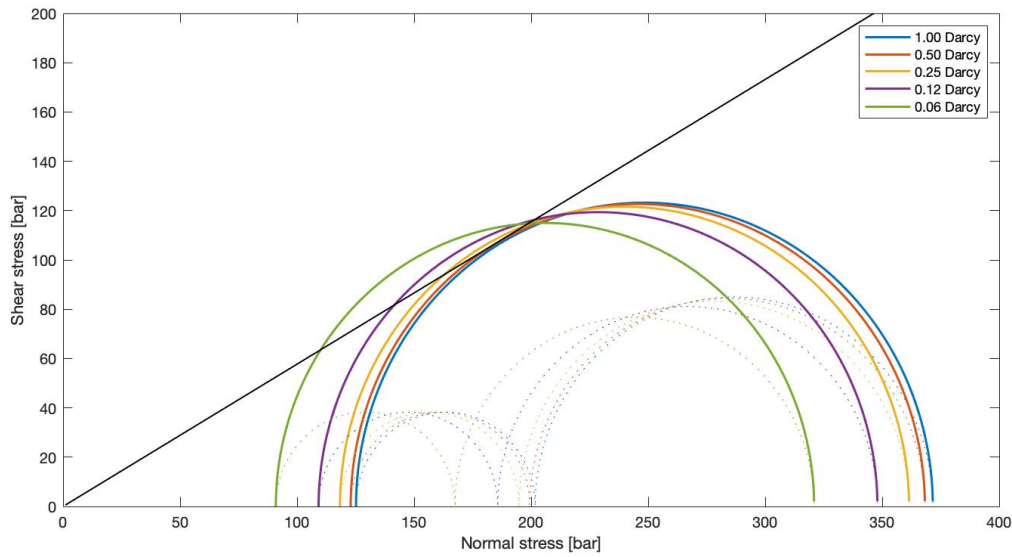


Figure 8-4. Mohr plot with five Mohr circle corresponding to the five different permeabilities. The Mohr circles are created at a 5 meter distance from the injector after 3000 days.

8.1.2 INJECTION RATE

The injection rate is an operational input parameter. It gives a volume per time of fluid that is injected into the reservoir. In the geothermal industry the most commonly used unit is cubic meter per hour, m^3/h . This notation is slightly different from the unit used in PSM Step 1, see section 7.1. In the equations from Rudnicki, used for diffusion calculation of ΔP and $\Delta\sigma_{\text{poro}}$, fluid mass per time, Φ [kg/s], is used. As Φ is divided by the fluid mass density, ρ_f [kg/m^3], this term can be summed up to injection rate, V_{fi} [m^3/s].

The equations for diffusion calculations of ΔT , from Ganguly and Kumar (2014) [24], make use of the flow velocity of water through the reservoir. This parameter is dependent on the injection rate but is not the same, as it is also strongly dependent on the pressure differences that stimulate the fluid flow, the conductivity and thus permeability of the reservoir. According to Darcy's law:

$$q = -\frac{k}{\mu} \nabla P \quad [8.2].$$

Where q is the flow velocity in m/s , k is the permeability, μ is the dynamic viscosity and p is the pressure difference. As the pressure gradient is a result of the injection and production pressure differences and is calculated with Rudnicki's equation, the flow velocity through the reservoir can be calculated. This makes q linearly related to pressure gradient and thus the injection rate (assuming the other parameters stay constant).

The influence of the injection rate depends on creating a pressure difference at the injector in order to stimulate fluid flow inside the reservoir between the wells. As Darcy's law (Eq. 8.2) suggests the injection rate therefore depends on the flow velocity of the water inside the reservoir. Lowering the injection rate lowers the flow velocity and thus the hot water production. Additionally, the pressure difference directly creates the $\Delta\sigma_{\text{poro}}$, which then is diffused through the matrix of the reservoir. Lowering the injection rate leads to a lower pressure difference and thus lowers the ΔP and $\Delta\sigma_{\text{poro}}$ at the injector and consequently at the whole reservoir, which then is leading to less in situ stress changes and a smaller seismic risk. The opposite is expected when increasing the injection rate.

For this sensitivity analysis the following injection rates are used: 100, 200, 300, 400 and 500 m³/h. These numbers fall in the range of the currently used injection rate in the industry.

RESULTS

As expected both the ΔP and the $\Delta\sigma_{\text{poro}}$ increase with an increase of the injection rate. Figure 8-5 (and both figure A-9 and A-10 in the Appendix G) show the increasing ΔP and $\Delta\sigma_{\text{poro}}$ with a higher injection rate. The injection rate was increased linearly and this subsequently results in a linear rise of ΔP , this is also shown in Table 8-3. This linear relation between injection rate and ΔP was expected regarding Rudnicki's equation.

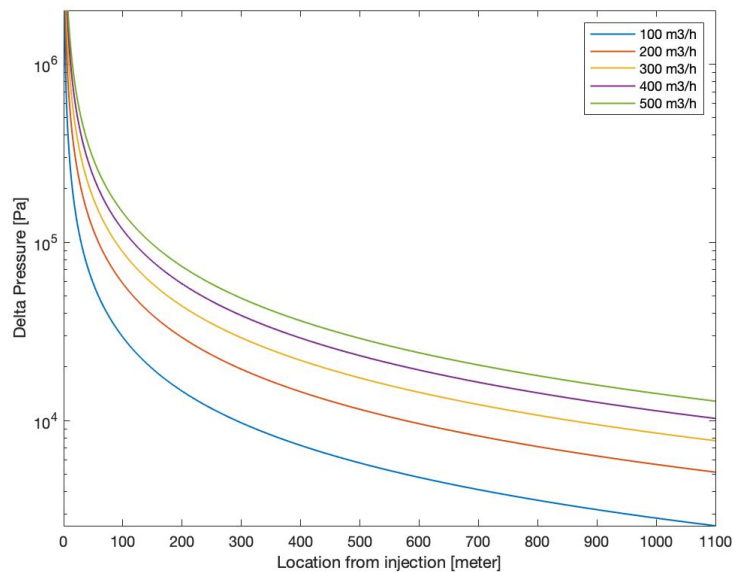


Figure 8-5. Plot of the ΔP over location from the injector after 1000 days of injection with five different injection rates.

Table 8-3. The different Δp , $\Delta\sigma_{\text{rad}}$ and $\Delta\sigma_{\text{tan}}$ at a 5-meters and 50-meter radius from the injector after 1000 days of constant injection corresponding with the five different injection rates.

Injection rate [m ³ /h]	ΔP at 10 meters after 1000 days [Bar]	ΔP at 50 meters after 1000 days [Bar]	$\Delta\sigma_{\text{rad}}$ at 5 meters after 1000 days [Bar]	$\Delta\sigma_{\text{tan}}$ at 5 meters after 1000 days [Bar]
100	2.95	0.588	1.44	0.722
200	5.89	1.18	2.89	1.44
300	8.84	1.77	4.33	2.17
400	11.8	2.35	5.78	2.89
500	14.7	2.94	7.21	3.86

The injection rate has a significant influence on the average flow velocity. Figure 8-6 and 8-7 show the result of this influence. From the second figure it can be seen that with a decreasing injection rate the thermal front elongates. Increasing the injection rate causes the thermal front to travel faster through the reservoir in general, but it also significantly extends the time it takes for the temperature of the reservoir to completely cool down. At an injection rate of 500 m³/h it takes 600 days after the thermal front arrives for the reservoir to completely cool down, while with a rate of 100 m³/h this takes more than 6000 days.

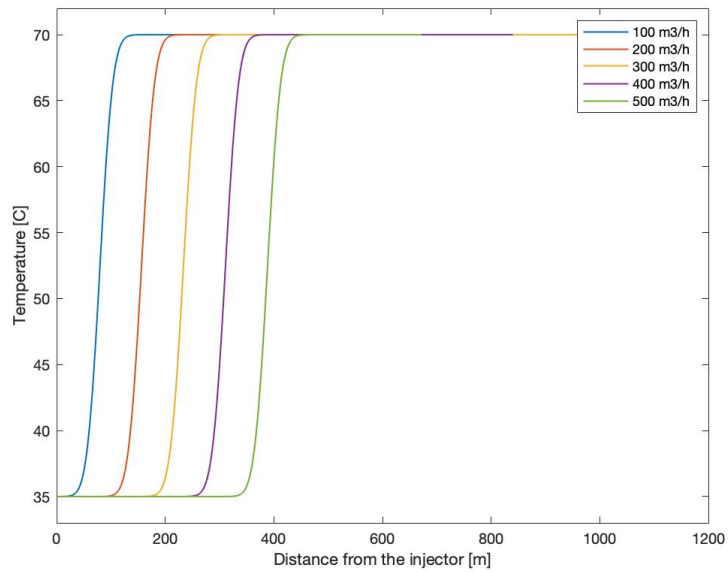


Figure 8-6. Plot of the thermal front over distance from the injector after 3000 days of constant injection with the five different injection rates. Increasing the injection rate significantly increases the velocity of the thermal front through the reservoir.

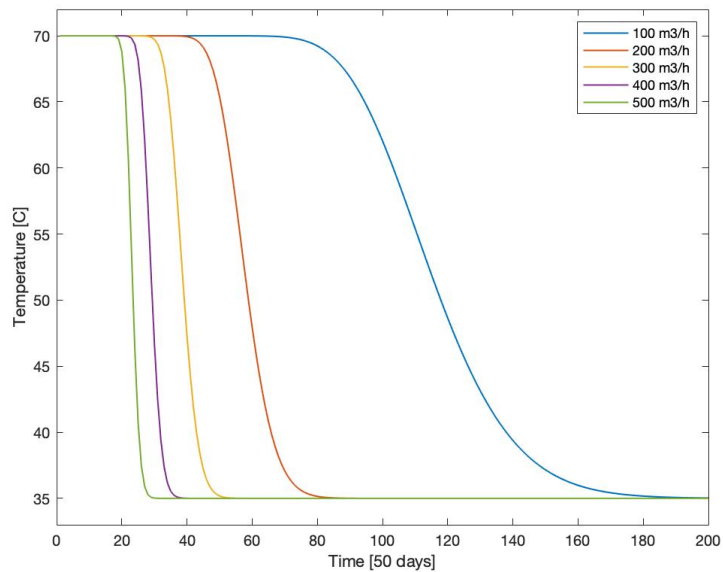


Figure 8-7. Plot of the thermal front over time at 150 meters from the injector with the five different injection rates. Not only is the overall velocity of the thermal front significantly influenced but this front velocity increase also extends the time for the reservoir to completely cool down.

The Mohr circles shown in figure 8-8 are taken at a 5-meter radius after 1000 days. As the thermal front has already completely passed and thus making the thermoelastic stress decrease similar for all the five injection rates, the difference between the five Mohr circles is fairly linear, in agreement with the linear relation observed with Rudnicki's equations.

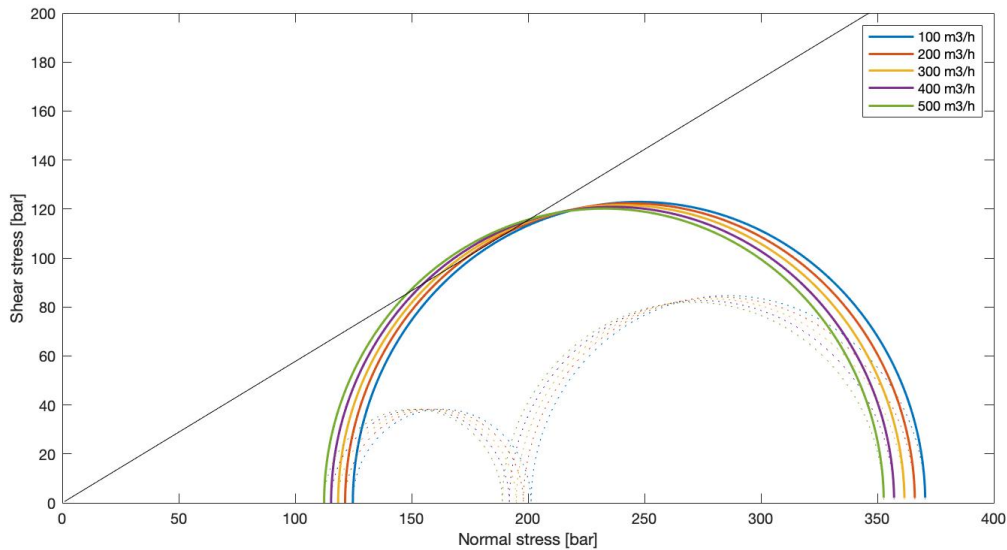


Figure 8-8. Mohr plot with five Mohr circle corresponding to the five different injection rates. The Mohr circles are created at a 5 meter distance from the injector after 1000 days. As the thermal front has already passed at this moment, the difference between the 5 circles originates only from the pressure differences.

8.1.3 INJECTION TEMPERATURE

The injection temperature is another operational parameter that can be changed by the operator. The cooled injected water is normally around 20-50 °C in hydrothermal systems [44].

Changing the injection temperature of the water does not influence the diffusion of pore pressure or poro-elastic stress through the system, because the injection rate and flow velocity is not altered by a change of water temperature. For the same reason it has no influence on the diffusion of the temperature through the reservoir. One could argue that colder or warmer water has a lower or higher density and thus changes the injection pressure and fluid flow velocity with the same injection rate. This small effect will be neglected in this sensitivity analysis. Another could argue that difference in injection temperature will extend or reduce the thermal fronts length, but this process is seen to be small and has eventually little effect on the thermal stress reduction.

Modifying the injection temperature, however, does influence the magnitude of the thermoelastic stress changes as it is dependent on the difference in temperature, ΔT , before and after injection, see Eq. 6.59 in section 6.6. As the equation shows, there is a linear relationship between the thermoelastic stress changes and the difference in water temperature. The expectation is that this relation between ΔT and the total stress drop, and thus the moment magnitude, will likewise be linear.

There are four different injection temperatures chosen for the sensitivity analysis: 20°C, 30°C, 40°C, and 50 °C.

RESULTS

Adjusting the injection temperature has predictable influence on the stress alterations. Changing the water temperature of the injected fluid does not alter the diffusion scheme of the ΔP , $\Delta\sigma_{\text{poro}}$ or ΔT over location and time. Figure 8-9 and 8-10 shows that even the path of the spatio-temporal evolution of temperature change is not significantly different between 20°C and 50°C. However, it takes about an extra 250 days for the reservoir to cool completely down to 20°C instead of only 50°C.

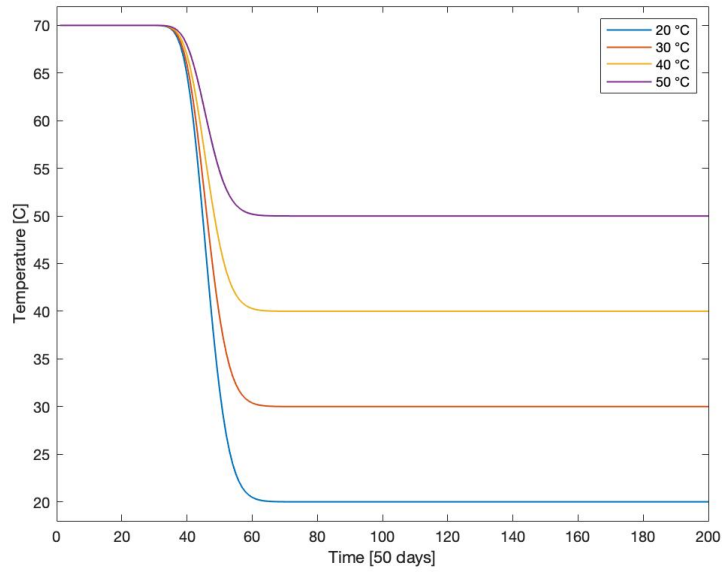


Figure 8-9. Plot of the thermal front over time at 150 meters from the injector with the four different injection temperatures; 20, 30, 40 and 50 °C.

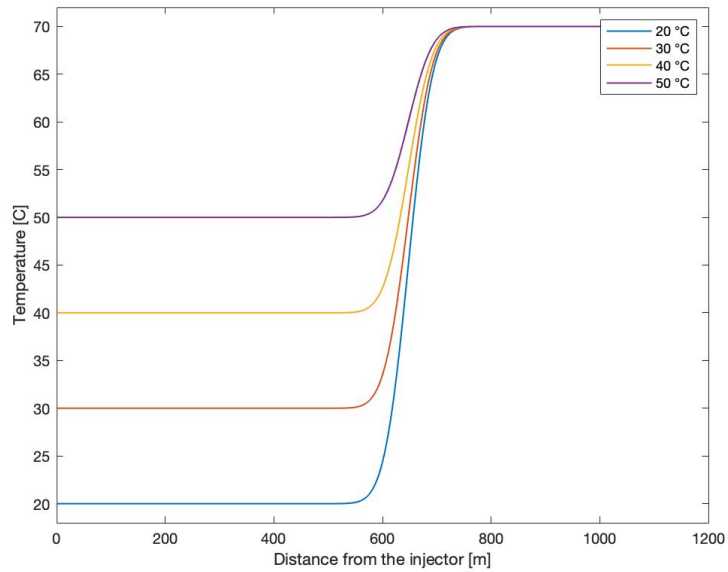


Figure 8-10. Plot of the thermal front over distance from the injector after 40 years of constant injection with the four different injection temperatures; 20, 30, 40 and 50 °C.

Changing the injection temperature does however substantially change the $\Delta\sigma_T$ due to the thermal front being colder or warmer. The Mohr circles in figure 8-11 show that a fault at a 10-meter radius is far more likely to be reactivated when injecting with 20°C fluids as opposed to 50°C or even 40°C fluids.

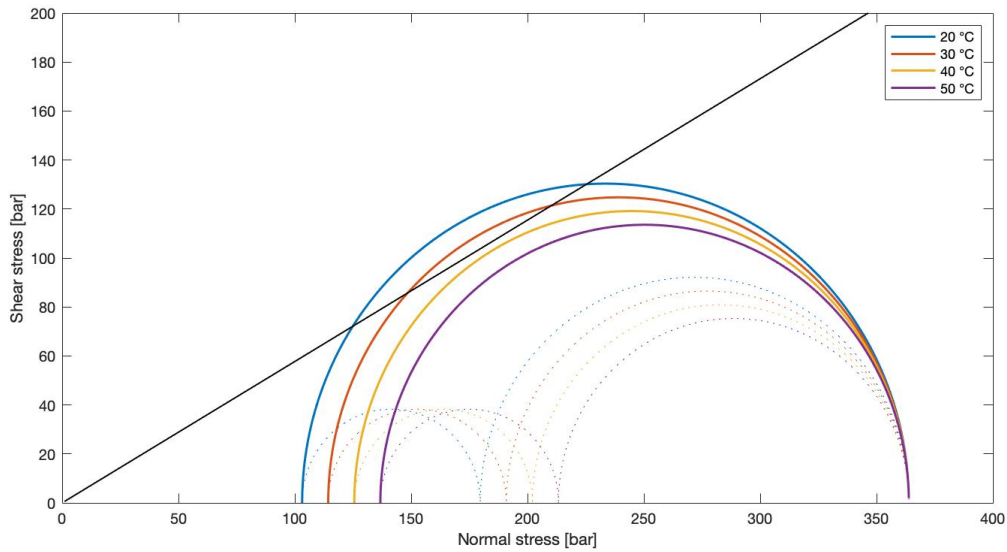


Figure 8-11. Mohr plot with five Mohr circle corresponding to the five different injection temperatures. The Mohr circles are created at a 10-meter radius from the injector after 300 days.

8.1.4 ELASTIC MODULI

Most of the geothermal projects in the Netherlands are operated in sandstone aquifers, but also limestone is used as a geothermal reservoir, for example in Limburg. Different reservoir types have different reservoir parameters, like for instance permeability. When investigating the diffusion through a reservoir and the seismic reaction of faults in a reservoir on changing in situ stresses, the elastic modulus of the rock is essential.

An elastic modulus is a quantity that measures an object or substance's resistance to being deformed elastically when a stress is applied to it. There are 6 different elastic moduli. Three primary ones are: Young's modulus (E), the shear modulus (G or μ) and the bulk modulus (K). The three other elastic moduli are: Poisson's ratio (ν), Lamé's parameter (λ) and P-wave modulus. The general form of an elastic modulus is that of stress divided by strain. In chapter 6 these moduli can be found throughout the sections in various equations.

As homogeneous isotropic material, or reservoir rock in this case, have their elastic properties fully described by just two randomly chosen elastic moduli, only two different elastic moduli are needed to investigate the sensitivity of the elastic modulus of the rock. To give this sensibility study a more interesting angle in terms of usability, the elastic modulus of four different rock types are compared. In Table 8-4 the typical Poisson's ratio and Young's modulus for sandstone, shale, limestone and granite are given.

Table 8-4. General ranges and for the this sensitivity analysis chosen Poisson's ratios and Young's Modulus of sandstone, shale, limestone and granite.

Elastic modulus	Sandstone (SST)		Shale (SHL)		Limestone (LST)		Granite (GNT)	
	Range	Chosen	Range	Chosen	Range	Chosen	Range	Chosen
Poisson's ratio (ν) [-]	0.21-0.38	0.25	0.2-0.4	0.28	0.18-0.33	0.24	0.1-0.3	0.18
Young's Mod (E) [GPa]	1-20	13	1-70	15	15-55	35	10-70	40

Different elastic moduli of the reservoir rock will have some effect on the diffusion of both ΔP and $\Delta\sigma_{\text{poro}}$, according to Rudnicki, but this is assumed to be minimal, especially between the four rock types. The $\Delta\sigma_T$ created by ΔT , according to Eq. 6.59 in section 6.6, will be more influential.

In a second part of this sensitivity analysis for elastic moduli, only the Young's modulus will be changed while the other elastic modulus, i.e. Poisson's ratio, will remain the same. Young's modulus (and Poisson's ratio) is the most commonly used of all the elastic moduli in (geothermal) operations. Changing it will have some influence on the diffusion of ΔP and $\Delta\sigma_{\text{poro}}$, but will mainly and directly investigate its thermoelastic stress change. The four different Young's moduli taken are 10, 20, 30 and 40 MPa.

RESULTS

The result of the four different rock types, according to their different elastic moduli, is minimal in the first few hundred-meter radius after 1 day, see figure 8-12. There is little alteration in pore pressure distribution; only far from the injector the differences become clear. Sandstone is the worst performing diffusive material, the other three are very close to one another. After 1000 days the differences between the four rock types is completely diminished, see figure A-11 in Appendix H. $\Delta\sigma_{\text{poro}}$ in both the tangential and radial direction, continues to be slightly different for the four rock types, even after 1000 days of injection, see Appendix H. ΔT shows equal result as ΔP , where there is no difference between the diffusion patterns after sufficient time, see Appendix H.

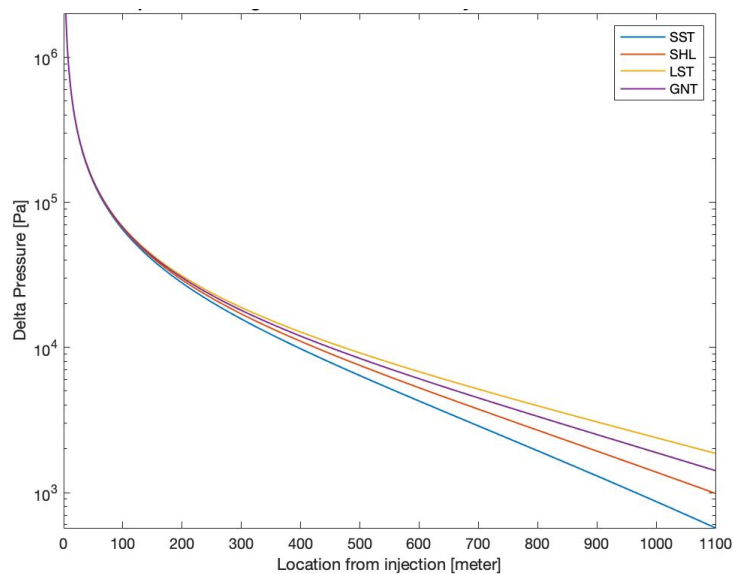


Figure 8-12. Plot of the ΔP over location from the injector after 1000 days with four different rock types.

$\Delta\sigma_T$ is affected considerably, see figure 8-13. This is due to the different bulk moduli that are used to calculate $\Delta\sigma_T$ via Eq. 6.59. As the bulk modulus is almost twice as big for limestone and granite $\Delta\sigma_T$ also becomes twice as big, see Table 8-5. Note that the bulk modulus is not the only factor changing $\Delta\sigma_T$. $\Delta\sigma_T$ of granite is larger than that of the limestone; this is due to the indefinitely different $\Delta\sigma_{\text{poro}}$ for the four rock types while ΔP is the same (see Appendix H).

Table 8-5. The four different bulk moduli of sandstone, shale, limestone and granite that correspond with the maximal thermal stress decrease, $\Delta\sigma_{T,max}$.

Rock type	Bulk Modulus [MPa]	$\Delta\sigma_{T,max}$ [Bar]
Sandstone	8.67	30.3
Shale	11.63	36.5
Limestone	22.44	80.6
Granite	20.83	85.4

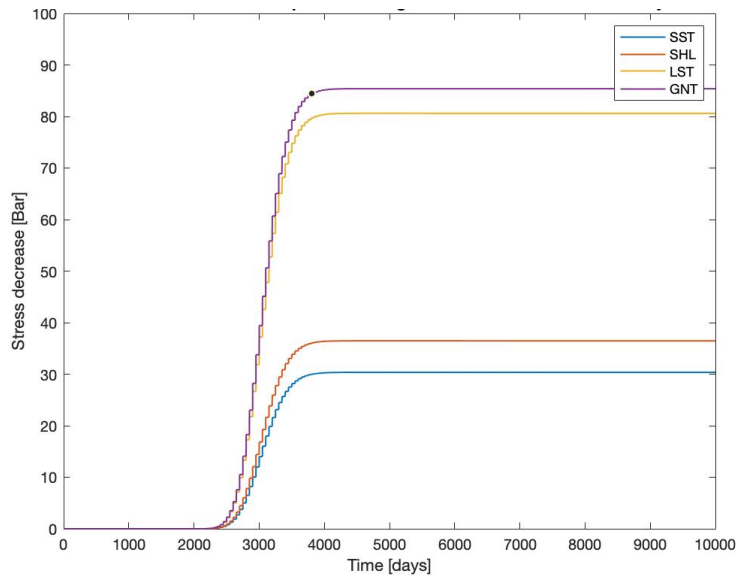


Figure 8-13. Plot of the $\Delta\sigma_T$ over time at 200 meters from the injection point. There is a distinct difference between limestone/granite and sandstone/shale.

The change in elastic moduli eventually results in a large difference between the different rock types when looking at the corresponding Mohr circles. While both the sandstone and the shale are considerable stable a certain injection time and fault location as can be seen in figure 8-14, this does not hold for granite or limestone. This is primarily due to the sizeable differences in $\Delta\sigma_T$.

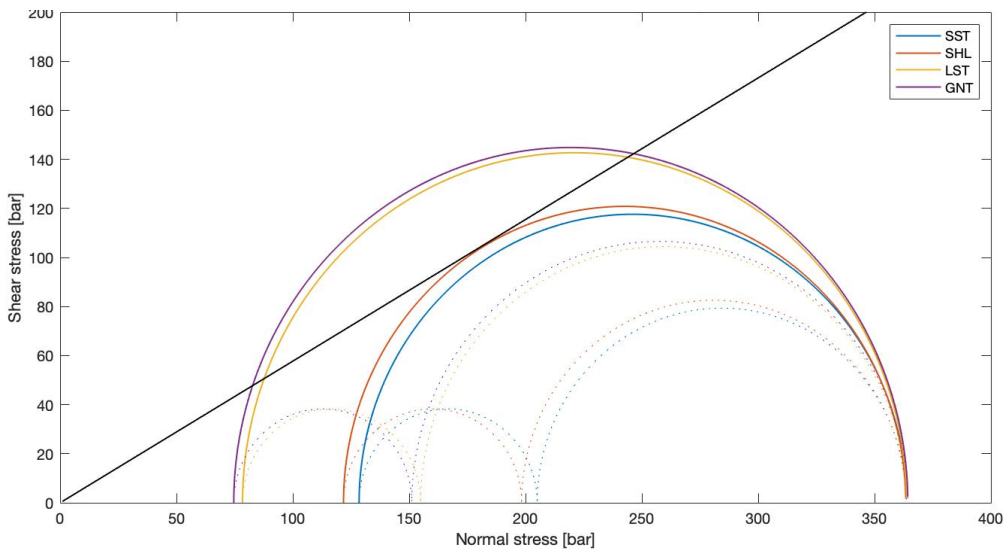


Figure 8-14. Mohr plot with four Mohr circle corresponding to the four rock types. The Mohr circles are created at a 5-meter radius from the injector after 1000 days.

For the second part of this sensitivity analysis of elastic moduli, when only looking at the relation between the Young's modulus and its results on the Mohr circle, it can be seen that this relation is linear. This is shown in figure 8-15 below, where the Mohr circles of the four different Young's moduli are displayed, while all the other parameters remained unchanged.

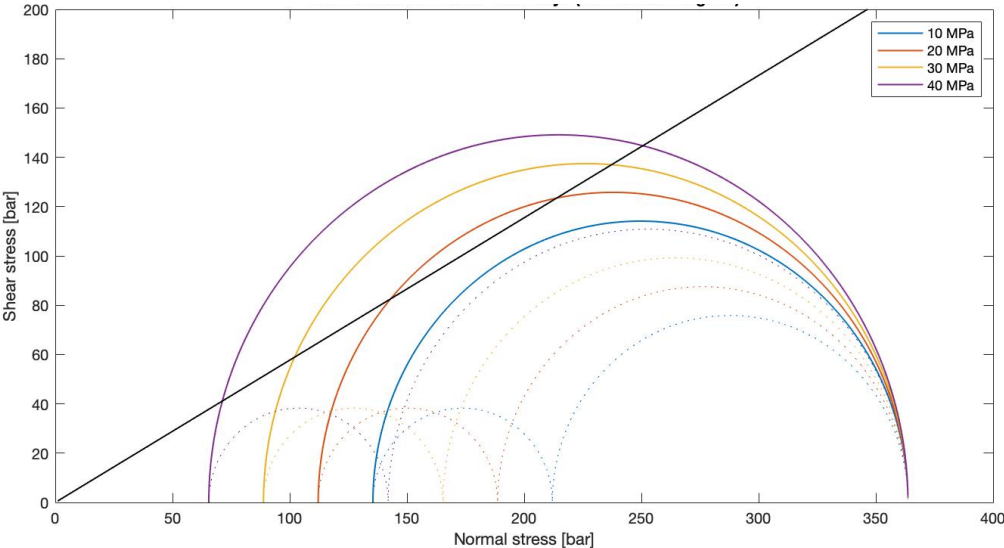


Figure 8-15. Mohr plot with four Mohr circles corresponding to the four different Young's moduli. The Mohr circles are created at a 5-meter radius from the injector after 1000 days.

8.2 SRA CASE STUDY: DAP PROJECT

Performing case studies will show how SRA Step 1A and B (of the new SRA approach) will perform in specific situations. This case study follows the reservoir and operational parameters of the future DAP project; a geothermal project to be developed at the TU Delft campus [61].

SRA STEP 1A

First Step 1A, the Physical Screening Model, is performed with the parameters displayed in Table 8-6, where also the default parameters used in chapter 7 are shown. The faults found in the area are the result of extensional faulting in the Late Jurassic, creating half-graben structures. The faults are between southeast to northwest trending [72]. These faults were active during and after deposition, and are assumed to lie at least at a 100m (about 500m should be the right distance) radius from the point of injection.

Table 8-6. The different parameters used for the DAP case study with respect to the default mode, used in chapter 7.

	Default mode	DAP project
Permeability reservoir	0.3 Darcy	0.6 Darcy
Biot-Willis coefficient	0.7	0.75
Shear modulus	8.4 GPa	5 GPa
Lame (drained) parameter	8.4 GPa	4 GPa
Lame parameter (undrained)	11.2 GPa	5.3 GPa
Poisson ratio	0.25	0.25
Young modulus	21 GPa	10 GPa
Bulk modulus	14 GPa	7.3 GPa
Fluid density	1000 kg/m ³	1000 kg/m ³
Volumetric flow rate	200 m ³ /h	380 m ³ /h
Depth Reservoir	3000 m	2100
Temperature reservoir	70 °C	77 °C
Temperature injection water	35 °C	35 °C
Lithostatic gradient	0.225	0.213
Hydrostatic gradient	0.106	0.106
Minimal horizontal gradient	0.16	0.165

Performing PSM Step 1 of the Physical Screening Model reveals that in the DAP project case the direct pore pressure and the poro-elasticity are essentially a non-factor past a 50-meter radius of the injector. Due to the relative high volumetric injection rate the injection pressure is rather high in the first meters but because permeability is good this decreases at a very strong rate. The direct pore pressure is essentially neglectable past ± 50 meter radius of the injector, dropping below 1 bar. See figure A-16 for this graph in the Appendix I.

The temperature difference between the injection water and the reservoir, however, is significant over the whole reservoir as soon as the thermal front arrives, leading to a large decrease in stress when the rock is cooled down. Figure 8-16 displays the Mohr circle at 1 meter from the injector after 3000 days, showing the difference between the Mohr circle with and without the inclusion of poro-elastic coupling and thermoelastic coupling. In figure 8-16 the Mohr circles at 1 meter from the injector shows that the water injections does not have a strong enough influence close to the injector.

Thus it can be seen that even a fault with the critical orientation at 1 meter from the injector can not be set into unstable conditions, as the Mohr circle clearly does not cross the Mohr-Coulomb criterion. Knowing from existing subsurface data that faults in this particular reservoir can be found from at least a 100 meters distance from the injector location, figure 8-16 shows that the fault region is still stable and will not be subject to potential slip. Thus, concluding that the Mohr circle in SRA Step 1A (Physical Screening Model) is stable, with the biggest influence being the relative high temperature difference between the injection water and the reservoir water.

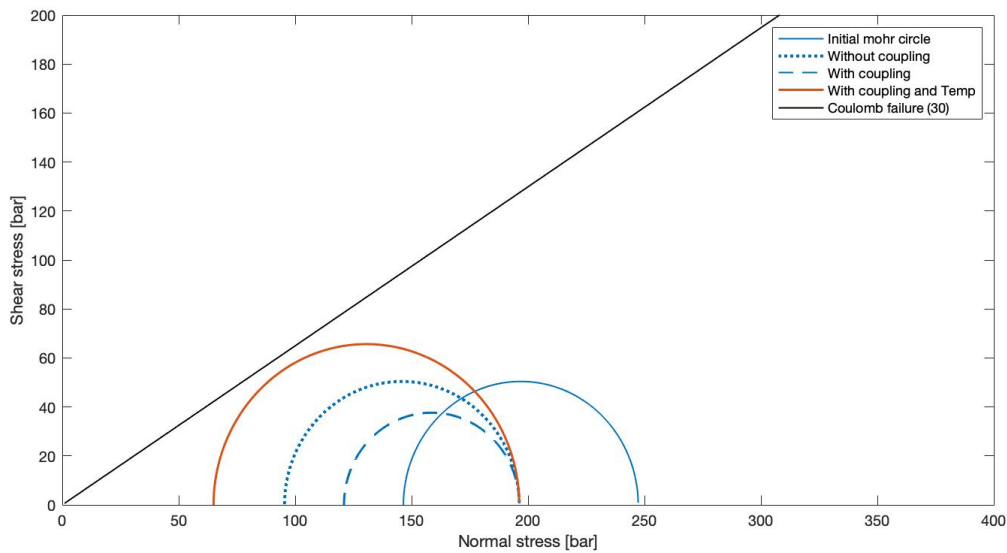


Figure 8-16. Mohr plot for the DAP project case. This Mohr circle should be taken in case a fault lies at a 1-meter radius from the injection point.

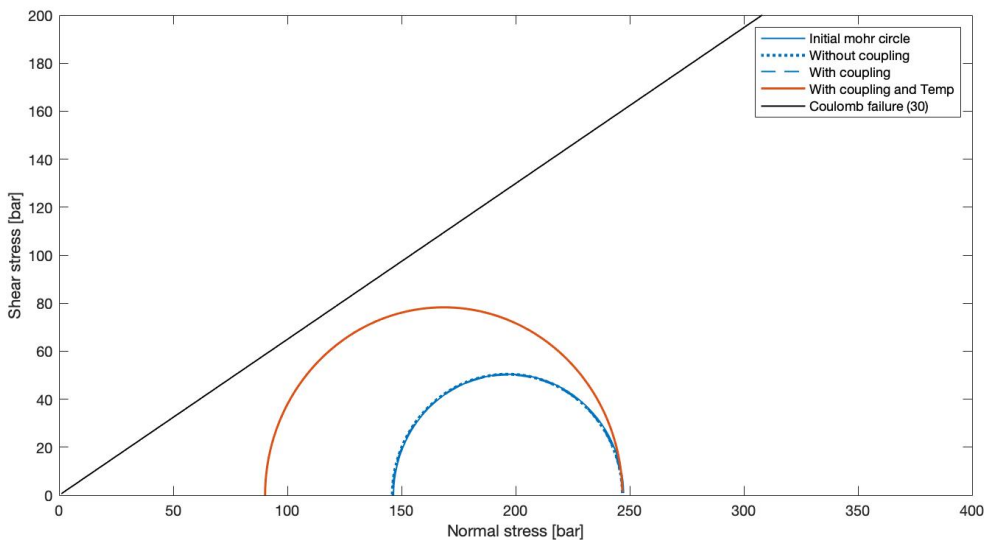


Figure 8-17. Mohr plot for the DAP project case. This Mohr circle should be taken in case a fault lies at a 100-meter radius from the injection point.

A main contributor to the stable conditions at the potential fault location in figure 8-16 and 8-17, apart from the earlier discussed input parameters in section 8.1, are the location specific calculated lithostatic and minimal horizontal gradients. Research into the subsurface of the DAP project by Pantera provided these numbers. The contribution of the changes in the gradients significantly

influenced the stability of the faults positively. In Appendix I the figures of the Pantera study for this locations are shown.

After constructing the Mohr circles (PSM step 1-2) the Moment Magnitude, M_w , (PSM step 3) and the Peak Ground Velocity, PGV can be calculated. These calculations are purely hypothetical as no sliding or failing of faults is expected. Assuming the fault dimensions are 10m by 1000m the maximum Moment Magnitude at 1m from the injector would be 1.92 and at 100m would be 1.81. This means that the Peak Ground Velocity at 1m from the injector would be 0.18 cm/s and at 100m would be 0.15 cm/s.

SRA STEP 1B

SRA Step 1B should also be evaluated for the DAP project case study. Table 8-7 is filled in with the information from the DAP project. Normalizing the added scores from the five parameters corresponds to 0.06, which is far below the 0.33 that is needed to fail this step. Thus this part of SRA Step 1 is completed successfully.

Table 8-7. The filled in Quick-Scan table of SRA Step 1b with data from the DAP project.

Score	Basement connection	Inter-well pressure communication	Epicentral distance to natural earthquakes [KM]	Epicentral distance to induced seismicity [KM]	Net injected fluid [1000 m ³]
10	Yes	No	< 1	< 1	> 20
7	Possible	Unlikely	1 – 5	1 – 5	5 – 20
3	Unlikely	Likely	5 – 10	5 – 10	0.1 – 5
0	No	Yes	> 10	> 10	< 0.1

As both SRA Step 1A and 1B are successful according to the new SRA (figure 5-1), only step 3 Monitoring I will need to be done.

8.3 SRA CASE STUDY: EXTREME CASE

The DAP case resulted in a successful completion of the SRA Step 1 (A&B), concluding that only Monitoring level I will be required. In order to illustrate what result is expected when the reservoir and operational parameters are not that favourable, this section presents a more extreme case, in which less favourable input parameters are chosen.

For SRA Step 1A (the PSM) the most influential parameters are changed such that eventually faults at 100 meters from the injector will still be in an unstable stress environment. The permeability is lowered from 0.6 to 0.1 Darcy; this will influence the pressure, stress and temperature distribution. The injection rate is increased with an extra 120 m³/h to 500 m³/h; this will also influence the pressure, stress and temperature distribution, especially close to the injector. Changes in the elastic moduli and injection temperature will have the biggest influence on the thermoelastic stress change. Table 8-6 shows the parameters used in this extreme case.

Table 8-6. The different parameters used for the Extreme case study with respect to the DAP project case study and default mode, used in chapter 7.

	Default mode	DAP project	Extreme case
Permeability reservoir	0.3 Darcy	0.6 Darcy	0.1 Darcy
Biot-Willis coefficient	0.7	0.75	0.75
Shear modulus	8.4 GPa	5 GPa	7 GPa
Lame (drained) parameter	8.4 GPa	4 GPa	6 GPa
Lame parameter (undrained)	11.2 GPa	5.3 GPa	7.98 GPa
Poisson ratio	0.25	0.25	0.25
Young modulus	21 GPa	10 GPa	15 GPa
Bulk modulus	14 GPa	7.3 GPa	10 GPa
Fluid density	1000 kg/m ³	1000 kg/m ³	1000 kg/m ³
Volumetric flow rate	200 m ³ /h	380 m ³ /h	500 m ³ /h
Depth Reservoir	3000 m	2100	2100
Temperature reservoir	70 °C	77 °C	77 °C
Temperature injection water	30 °C	35 °C	25 °C

Following the steps in the Physical Screening Model, the Mohr circles found at 3m from the injector and 100 meters from the injector can be seen in the figures below, 8-18 and 8-19.

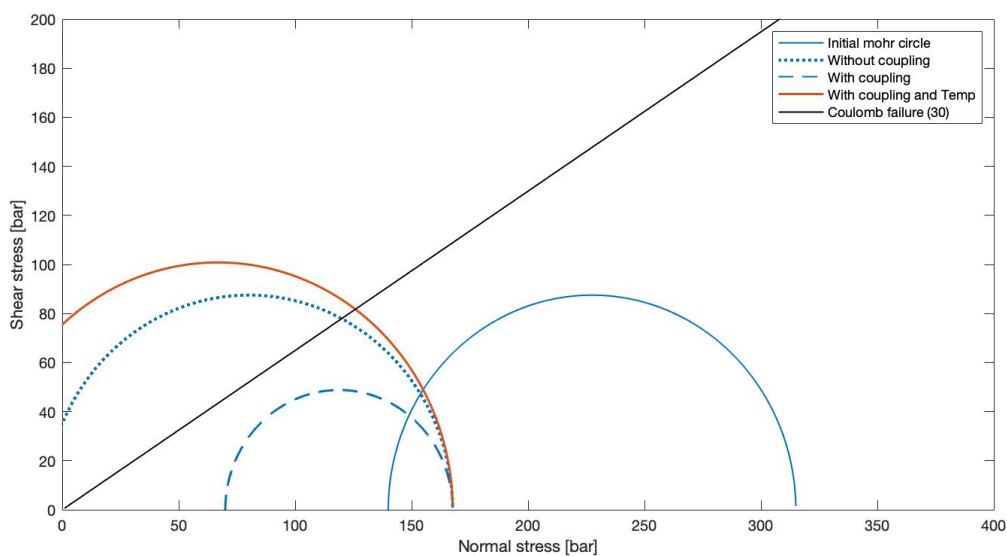


Figure 8-18. Mohr plot for the Extreme case. This Mohr circle should be taken in case a fault lies at a 3-meter radius from the injection point.

In figure 8-18 the results from a 3-meter distance from the injector are shown. Moving even closer to the injection point the stress situations will get worse and the fault plane will be even more unstable. At a 100 meter radius from the injector the effect of the ΔP and $\Delta\sigma_{poro}$ are diminished but due to the low injection temperature and high Bulk modulus the effect of thermo-elasticity is still resulting in an unstable stress situation. Assuming the orientation of the fault lies between a 49.8 and 73.1 angle with the smallest horizontal stress (σ_3), see figure 8-19 for an indication, the fault is unstable and seismic slip can be expected.

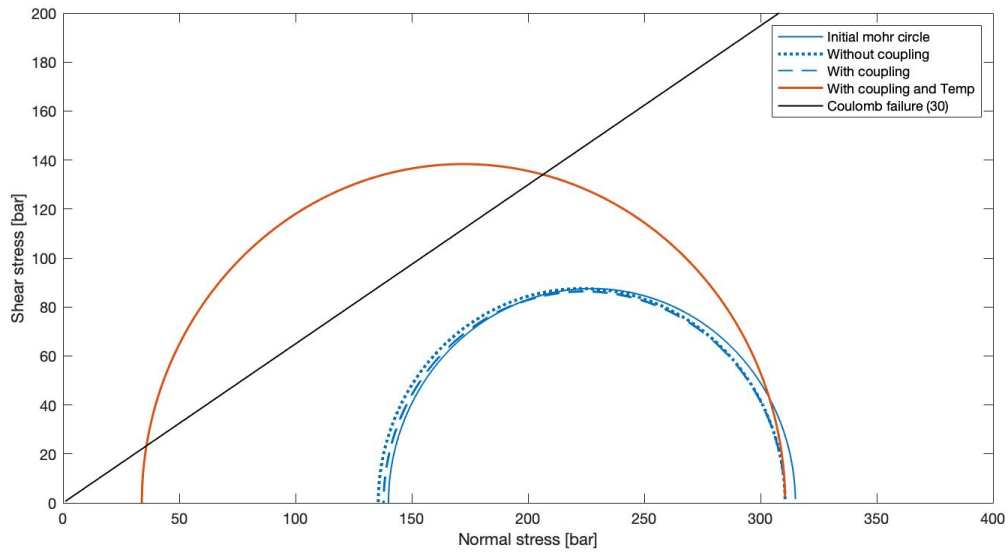


Figure 8-19. Mohr plot for the Extreme case. This Mohr circle should be taken in case a fault lies at a 100-meter radius from the injection point.

When slip does appear the maximum Moment Magnitude, M_w , (PSM step 3) and the Peak Ground Velocity, PGV can be calculated. Also in this extreme case study the fault dimensions are assumed to be 10m by 1000m. The maximum Moment Magnitude at 1m from the injector is 2.31 and at 100m it is 2.0. This means that the Peak Ground Velocity at 1m from the injector is 0.34 cm/s and at 100m it is 0.21 cm/s.

These figures show that the faults in the geothermal reservoir could be unstable after production has started and this could result in seismic slip. SRA Step 1A (the PSM) show that the faults in reservoir could be unstable and thus more investigation remains to be done before the operation can start.

9. DISCUSSION

Trying to predict and quantify seismic hazards during geothermal operations is not a simple task. Creating a new SRA that only eliminates the projects with too much hazard and let the safe ones carry on, is an equally difficult assignment. The new SRA, that includes the Physical Screening Model, needs to be accurate, but also quick and simple. In order to respect these requirements certain assumptions have been made.

The many assumptions in the Physical Screening Model can create some discussion in using it for the evaluation of seismic risk in geothermal reservoirs. It is important to mention that most of the assumptions actually overestimate the seismic hazard. Although there is one major assumption that can untimely have a negative influence on the prediction of seismicity. This assumption is that the faults in the reservoir are not sealing, this means that the faults are open and flow is possible along or through the fault. When a fault is sealing there can be a pressure build-up due to the water injection, which can ultimately lead to failure and seismicity.

Another significant assumption is the homogeneity of the reservoir. Introducing heterogeneity, which provides a more realistic picture of a reservoir, will lead to many different outcomes for the distribution of ΔP , $\Delta\sigma_{\text{poro}}$ and ΔT . This can either promote or depress the seismic hazard. The influence of a certain heterogeneous characters of the reservoir is to be determined for this model. When SRA step 1 of the new SRA is failed the next step will include modelling a specific heterogeneity into the reservoir depending on its parameters and depositional history.

An additional point for discussion is the linear superposition of the stress alterations due to pressure and temperature change. Normally when only regarding the thermal elastic behaviour of the rock Eq. 6.59 would satisfy, but as it is challenging to separate the relative influence of the pore pressure alteration and temperature effects on seismicity this will most likely not be sufficient. Therefore, there can be an over-and/or-underestimation in determining the total stress change with the linear superposition of stress increase or decrease due to direct pore pressure, poro-elasticity and thermo-elasticity [10]. These three processes should be fully coupled in this case as much as can be. For example when cold water is injected into a geothermal reservoir, resulting in stress decrease due to direct pore pressure and poro-elastic stressing, the thermal shrinkage of the rock, as result of thermo-elasticity, will reduce the pressure. In other words, there is a negative feedback loop unaccounted for when using linear superposition of ΔP , $\Delta\sigma_{\text{poro}}$ and $\Delta\sigma_T$. A more detailed investigation on the relation between the pore pressure, poro-elastic stress and the thermoelastic stress should be done in order to give a better estimate of the total stress alteration. In the PSM there is a linear superposition when adding the thermo-elastic stress, which makes the total stress decrease worse than is probably should be in a normal fault environment.

The equation used for the diffusion of the thermal front through the geothermal reservoir originates from Ganguly (2014) [24]. The assumptions with this equation are mentioned in section 7.1. One of these assumptions encompasses the fact that the reservoir is homogeneous and not heterogeneous. According to Ganguly (2014), the advancement of the thermal front in case of heterogeneous aquifer is initially greater than the homogeneous one. After some time (about 1000 days) actually the thermal front of the homogeneous one passes the one of the heterogeneous one and the average aquifer temperature at later times is also lesser for the homogeneous aquifer than the heterogeneous one. Thus in the long run the Physical Screening Model, which assumes the reservoir to be homogeneous, overestimated the speed of the thermal front.

With respect to the non-existing upper and lower boundaries, this will also add to the slower movement of the thermal front. Rock at the boundaries of the reservoir will reheat the reservoir from the bottom and the top. In thinner horizontal reservoir this will have a very significant influence. Results from Ganguly (2014) show that heat loss to the confining rock layers plays a vital role in slowing down the cooling of the reservoir [24]. Also clay structures inside the reservoir, where the fluids are not flowing, can have significant influence on the temperature preservation of the geothermal reservoir.

The stability of a fault due to the Mohr circle not crossing the Mohr-Coulomb criterion can be in some cases only a matter of a couple of kPa or Bars. The distinction between stable and unstable faults in a Mohr plot can be a small change in in-situ stress, which is why for most of the calculation in the Physical Screening Model the worst possible situation is assumed. Constructing a Mohr circle starts with finding the current stress field of the potential geothermal field. As this information is scarcely available, most of the time the current stress field is calculated according to standard methods. An (small) anomaly in the actual stress field or the pore pressure can have major impact on the stability calculations and thus on the outcome of SRA Step 1 of the new SRA.

During field exploitation the subsurface is investigated. An important matter in this investigation is the mapping of the faults in and outside of the reservoir. Their orientation with respect to the current regional stress field, their size and whether it's sealing or not are major important features of faults when investigating the possible reactivation of these faults. When faults are small, >1 km, they are often undetected. This means there is no possible way of knowing if they are present and where they are positioned. PSM Step 3 of the Physical Screening Model provides a way of showing what the maximal moment magnitude is of a seismic event. This includes the dimensions of the fault, thus with this step there is also a way of calculating the seismic hazard of smaller undetected faults and their seismic result.

The result from the PSM in chapter 7, isolated every step, and chapter 8, including the case studies, were consistent over the whole process. The PSM is only investigating the injection part of the geothermal operation as this is assumed to be the most dominant area related to induced seismicity [66]. Although this assumption is still would be wise to investigate potential seismicity around the producing well in a geothermal reservoir.

The new Seismic Risk Analysis created in this thesis is in some way an enhanced combination of the 3 existing SRA's discussed in chapter 4. While some assumptions of the PSM, and thus of the new SRA, might narrow the usage of this risk analysis, it is applicable for practically the whole Dutch subsurface. The assumption for the SRA is that the geothermal reservoir is laterally extensive and the primary stress direction is vertical (normal stress regime). While the contrary of both these assumptions is also investigated and calculated (see chapter 7.2, 7.3 and Appendix E) it is yet to be integrated into the new Seismic Risk Analysis. The integration of different geothermal reservoirs, like strike-slip regimes or non-lateral extensive reservoirs, should be done both in the new SRA and in the PSM. Although some of the steps for these systems are already done in this thesis, the SRA and PSM are not fully adjustable to these reservoir types.

10. CONCLUSION

This thesis exercised three main assignments:

- First it analysed and reviewed three SRA methodologies currently used for geothermal operations,
- Thereafter the design of a new and improved SRA method, based on the three existing SRA methodologies.
- The last and most extensive part of this thesis contained the development of a Physical Screening Model (PSM), which is part of the first step of the new SRA. This PSM is fairly quick and easy to use, and provides an analytical analysis on the seismic hazard that arises during geothermal production.

The three evaluated SRA's (SodM, Q-con/IF, TNO/Geomech) all have their up- and downsides. The main focus of the evaluation was on the first step(s) of the SRA's, containing the Quick Screening or Quick Scan that determined whether further investigation into seismic hazards and/or risks is necessary. Both the SodM and Q-con/IF methodologies predominantly lacked a solid physical study in this first step. While in the SodM method a few calculations were done that could indicate some quantifiable seismic hazard analysis, the first step of the Q-con/IF method only contained a simple scoring table. TNO/Geomech designed a calculating tool for seismic hazards, however, this tool required some adjustments to make it more applicable to realistic geothermal cases. The newly proposed SRA contains elements of all the three evaluated SRA methodologies.

SRA Step 1A and B, the main subjects of this thesis, directly originates from the Quick-Scan (Q-con/IF) and the TNO/Geomech-model. The indicated parameters from the Quick-Scan (Table 4-2, section 4.2) were combined and quantified in order to directly provide the fundament of the Physical Screening Model (SRA Step 1A), while the remaining parameters, which could still be significant in the SRA, were similar to the Quick-Scan in SRA Step 2A. The consecutive steps in this new SRA, SRA Step 2A/B and the monitoring steps (SRA Step 3), correspond to further steps taken in the SodM and Q-con/IF SRA's. The improvement of this new SRA, including the Physical Screening Model, lies in the more elaborate, more physical and more evidential based manner of determining a possible seismic hazard in geothermal reservoirs.

SRA Step 1A of the new SRA is a Physical Screening Model. This model contains four different steps of which the first two, the diffusion of ΔP , $\Delta\sigma_{poro}$, ΔT and illustrating these differences in a Mohr diagram with the current regional stress field, are most important for the SRA in defining whether faults in the system are stable or not. Step 3 and 4 of the PSM, calculating the M_w and the PGV, present an indication of the maximal hazard when a seismic event occurs. The outcome of SRA Step 1A (the PSM) is then combined with the outcome of SRA Step 1B, the Quick Scan, in order to complete SRA Step 1. The Physical Screening Model, while it still is a fairly quick and easy to use, provides simple and clear results that give an indication of the maximum seismic hazard that can occur when producing from a geothermal reservoir.

The consecutive steps in this new SRA, SRA Step 2A/B and the monitoring steps (SRA Step 3), correspond to further steps taken in the SodM and Q-con/IF SRA's. SRA Step 2A is a more detailed and full location specific SRA. This part of the SRA requires considerable more effort, as it will include a reservoir specific flow-and-production model. SRA Step 2B is made to evaluate the risk situation of the seismic hazard.

Sensitivity analysis on the input parameters of the Physical Screening Model shows that permeability, injection pressure, and injection temperature all are the dominant factors in the ultimate result of the PSM; the seismic hazard. Permeability and injection pressure mainly influence the diffusion of ΔP , $\Delta\sigma_{\text{poro}}$ and ΔT , while the injection temperature has the biggest influence on $\Delta\sigma_T$.

Both the Case studies done in this study give an example of what to expect when going through step 1 of the new SRA. While the first case study, the DAP project, passes in all categories, the second case study, the extreme case, gives a good illustration of what happens when the key parameters do not co-operate.

RECOMMENDATION

In order to provide the best conclusions of this thesis some recommendations are listed below to improve this work:

- The first recommendation will be the same topic as discussed in the chapter 9; the linear superposition of the stress alterations due to pressure and temperature change will overestimate the seismicity prediction. A coupling between ΔP , $\Delta\sigma_{\text{poro}}$ and $\Delta\sigma_T$ will give a better prognosis of the situation.
- Secondly comes the iterative fault model introduction. Here the fault will be divided into patches, when one patch begins to slip it activates surrounding patches by transferring the stress. This is explained in section 6.7. Introducing such a model will provide a better estimate of the PSM.
- When studying the subsurface there are a lot of uncertainties to deal with. The same hold for this thesis; many parameters that are put in the PSM are estimations or concluded from extrapolated data. In the PSM the current outcome is simply one number or one figure, when dealing with such uncertain input data this is probably not sufficient. Using a Monte Carlo simulation will help to investigate more potential outcomes and also the most likely outcome. It uses randomness to solve for the uncertainty of input data and therefore provides a wider picture than the PSM presents right now.

APPENDIX

APPENDIX A: SRA STEP 2B

In the risk analysis in step 2B of the new SRA, the most important influence factors from the subsurface and aboveground are considered and classified. Figure 5-2 shows a cause-result relations model of induced seismicity with a spider plot. Points are assigned based on the classification. The assigned points for the influence factors are then summed and normalized to determine the values for the subsurface and surface. These two normalized numbers are then plotted against each other in the risk plot, figure 5-3.

Besides some alteration in order to fit it in the proposed new SRA it, this part of the SRA step 2B is similar to the second step of the SodM SRA [6].

The various influencing factors are discussed below.

INFLUENCE FACTORS SUBSURFACE

The influence factors and the classification for these factors are given in Table A. The classifications are described below.

1. **Chance of inducing seismicity:** The probability that tremors are induced is determined based on the DHAS analysis. This analysis has already been performed in SRA step 1 of the SodM approach. The result can be used directly in the classification.
2. **The maximal Moment magnitude (M_0):** The magnitude of one seismic event that must be realistically taken into account is calculated in PSM step 4. The result can be used directly in the classification.
3. **Location:** In the north of the Netherlands (including Noord-Holland) there is a thick layer of Zechstein salt, which is often the final layer of the existing gas deposits. Salt at a depth of ~ 3km behaves fluidly and will flow to relax the tensions in the salt. This creates extra tension just above and below a thick layer of salt. Since the start of gas extraction, it has never happened that induced earthquakes occurred in fields south of the Amsterdam-Arnhem line, where the Zechstein salt deposits are missing. When a geothermal operation is done north of the Amsterdam-Arnhem line but above the Zechstein salt layer it should be considered south of the Amsterdam-Arnhem line (and thus 0 point).
4. **Local “opslinger”:** In the shallow types of soil and the associated surges are mapped. The geothermal field to be analysed must be projected on the map and the percentage of the field above the different soil types analysed. The “opslingfactor” (“amplificationfactor” discussed in section 6.8) can be classified based on the determined percentages.

To determine the threat, the point values associated with the classification of the four factors are summed and normalized with the maximum number of points to be achieved (= 14).

Table A. the classification of the below ground influence factors

	DHAIS	M ₀	Location	Local "opslinger"
5		>4.5		
4	> 5 seismic activities per year with M ₀ ≥1.5	4.1 - 4.5		
3	< 5 seismic activities per year with M ₀ ≥1.5	3.6 - 4		> 60% soft soil (V _{s,30} = <200 m/s) and/or > 30% soil type that are extra sensitive to amplification, such as peat layers thicker than 3 m and soft peat layers with a thickness of 1-3 m located on a rigid surface.
2	P=42% or seismic activities with M ₀ ≥1.5	3.1 – 3.5	North of Amsterdam-Arnhem line	30-60% soft soil (V _{s,30} = <200 m/s) and/or 15-30% soil type that are extra sensitive to amplification, such as peat layers thicker than 3 m and soft peat layers with a thickness of 1-3 m located on a rigid surface.
1	P=19%	2.6-3		10-30% soft soil (V _{s,30} = <200 m/s) and/or 5-15% soil type that are extra sensitive to amplification, such as peat layers thicker than 3 m and soft peat layers with a thickness of 1-3 m located on a rigid surface.
0		≤2.5	South of Amsterdam-Arnhem line	<10% soft soil (V _{s,30} = <200 m/s) and/or <5% soil type that are extra sensitive to amplification, such as peat layers thicker than 3 m and soft peat layers with a thickness of 1-3 m located on a rigid surface.

INFLUENCE FACTORS ABOVEGROUND

The result factors and the classification for these factors are given in Table B. The way in which the classification must be determined is described below. General remark here is that a 5 km buffer zone is taken from the edge of the field. The reason for this is that tremors on the edge fractures of a field within this distance can still cause significant ground movements. This can also be seen in the GMP in step 4 of the PSM.

1. **Population density & buildings:** The population density, or the number of inhabitants per km², can be determined by mapping the area of the field within the various municipalities where the field is located. The average population density can be read per municipality on the population density map (CBS Statline). Based on the area within the various municipalities, a weighted average for the population density above the geothermal field can then be determined, which can be classified. For very small fields, the "population density per neighbourhood" may also be used (CBS Statline). In addition, the existing buildings are also taken into account in this category. The type of buildings plays an important role, but is difficult to specify. It is possible to determine whether there are areas with flats/apartment complexes present. This is processed in this category.
2. **Industrial constructions:** At '<http://www.risicokaart.nl>' the presence of industrial facilities above and around the field can be inventoried and this factor can be classified.
3. **Special buildings and vital infrastructure:** At '<http://www.risicokaart.nl>' the presence of schools, hospitals, homes and public buildings where many people come together can be mapped and this factor can be classified.

4. **Dikes:** The presence of primary and / or secondary dikes can be mapped on 'http://www.risicokaart.nl'.

To determine the results factor, the point values associated with the classification of the four factors are summed and normalized with the maximum number of points to be achieved (= 16).

Table B. the classification of the above ground influence factors

	Population density (inhabitants per km ²)	Industrial constructions	Special buildings and vital infrastructure	Dikes
4	> 2500	Multiple directly above the field	Multiple hospitals and/or energy facilities directly above the field	Primary dikes above the field.
3	1000-2500 and/or 500-1000 with neighbourhoods consisting of flats/apartment complexes within 5 km of the field.	1 above the field and/or several within 5 km of the field.	1 hospital and/or energy supply directly above the field or several within 5 km around the field. Multiple schools, homes and/or public buildings directly above the field.	Primary dikes within 5 km of the field and/or secondary dikes above the field.
2	500-1000 and/or 250-500 with neighbourhoods consisting of flats/apartment complexes within 5 km of the field.	1 within 5 km of the field.	1 school, home and/or public building above the field or several within 5 km of the field.	Secondary dikes within 5 km of the field
1	250-500 and/or <250 with neighbourhoods consisting of flats/apartment complexes within 5 km of the field.		1 school, home and/or public building within 5 km of the field.	
0	<250	None within 5 km of the field.	None above and/or within 5 km of the field	No dikes within 5 km of the field

APPENDIX B: RUDNICKI EQUATIONS EXTENSION

In this part of the appendix the origin of the dimensionless variable that stands for the fluid volume transported into or out of storage, ζ , will be explained.

Rice and Cleary (1976) defined the mass fluid content, m_f , as a fluid mass per unit reference volume. In order to investigate the change in fluid mass content, which can be stated like $\delta m = m_f - m_0$ (with m_0 being the reference state), ζ was introduced:

$$\zeta = \frac{\delta m_f}{\rho_{f_0}} \quad [A1]$$

where ρ_{f_0} = fluid density in the reference state [kg/m³]

δm_f = mass fluid per unit volume.

Now writing this in the equations that relate the strain (ϵ) with the incremental fluid change (ζ) with the stress (σ) and pore pressure (P) in all the principle coordinates, there is:

$$\epsilon_1 = \frac{1}{E}\sigma_1 - \frac{\nu}{E}\sigma_2 - \frac{\nu}{E}\sigma_3 + \frac{1}{3H}P \quad [A2]$$

$$\epsilon_2 = -\frac{\nu}{E}\sigma_1 + \frac{1}{E}\sigma_2 - \frac{\nu}{E}\sigma_3 + \frac{1}{3H}P \quad [A3]$$

$$\epsilon_3 = -\frac{\nu}{E}\sigma_1 - \frac{\nu}{E}\sigma_2 + \frac{1}{E}\sigma_3 + \frac{1}{3H}P \quad [A4]$$

$$\zeta = \frac{1}{3H}P(\sigma_1 + \sigma_2 + \sigma_3) + \frac{1}{R}P \quad [A5]$$

where E = Young's modulus [GPa]

v = Poisson's ratio [-]

$\frac{1}{H} \equiv \frac{\delta\varepsilon}{\delta P} |_{\sigma=0}$ = poro-elastic expansion coefficient [-]

$\frac{1}{R} \equiv \frac{\delta\zeta}{\delta P} |_{\sigma=0}$ = unconstrained specific storage coefficient [-].

The poro-elastic expansion coefficient describes the change in bulk volume due to a change in pore pressure under constant stress conditions and unconstrained specific storage coefficient describes the change in increment of fluid content due to pore pressure change under constant stress [3].

Adding Eq. A2, A3 and A4 and using the mean normal stress σ ($=(\sigma_1 + \sigma_2 + \sigma_3)/3$), result in the following changes for the Eq. A2 – A5

$$\varepsilon = \frac{1}{K_d}\sigma + \frac{\alpha}{K_d}P \quad [A6]$$

$$\zeta = \frac{\alpha}{K_d}\sigma + \frac{\alpha}{K_d B}P \quad [6.22]$$

where K_d = drained bulk modulus [Pa]

α = Biot-Willis coefficient [-].

APPENDIX C: THERMOELASTIC DIFFUSION EQUATIONS EXTENSION

This appendix will provide the missing steps in the generation of the thermoelastic diffusion equation.

Eq. 6.65, the particular solution, is converted into

$$\bar{T} = \frac{T_0}{s} - \frac{2}{\pi^{\frac{1}{2}}}(T_0 - T_{in}) \exp\left(\frac{K_2 x}{2\lambda}\right) \int_0^\infty \exp\left(-\zeta^2 - \frac{K_2^2 x^2}{16\lambda^2 \zeta^2}\right) \frac{\exp\left(\frac{K_1 x^2 s}{4\lambda_c \zeta^2}\right)}{s} d\zeta \quad [A7]$$

where T_0 = initial temperature [°C]

T_{in} = injection temperature [°C]

s = complex number [-]

x = longitudinal direction [m]

λ_c = thermal conductivity of the porous medium [W/m °C]

ζ = incremental step.

This conversion is facilitated by the integral solution given by Gradshteyn and Ryzhik [29], which states

$$\int_0^\infty \exp\left(-\zeta^2 - \frac{b^2}{\zeta^2}\right) d\zeta = \frac{\pi^{\frac{1}{2}}}{2} \exp(-2b) \quad [A8].$$

Next applying the inverse Laplace transformation on Eq. A7 result in

$$T = T_0 - \frac{2}{\pi^2} (T_0 - T_{in}) \exp\left(\frac{K_2 x}{2\lambda}\right) \int_0^\infty \exp\left(-\zeta^2 - \frac{K_2^2 x^2}{16\lambda^2 \zeta^2}\right) \cdot u\left(t - \frac{K_1 x^2}{4\lambda \zeta^2}\right) d\zeta \quad [A9].$$

APPENDIX D: DIFFUSION OF ΔP , $\Delta \Sigma_{\text{PORO}}$ (7.1.1)

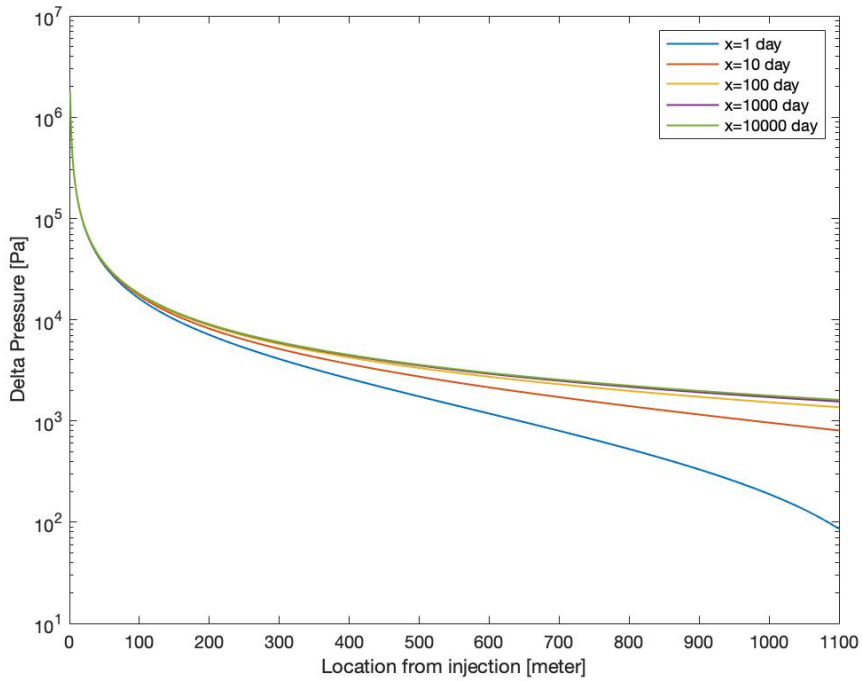


Figure A-1. Plot of the $\Delta \sigma_{\text{tan}}$ over location from the injector after five different time scales. The change in pore pressure over the whole system is negligible after 100 days, while this holds after 1 day up to a 100-meter radius from the injector.

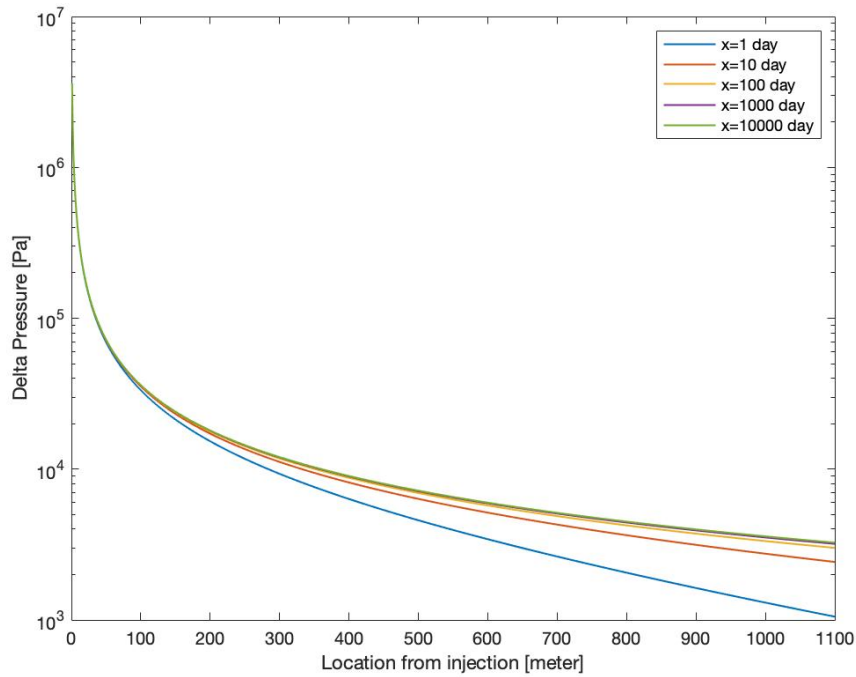


Figure A-2. Plot of the $\Delta\sigma_{rad}$ over location from the injector after five different time scales. The change in pore pressure over the whole system is negligible after 100 days, while this holds after 1 day up to a 100-meter radius from the injector.

APPENDIX E: MOHR CIRCLES FOR THRUST FAULTS AND STIKE SLIP REGIMES

In a thrust fault regime the results are opposite of these of a normal regime because now the primary stress is in the horizontal direction. It can be seen in figure A-3 that the poro-elasticity in the horizontal direction (which should be used in a PSM for thrust fault regimes because of the horizontal extensive reservoir assumption) has an amplifying effect on the Mohr circle. Figure A-4 subsequently shows the final Mohr circle including the thermo-elastic stress decrease. Here the $\Delta\sigma_T$ has a weakening effect on the Mohr circle because the $\Delta\sigma_T$ now only works on the now horizontal σ_1 .

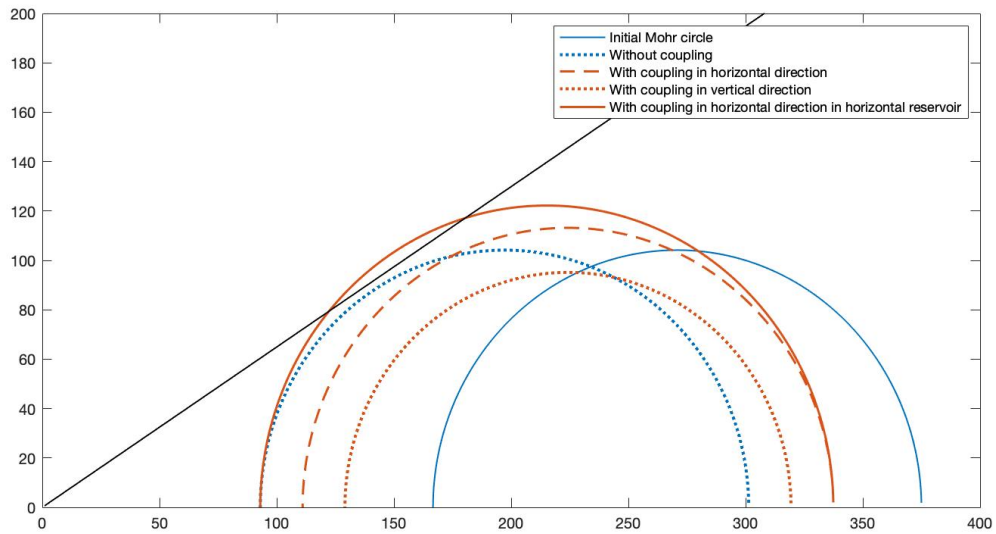


Figure A-3. Mohr plot with the two different observation points and a failure envelope. Except for the initial Mohr circle all the Mohr circles are after 3000 days of injection at a 1-meter radius from the injector. The two red Mohr circles include $\Delta\sigma_{\text{poro}}$ but not $\Delta\sigma_T$. The dotted blue Mohr circle is without thermo-elastic and poro-elastic coupling.

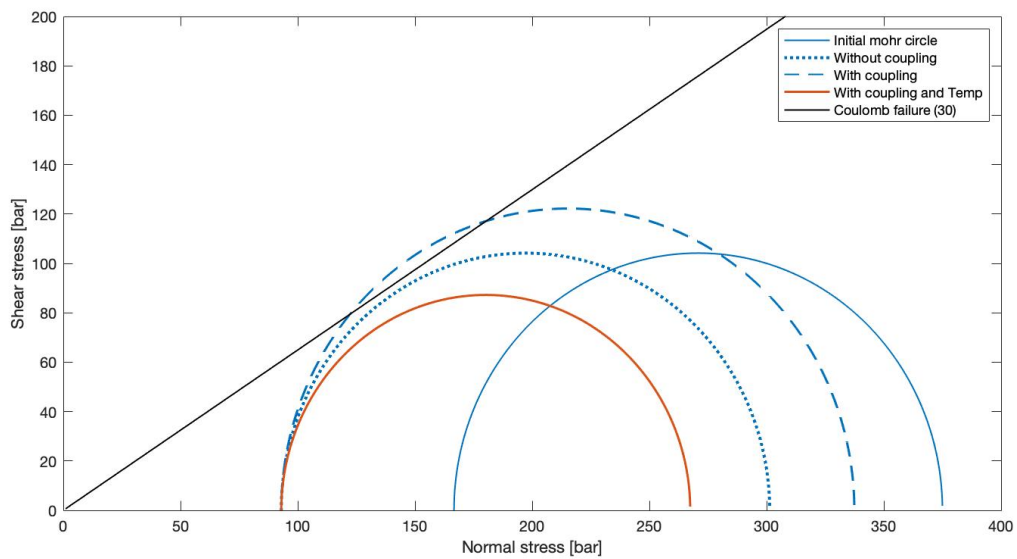


Figure A-4. Mohr plot with four different Mohr circles and a failure envelope. Except for the initial Mohr circle all the Mohr circles are after 3000 days of injection at a 1-meter radius from the injector. The difference between the Mohr circles with and without poro-elastic coupling is considerable.

In a strike slip regime both the maximal and minimal primary stress act horizontally, but have different result on the effect of poro-elasticity, see figure A-5. As both the minimal and maximal primary stresses are in the horizontal direction, both are affected by the temperature decrease and subsequently by the $\Delta\sigma_T$. Figure A-6 shows that this thermo-elastic stress decrease results in a substantial higher fault reactivation hazard.

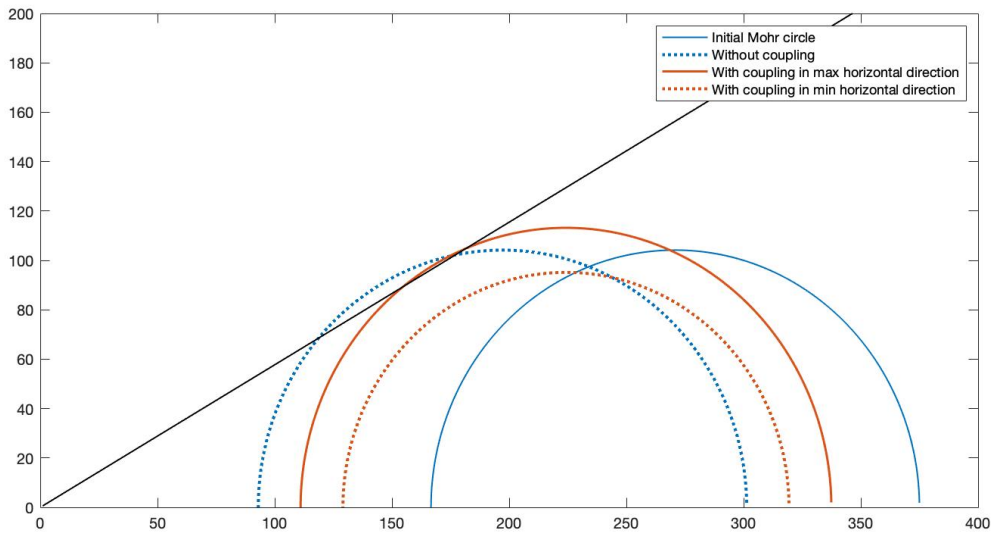


Figure A-5. Mohr plot with the two different observation points and a failure envelope. Except for the initial Mohr circle all the Mohr circle are after 3000 days of injection at a 1-meter radius from the injector. The two red Mohr circles include $\Delta\sigma_{poro}$ but not $\Delta\sigma_T$. The dotted blue Mohr circle is without thermo-elastic and poro-elastic coupling. Note that here both Mohr circles including coupling are in the horizontal direction.

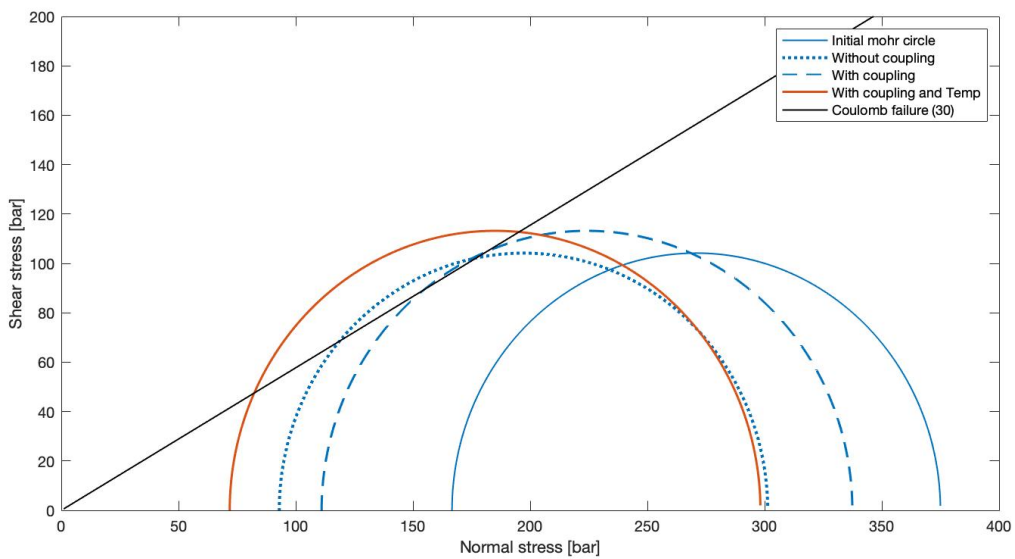


Figure A-6. Mohr plot with four different Mohr circles and a failure envelope. Except for the initial Mohr circle all the Mohr circle are after 3000 days of injection at a 1-meter radius from the injector. The difference between the Mohr circles with and without poro-elastic coupling is considerable.

APPENDIX F: SENSIBILITY ANALYSIS OF K (8.1.1)

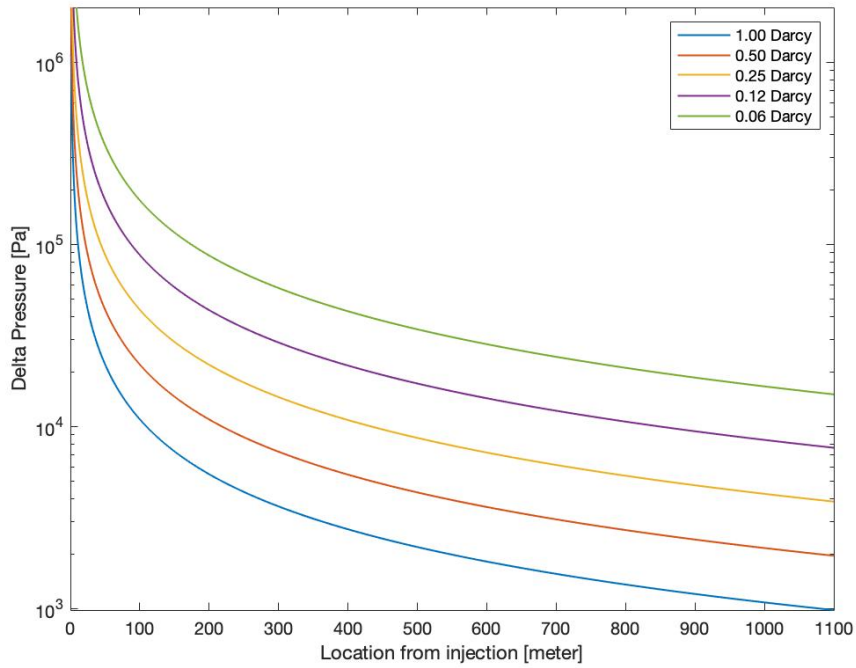


Figure A-7. Plot of the $\Delta\sigma_{rad}$ over location from the injector after 1000 days with five different permeabilities.

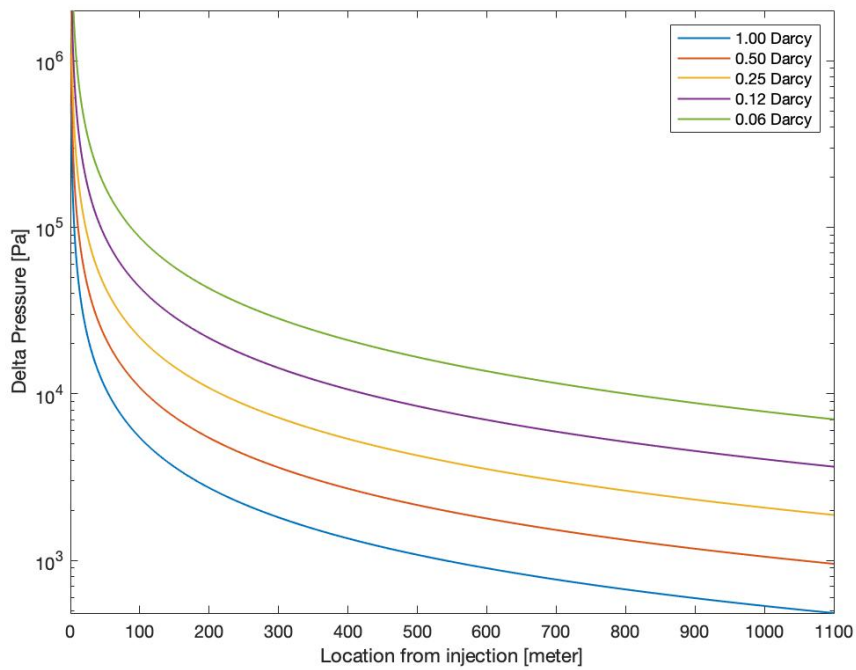


Figure A-8. Plot of the $\Delta\sigma_{tan}$ over location from the injector after 1000 days with five different permeabilities.

APPENDIX G: SENSIBILITY ANALYSIS OF INJECTION RATE (8.1.2)

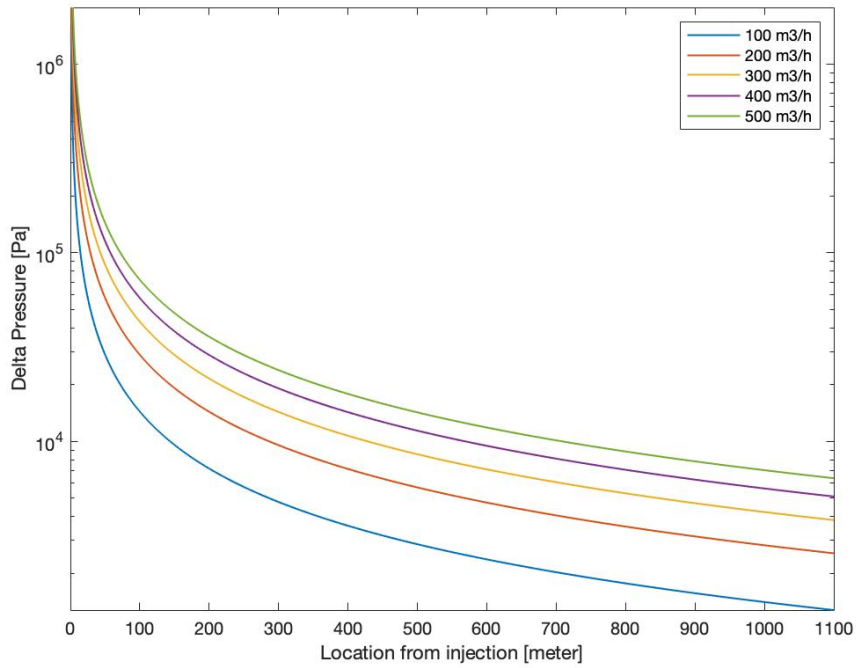


Figure A-9. Plot of the $\Delta\sigma_{rad}$ over location from the injector after 1000 days with five different injection rates.

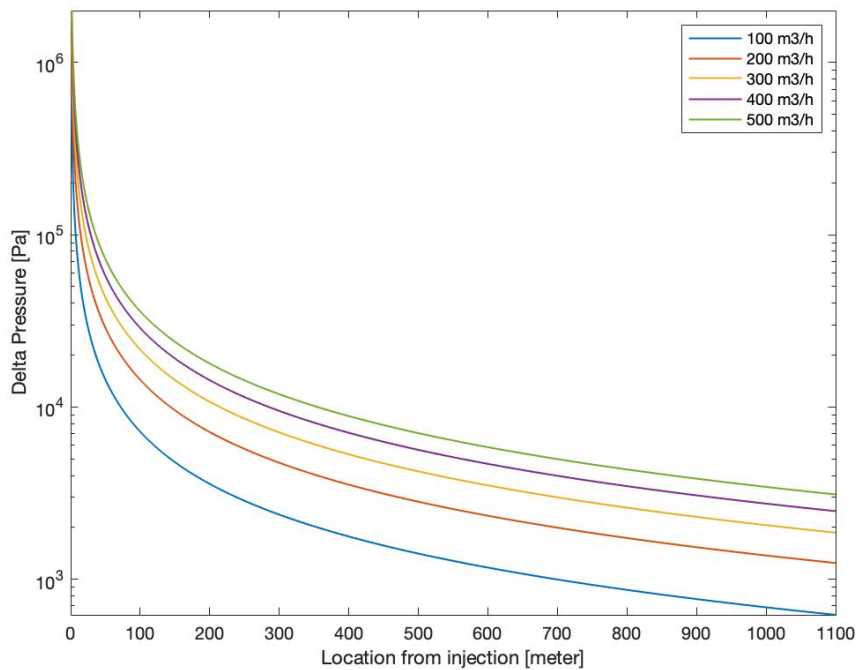


Figure A-10. Plot of the $\Delta\sigma_{tan}$ over location from the injector after 1000 days with five different injection rates.

APPENDIX H: SENSIBILITY ANALYSIS OF ELASTIC MODULI (8.1.4)

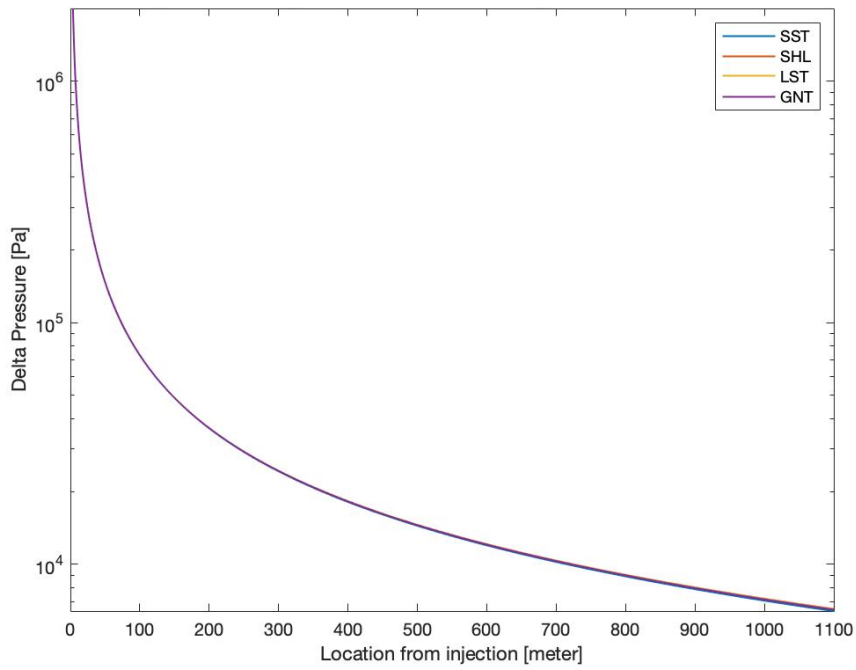


Figure A-11. Plot of the ΔP over location from the injector after 1000 days with five different permeabilities.

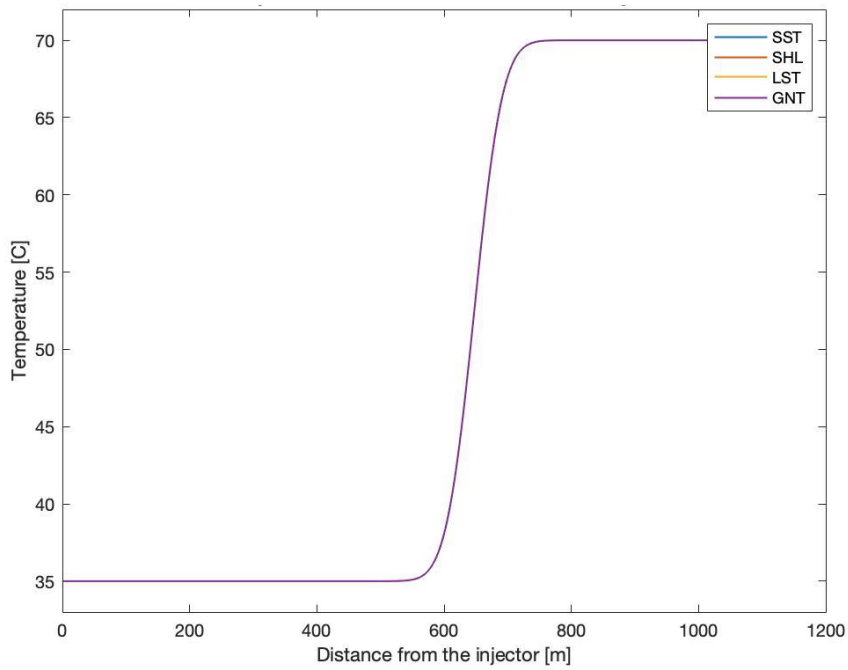


Figure A-12. Plot of the thermal front over distance from the injector after 40 years of constant injection the four different rock types.

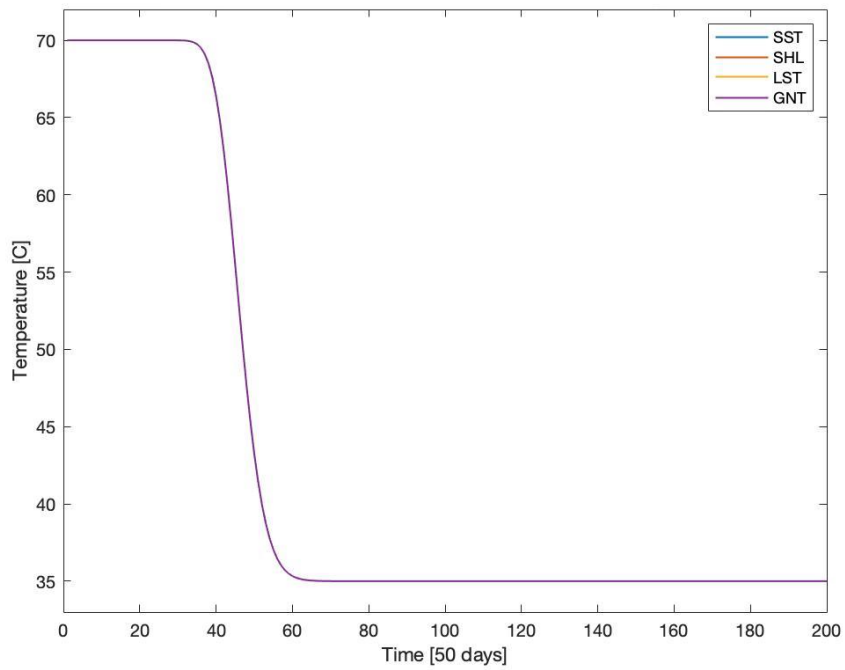


Figure A-13. Plot of the thermal front over time at 150 meters from the injector with the four different rock types.

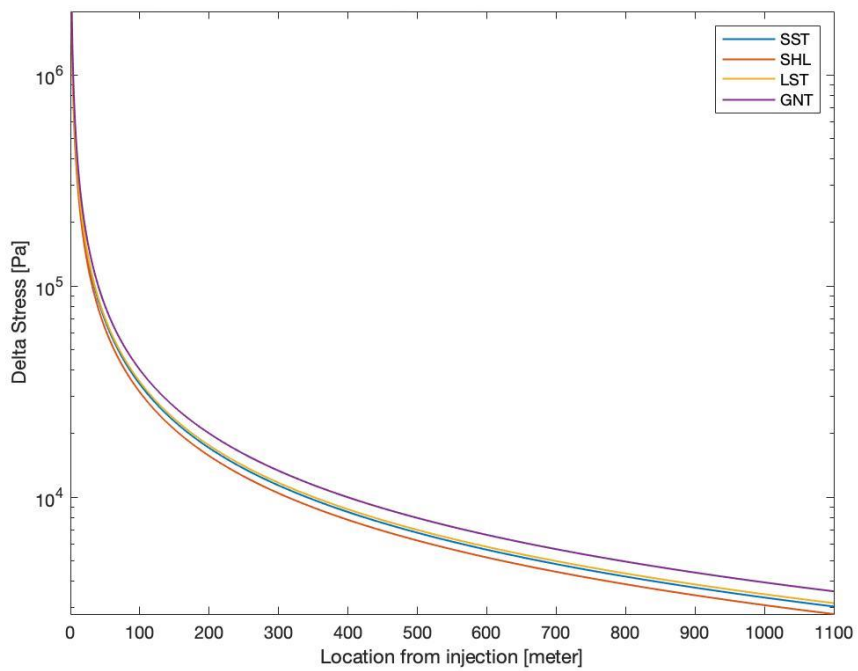


Figure A-14. Plot of the $\Delta\sigma_{rad}$ over location from the injector after 1000 days with the four different rock types.

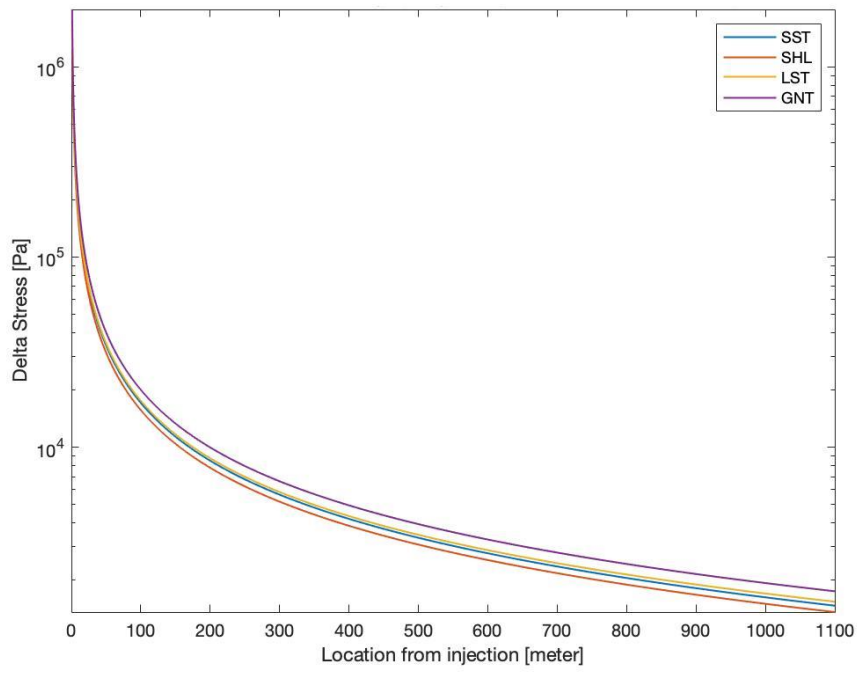


Figure A-15. Plot of the $\Delta\sigma_{tan}$ over location from the injector after 1000 days with the four different rock types.

APPENDIX I: DAPWELL PROJECT CASE STUDY (8.2)

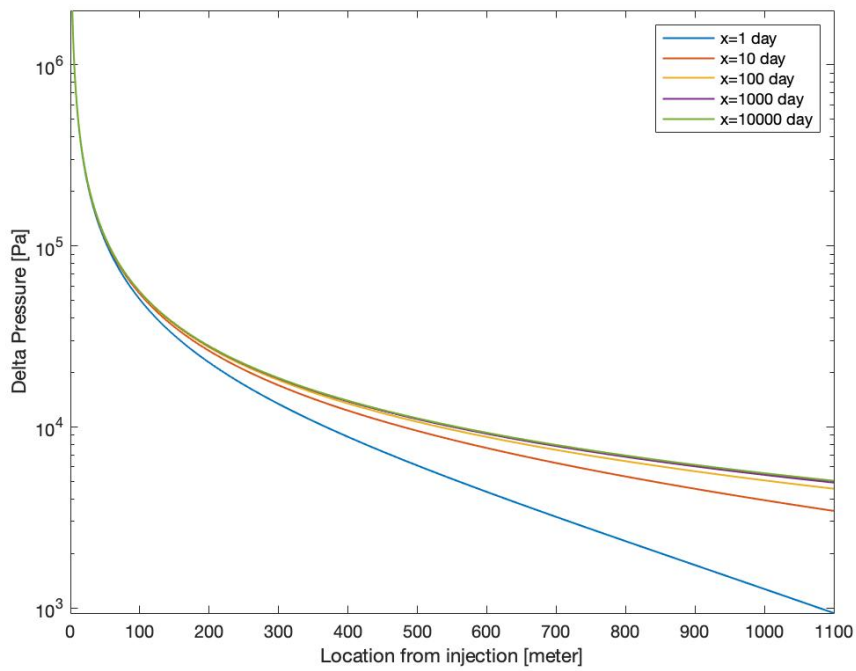


Figure A-16. Plot of the ΔP of the DAPwell case over location from the injector after five different time intervals; 1, 10, 100, 1000, 10000 days.

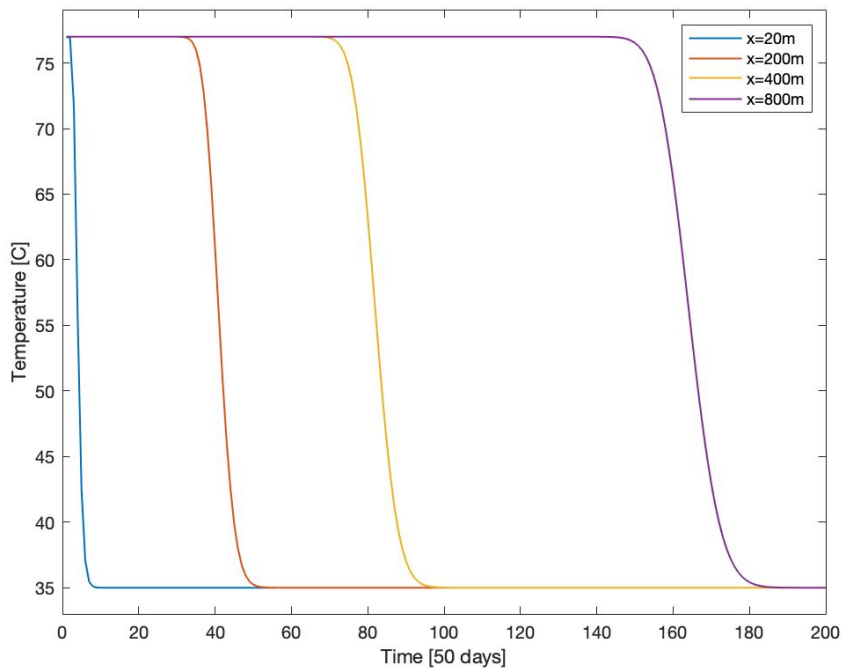


Figure A-17. Plot of the thermal front evolution of the DAPwell case over time at four different locations, 20, 200, 400 and 800 meters from the injection point.

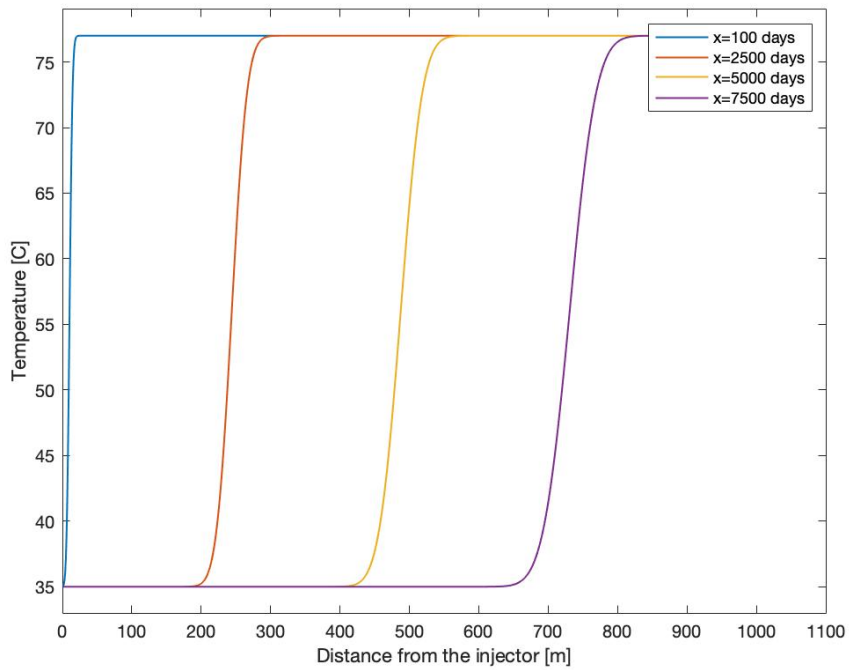


Figure A-18. Plot of the thermal front evolution of the DAPwell case over location at four different time intervals, 100, 2500, 5000 and 7500 days of injection.

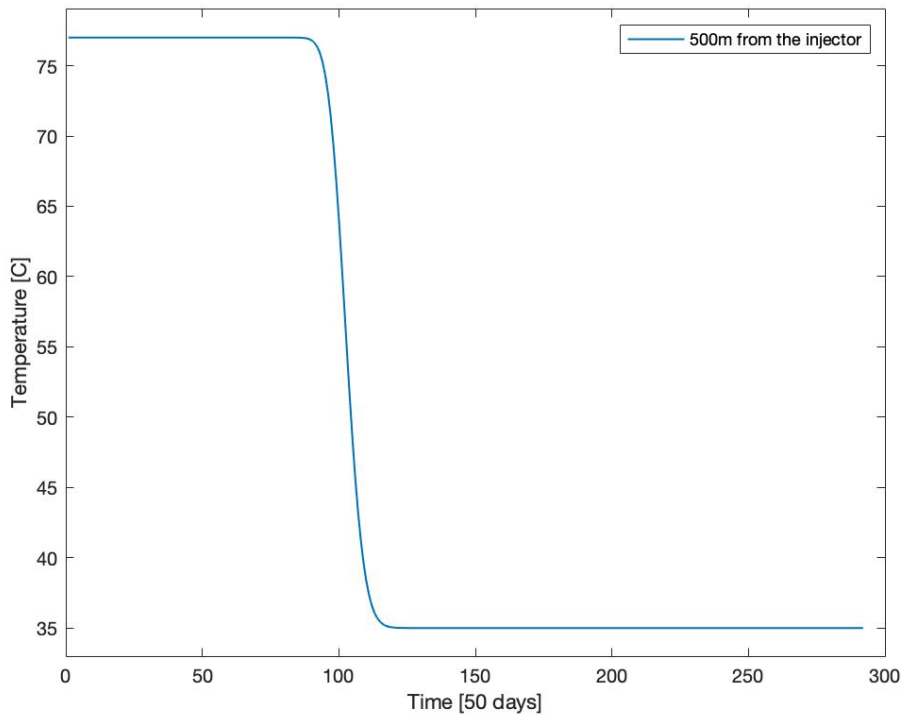


Figure A-19. The temperature decrease of the reservoir at 500 meters from the injector. After 4500 days the thermal front arrives decreasing the reservoir to 35 degrees C in approximately 1250 days.

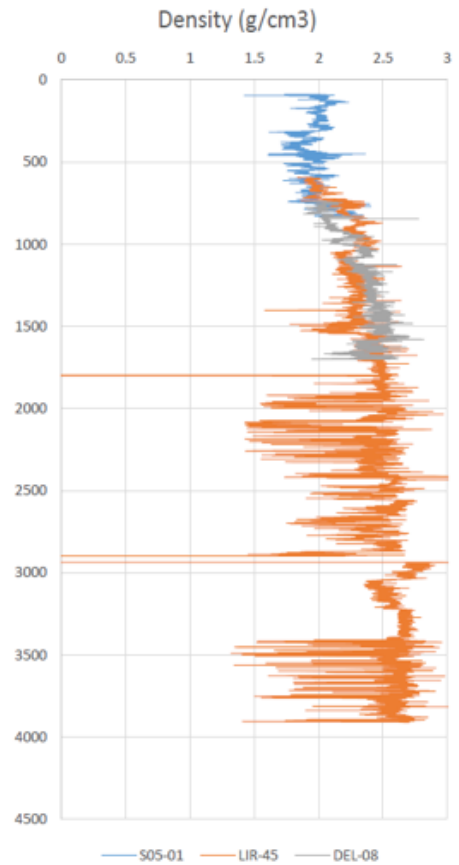


Figure A-20. Density log of well LIR-45/S05-01/DEL-08: resulting in a vertical stress gradient of 0.207-0.213 bar/m at the DAP well location. Courtesy: Panterra.

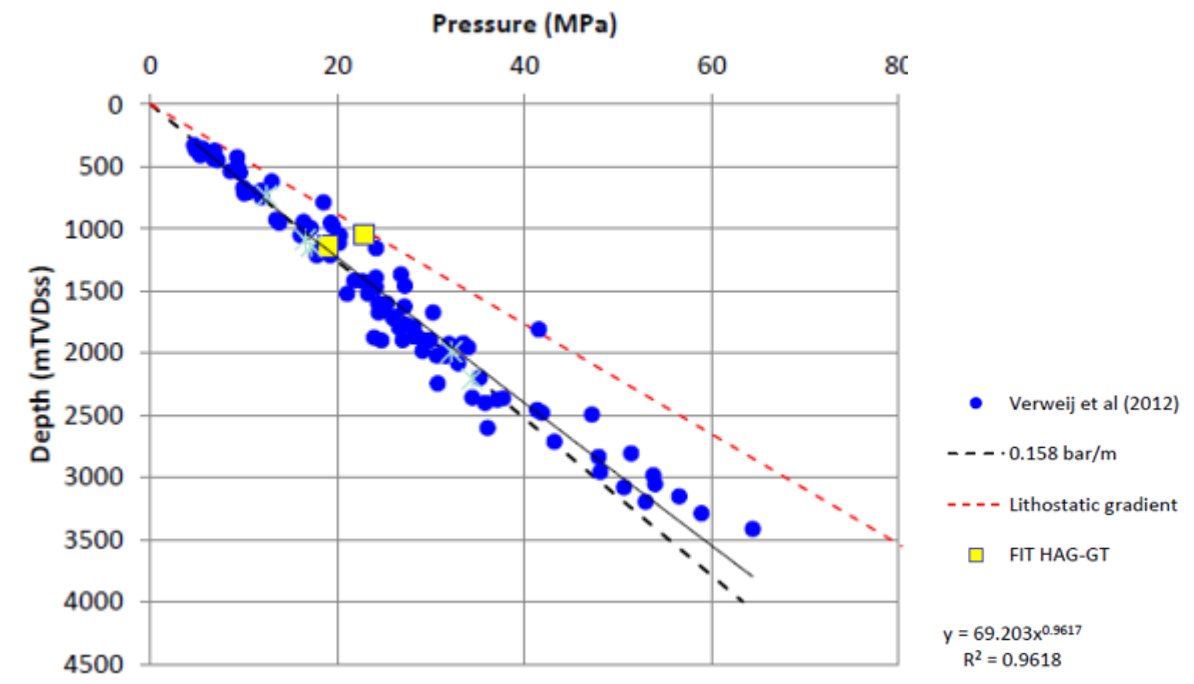


Figure A-21. FIT test HAG-GT-01: resulting in a horizontal stress gradient is 0.165 bar/m at the DAP well location. Courtesy: Panterra.

APPENDIX J: MODEL COMPARISON

Comparing the steps in the Physical Screening Model with excising models will provide more validation to the newly created model. The PSM will be compared with the following models:

1. TNO/GEOMECH model [64] – comparing the Mohr plot outcomes.
2. DoubletCalc (TNO) [18] – comparing the temperature diffusion.

1. TNO/GEOMECH MODEL

The pros and cons of this model are already discussed in chapter 4. Here the investigation continues with the comparison with the outcome of the PSM. The input parameters from Table C are used for this case in both models.

Table C. Input parameters for both the TNO/GEOMECH model and the PSM.

Input parameter	Value
Biot-Willis coefficient	0.75
Shear modulus	5 GPa
Poisson ratio	0.25
Young modulus	10 GPa
Fluid density	1000 kg/m ³
Volumetric flow rate	200 m ³ /h
Depth Reservoir	2000 m
Temperature reservoir	70 °C
Temperature injection water	35 °C

When inserting the parameters in the PSM the pressure difference, ΔP , at the well location is 3.5 MPa, this is then subsequently inserted into the TNO/GEOMECH model. Thus completely using the same input parameters, figures A-22 and A-23 show the resulting Mohr plots of respectively the TNO/GEOMECH model and the PSM. The result are comparable, in Table D the primary stresses are noted.

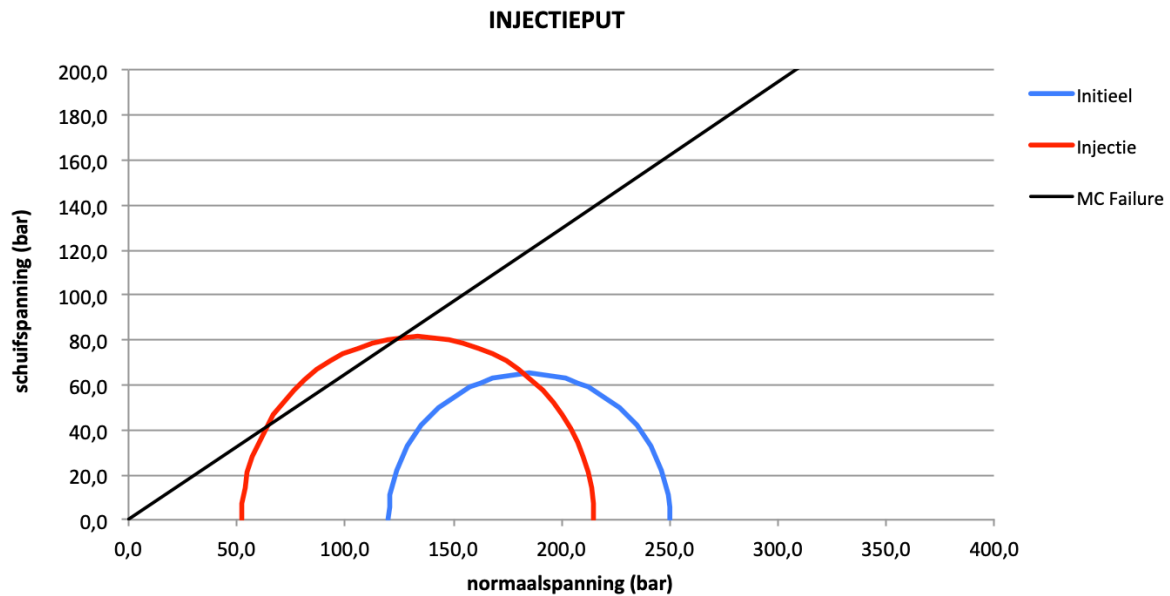


Figure A-22. Mohr plot with the initial Mohr circle and the after-injection Mohr circle at the well location from the TNO/GEOMECH model.

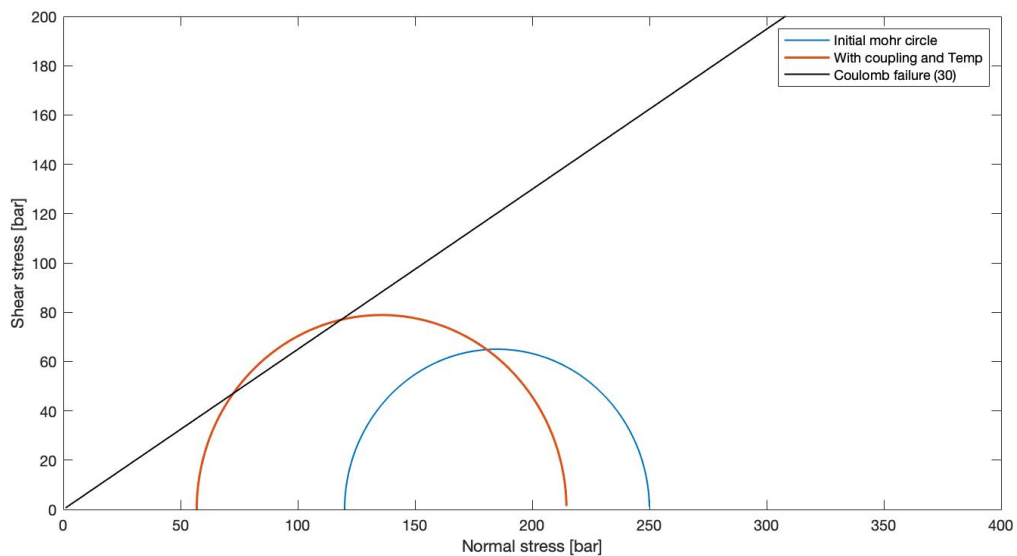


Figure A-23. Mohr plot with the initial Mohr circle and the after-injection Mohr circle at the well location from the PSM.

Table D. Output of the principal stresses after injection of the Mohr circles from figures A-21 and A-22.

	TNO/GEOMECH	PSM
σ_1	215 bar	215 bar
σ_3	52 bar	57 bar

From Table D it is visible that both model produce similar results. σ_1 is the same for both models because the injection pressure is the same for both models. This is a result from the assumption that it concerns a horizontal reservoir, where there is no additional additions or subtractions other than the direct pore pressure from the largest stress in the vertical direction.

2. DOUBLET-CALC (TNO)

The spatio-temporal evolution of both the pore pressure and temperature can be calculated with DoubletCalc. For both models using the same input parameters, see Table E (using the default parameters from Doubletcalc), the outcome for both the DoubletCalc and the PSM can be compared. In figures A-24 and A-25 the visual comparison between the two models are shown.

Table E. Input parameters for both the DoubletCalc model and the PSM.

Input parameter	Value
Permeability	0.381 Darcy
Fluid viscosity	0.8 cP
Biot-Willis coefficient	0.75
Shear modulus	5 GPa
Poisson ratio	0.35
Young modulus	9 GPa
Fluid density	1000 kg/m ³
Volumetric flow rate	200 m ³ /h
Depth Reservoir	1500 m
Temperature reservoir	65 °C
Temperature injection water	30 °C
Thermal conductivity of the aquifer	2.26 W/m °C
Thermal conductivity of the rock	4 W/m °C
Thermal conductivity of the water	0.6 W/m °C

Note that for the thermal conductivity the PSM is the average effective thermal of the aquifer is taken, while in the Doubletcalc this is separated into the fluid and rock conductivity. This can simply be converted to one another by using this equation:

$$\lambda_c = \lambda_{c,matix}^{1-\varphi} * \lambda_{c,water}^{\varphi} \quad [A10]$$

where: λ_c = thermal conductivity of the aquifer [W/m °C]

$\lambda_{c,matix}$ = specific thermal conductivity of the rock of the aquifer [W/m °C]

$\lambda_{c,water}$ = specific thermal conductivity of the water in the aquifer [W/m °C]

φ = porosity of the aquifer [-].

Despite using different equations in the models and the PSM only looks at the injector and the producer separately, figures A-24 and A-25 are similar in outcome after 40 years of production. In both models the thermal front has reached up to about 600 meters form the injector after these years.

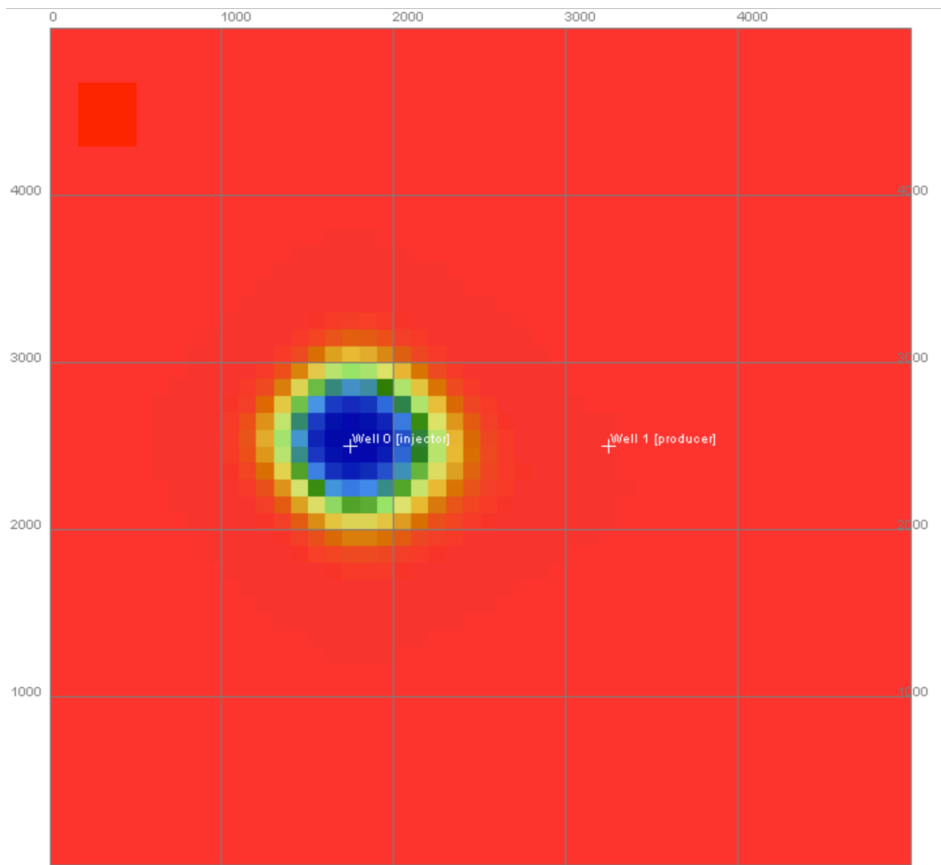


Figure A-24. Screenshot taken from the DoubletCalc model. A top view map of the reservoir and the expansion of the thermal front after 40 years of injection.

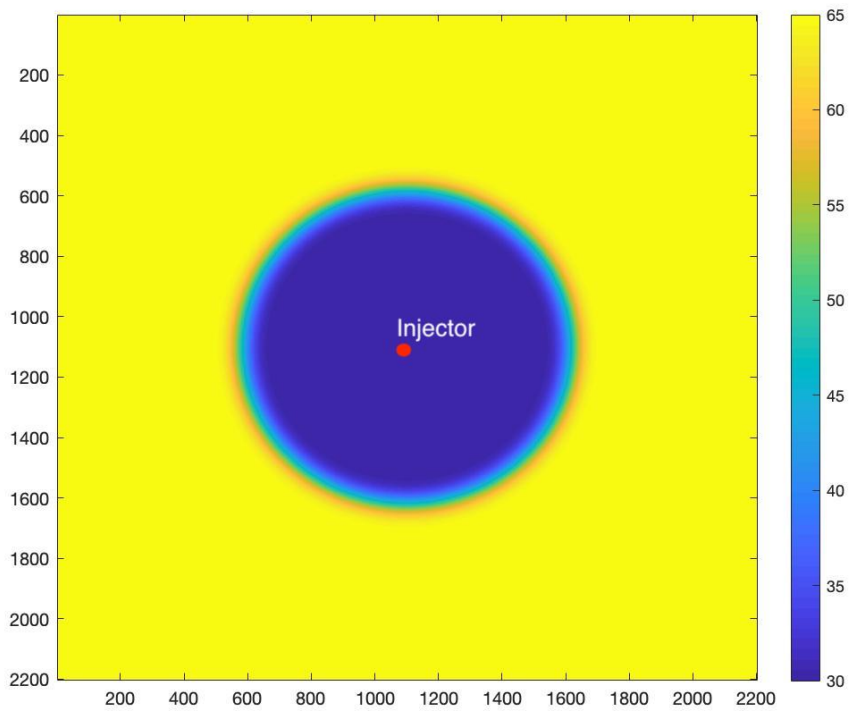


Figure A-25. A top view map of the reservoir and the expansion of the thermal front after 40 years of injection from the PSM.

12. REFERENCES

- [1] Abercrombie, R.E. (1995). Earthquake source scaling relationships from –1 to 5 ML using seismograms recorded at 2.5-Km depth. *J. Geophys. Res.* 100, 24015–24036.
- [2] Agemar, T., Weber, J., Schulz, R. (2014). Deep Geothermal Energy Production in Germany. *Energies*. 7. 4397-4416. 10.3390/en7074397.
- [3] Altmann, J. B. (2010). Poroelastic effects in reservoir modelling. *Karlsruher Instituts für Technologie*.
- [4] Altmann, J. B., Müller, T., Müller, B., Tingay, M. and Heidbach, O. (2010). Poroelastic Contribution to the Reservoir Stress Path. *International Journal of Rock Mechanics and Mining Sciences*, 47(7), 1104-1113.
- [5] Altmann, J. B., Müller, B., Müller, T., Heidbach, O., Tingay, M., Weißhardt, A. (2014). Pore pressure stress coupling in 3D and consequences for reservoir stress states and fault reactivation. *Geothermics*, 52, p. 195-205.
- [6] Baisch, S., Koch, C., and Stang, H. (Q-con GmbH and IF technology B.V.) (2016). Defining the Framework for Seismic Hazard Assessment in Geothermal Projects V0.1 - Technical Report.
- [7] Bommer, J. J., Stafford P. J., Ntinalexis, M. (2017). Empirical Ground-Motion Prediction Equations for Peak Ground Velocity from Small-Magnitude Earthquakes in the Groningen Field Using Multiple Definitions of the Horizontal Component of Motion. Updated Model for Application to Smaller Earthquakes. *NAM*.
- [8] Bourne, S.J., Oates, S.J., van Elk, J., and Doornhof, D. (2014). A seismological model for earthquakes induced by fluid extraction from a subsurface reservoir, *J. Geophys. Res.* 119(2), 8991-9015, doi:10.1002/2014JB011663.
- [9] Brodsky, E., Kanamori, H. (2001). Elaso-hydrodynamic lubrication of faults. *Journal of Geophysical Research*. 106. 16357-16374. 10.1029/2001JB000430.
- [10] Buijze, L., van Bijsterveldt, L., Cremer, H. (2019). Review of worldwide geothermal projects: mechanisms and occurrence of induced seismicity. *TNO*.
- [11] Byerlee, J. D. (1978). Friction of rocks, *Pure Appl. Geophys.*, 116, 615-626.
- [12] Chang, K. W. and Segall, P. (2016). Injection-induced seismicity on basement faults including poroelastic stressing, *J. Geophys. Res. Solid Earth*, 121, doi:10.1002/2015JB012561.
- [13] Comsol cyclopedia. <https://www.comsol.nl/multiphysics>.
- [14] De Barros, L., Daniel, G., Guglielmi, Y., Rivet, D., Caron, H., Payre, X., et al. (2016). Fault structure, stress, or pressure control of the seismicity in shale? Insights from a controlled experiment of fluid-induced fault reactivation. *Journal of Geophysical Research: Solid Earth*, 121, 4506–4522. <https://doi.org/10.1002/2015JB012633>.
- [15] Deflandre, J. P. (2016). Induced Microseismicity: Short Overview, State of the Art and Feedback on Source Rock Production. *The Open Petroleum Engineering Journal*. 9. 55-71. 10.2174/1874834101609010055.
- [16] Doglioni, C. (2018). A classification of induced seismicity. *Geoscience Frontiers*. 9. 10.1016/j.gsf.2017.11.015.
- [17] Dost, B. and Haak, H. (2007). Natural and induced seismicity. *Geology of the Netherlands*.
- [18] DoubletCalc v1.4.3 (2014). TNO model. <https://www.nlog.nl/en/tools>.
- [19] Eisbacher, G.H. (1996). Einführung in die Tektonik. Ferdinand Enke Verlag, Stuttgart, Germany, ISBN 3-432-99252-1, 374p.
- [20] Engelder, T. (1993). Stress regimes in the lithosphere. Princeton University Press, Princeton, New Jersey, USA, ISBN 0-691-08555-2, 475p.
- [21] EU-Commission (2016). Communication from the commission to the European Parliament, the council, the European Economic and Social Committee and the Committee of the regions. Technical report.

- [22] Fjaer, E., Holt, R. M., Horsrud, P., Raaen, A. M. and Risnes, R. (2008). Petroleum related rock mechanics (2nd Edition ed.) Elsevier.
- [23] Gan, Q. and Elsworth, D. (2014). Analysis of fluid injection-induced fault reactivation and seismic slip in geothermal reservoirs, *J. Geophys. Res. Solid Earth*, 119, 3340–3353, doi:10.1002/2013JB010679.
- [24] Ganguly, S. and Mohan Kumar, Ms. (2014). Analytical solutions for transient temperature distribution in a geothermal reservoir due to cold water injection. *Hydrogeology Journal*. 22. 10.1007/s10040-013-1048-2.
- [25] Gaucher, E., Schoenball, M., Heidbach, O., Zang, A., Fokker, P., Van Wees, J. and Kohl, T. (2015). Induced seismicity in geothermal reservoirs: A review of forecasting approaches. *Renewable and Sustainable Energy Reviews*. 52. 1473-1490. 10.1016/j.rser.2015.08.026.
- [26] General Secretariat of the Council, “European Council (23 and 24 October 2014) Conclusions,” 2014.
- [27] Ghassemi, A., Tarasovs, S., Cheng, A.H. (2007). A 3-D study of the effects of thermomechanical loads on fracture slip in enhanced geothermal reservoirs. *International Journal of Rock Mechanics and Mining Sciences* 44:1132
- [28] Goebel, T. and Brodsky, E. (2018). The spatial footprint of injection wells in a global compilation of induced earthquake sequences. *Science*. 361. 899-904. 10.1126/science.aat5449.
- [29] Gradshteyn, I.S., Ryzhik, I.M. (2007). *Table of Integral, Series, and Products*, seventh ed., Elsevier Academic Press, 2007.
- [30] Guglielmi, Y., Cappa, F., Avouac, J.-P., Henry, P. and Elsworth, D. (2015). Seismicity triggered by fluid injection–induced aseismic slip. *Science*, 348(6240), 1224–1226.
- [31] Guo, B., Liu, X., Tan, X. (2017). *Petroleum Production Engineering (Second Edition)*. Gulf Professional Publishing, ISBN 9780128093740.
- [32] Haibin, D. and Gao, D. (2016). Seismic attribute-aided fault detection in petroleum industry: A review.
- [33] Hanks, T. C. and Kanamori, H. (1979). A Moment Magnitude Scale. *Journal of Geophysical Research*, 84 (85), 2348-2350.
- [34] Hillis, R.R. (2000). Pore pressure/stress coupling and its implications for seismicity. *Exploration Geophysics - EXPLOR GEOPHYS*. 31. 10.1071/EG00448.
- [35] Jacquy, A., Cacace, M., Blöcher, G., Scheck-Wenderoth, M. (2015). Numerical Investigation of Thermoelastic Effects on Fault Slip Tendency during Injection and Production of Geothermal Fluids. *Energy Procedia*. 76. 311-320. 10.1016/j.egypro.2015.07.868.
- [36] Jaeger, J. C., Cook, N. G. and Zimmerman, R. (2007). *Fundamentals of rock mechanics*. Oxford, UK: John Wiley & Sons.
- [37] Jin, L. (2015). *Hydromechanical–Stochastic Modeling of Fluid-Induced Seismicity in Fractured Poroelastic Media*. Department of Geophysics, Stanford University.
- [38] Jung, R. (2013). EGS—goodbye or back to the future. *ISRM International Conference for Effective and Sustainable Hydraulic Fracturing*.
- [39] Koh, J., Roshan, H. and Rahman, S. S. (2011). A numerical study on the long term thermo-poroelastic effects of cold water injection into naturally fractured geothermal reservoirs. *Computers and Geotechnics*, 38 (5), 669-682.
- [40] Kostrov, V.V. (1974). Seismic moment and energy of earthquakes and seismic flow of rocks, *Izv. Acad. Sci. USSR Phys. Solid Earth, Eng. Transl.*, 1, 23-44.
- [41] Madariaga, R. (1979). On the relation between seismic moment and stress drop in the presence of stress and strength heterogeneity. *Journal of Geophysical Research: Solid Earth* 84: 2243–2250.

- [42] Martínez - Garzón, P., Kwiatek, G., Sone, H., Bohnhoff, M., Dresen, G. and Hartline, C. (2014). Spatiotemporal changes, faulting regimes, and source parameters of induced seismicity: A case study from The Geysers geothermal field. *Journal of Geophysical Research: Solid Earth*, 119 (11), 8378-8396.
- [43] McGarr, A., Simpson, D., and Seeber, L. (2002). Case histories of induced and triggered seismicity, in *International Handbook of Earthquake and Engineering Seismology*, vol. 81A, pp. 647–661, Academic Press, San Francisco, Calif.
- [44] Moeck, I. (2014). Catalog of geothermal play types based on geologic controls. *Renewable and Sustainable Energy Reviews*. 37. 867–882. 10.1016/j.rser.2014.05.032.
- [45] Paris agreement. (2015). United Nations.
- [46] Passelègue, F., Brantut, N., Mitchell, T. (2018). Fault Reactivation by Fluid Injection: Controls From Stress State and Injection Rate. *Geophysical Research Letters*. 10.1029/2018GL080470.
- [47] Platform geothermie, EBN, DAGO, and WN. 2018. Masterplan Aardwarmte in Nederland.
- [48] Regeerakkoord 2017-2021 “Vertrouwen in de toekomst” by VVD, CDA, D66 en ChristenUnie (10/10/2017), and subsequent Kamerbrief over geothermie by the Minister of Economic Affairs and Climate (08/02/2018). www.rijksoverheid.nl (in Dutch, accessed December 2018).
- [49] Roos, W., Waarts, P.H., Wassing, B.B. (2009). Kalibratiestudie schade door aardbevingen, TNO rapport TNO-034-DTM-2009-04435.
- [50] Rothert, E. and Shapiro, S. (2003). Microseismic monitoring of borehole fluid injections: Data modeling and inversion for hydraulic properties of rocks, *Geophysics*, 68(2), 685–689.
- [51] Rudnicki, J.W. (1986). Fluid mass sources and point forces in linear elastic diffusive solids. *Mechanics of Materials*, v. 5, p. 383-393.
- [52] Saemundsson, K. (2009). Geothermal Systems in a Global Perspective. ISOR – Iceland GeoSurvey. Presented at Short Course 4 on Exploration for Geothermal Resources, organized by UNU-GTP, KenGen and GDC, Lake Naivasha, Kenya, Nov., 2009. Print.
- [53] Schoenball, M., Müller, T., Müller, B., and Heidbach, O. (2010). Fluid-induced microseismicity in pre-stressed rock masses. *Geophysical Journal International*. 180. 813-819. 10.1111/j.1365-246X.2009.04443.x.
- [54] Schoots, K., Hekkenberg, M., and Hammingh, P. (2016). Nationale Energieverkenning 2016. Technical report, Energieonderzoek Centrum Nederland (ECN), Amsterdam/Petten.
- [55] Segall, P. and Lu, S. (2015). Injection-induced seismicity: Poroelastic and earthquake nucleation effects. *J. Geophys. Res.-Solid Earth* 120(7): 5082–5103.
- [56] Shapiro, S., Rentsch, S., Rothert, E. (2005). Characterization of hydraulic properties of rocks using probability of fluid-induced microearthquakes. *Geophysics*. 70. 10.1190/1.1897030.
- [57] Shapiro, S. A., Rothert, E., Rath, V. and Rindschwentner, J. (2002). Characterization of fluid transport properties of reservoirs using induced microseismicity, *Geophysics*, 67, 212–220.
- [58] Sibson, R. H. (1985). A note on fault reactivation. *Journal of Structural Geology*, 7(6), 751–754.
- [59] Staattoezicht op de Mijnen (SodM) (2016). Methodiek voor risicoanalyse ontrent geïnduceerde bevingen door gaswinning.
- [60] Stein, S. and Wysession, M. (2006). *An Introduction to Seismology, Earthquakes, and Earth Structure*. Blackwell Publishing, pp. 2006.
- [61] Stichting DAP website information. <https://www.stichtingdap.nl/>.
- [62] Terzaghi, K. (1943). *Theoretical soil mechanics*. J. Wiley and Sons, New York, xvii, 510p (465 T45 1943).
- [63] Thorsteinsson, H. H. and Tester, J. W. (2010). Barriers and enablers to geothermal district heating system development in the United States, *Energy Policy*, vol. 38, no. 2, pp. 803–813.
- [64] TNO. (2014). Geomechanische tool voor breukreactivatie en fracken bij aardwarmtewinning.

- [65] Townend, J. and Zoback, M.D. (2000). How faulting keeps the crust strong, *Geology*, 28, 399–402.
- [66] Turcotte, D.L. and Schubert, G. (2002). *Geodynamics*. Cambridge University Press, ISBN 0-521-66186-2.
- [67] Van Eck, T., Goutbeek, F.H., Haak, H.W. and Dost, B. (2006). Seismic hazard due to small-magnitude, shallow-source induced earthquakes in the Netherlands. *Engineering Geology*, 87, 105-121.
- [68] Van Eijs, R.M., Mulders, F.M., Nepveu, M., Kenter, C.J. and Scheffers, B.C. (2006). Correlation between hydrocarbon reservoir properties and induced seismicity in the Netherlands. *Engineering Geology*, 84, 99-111.
- [69] Van Thienen-Visser, K., Roholl, J.A., Kempen, B.M., Muntendam-Bos, A.G. (2018). Categorizing seismic risk for the onshore gas fields in the Netherlands. *Engineering Geology*. 237. 10.1016/j.enggeo.2018.02.004.
- [70] Van Thienen-Visser, K., Nepveu, M., Hettelaar, J., (2012). Deterministische hazard analyse voor geïnduceerde seismiciteit in Nederland: TNO-rapport 2012 R10198 (in Dutch).
- [71] Van Wees, J., Fokker, P., Van Thienen - Visser, K., Wassing, B., Osinga, S., Orlic, B., Ghouri, S., Buijze, L. and Pluymaekers, M. (2017). Geomechanical models for induced seismicity in the Netherlands: Inferences from simplified analytical, finite element and rupture model approaches. *Netherlands Journal of Geosciences*, 96(5), S183—S202.
- [72] Willems, C. (2017). Doublet deployment strategies for geothermal Hot Sedimentary Aquifer exploitation: Application to the Lower Cretaceous Nieuwerkerk Formation in the West Netherlands Basin. <https://doi.org/10.4233/uuid:2149da75-ca29-4804-8672-549efb004048>